Long-term records of Antarctic outlet glacier dynamics from historical data and novel remote sensing techniques

By

Sarah F. Child
M.Sc., University of Edinburgh, 2009
B.Sc., SUNY Cortland, 2007

Submitted to the graduate degree program in Geology and the Graduate Faculty of the University of Kansas in partial fulfillment of the requirements for the degree of Doctor of Philosophy.

_____

Chair: Leigh A. Stearns

_____

William C. Johnson

_____

C. J. van der Veen

_____

Alison Olcott

_____

George Tsoflias

Date Defended: 17 March 2020

The dissertation committee for Sarah Child certifies that this is the approved version of the following dissertation:

Long-term records of Antarctic outlet glacier dynamics from historic data and novel remote sensing techniques

Chair: Leigh A. Stearns

Date Approved: 17 March 2020

Abstract

Quantifying how the cryosphere responds to various climate forcings is essential in accurate forecasting of ice sheet stability as well as sea level rise. In order to better predict how future climates will impact ice sheet and glacier mass balance, it is first necessary to understand whether the observed changes in glaciers are from internal dynamics or responses to climate forcings. Equally necessary is the ability to identify if current glacier transformations are due to discrete events or ongoing phenomena. Unfortunately, most records for the world's glaciers only extend for the last two decades, thus making long-term projections difficult. The overall aim of each project is to improve our understanding of cryosphere-climate relationships through long-term observational records and numerical modeling. The three projects are: (1) validating the use of historic aerial imagery with modern-day image processing techniques and manually extracted ground control from high-resolution imagery; (2) quantifying ~60-year surface elevation changes of outlet glaciers flowing through the Transantarctic Mountains from trimetrogon aerial photos; and (3) investigating basal crevasse initiation and determining if the formation of anomalously large crevasses can be proxies for historic Antarctic subglacial flooding events. The first project uses historic vertical aerial imagery and high-resolution optical satellite imagery; the second employs oblique aerial imagery from the 1960s and high-resolution optical satellite imagery; and the last project relies on a combination of airborne radar, *in situ* GPS, and optical satellite imagery. Innovative remote sensing techniques are used to acquire information that is either analyzed or integrated into numerical models (depending on the project) to draw conclusions about the stability of the ice sheet. These results further our understanding of the manner in which ice sheets and glaciers respond to changes in climate and will ultimately allow for more accurate constraints in modeling future sea level rise.

Acknowledgements

First and foremost, I would like to express an enormous gratitude to my advisor Leigh Stearns for giving me this opportunity, her guidance, and support through some incredibly long months of data processing for these past few years. I want to acknowledge the late Gordon Hamilton who indirectly introduced me to Leigh—he was a remarkable person/scientist and it was a privilege to have worked in the field work with him. I want to thank Kees van der Veen for his help with ice dynamics. I thank Bill Johnson for giving me the opportunity to TA for a semester and advice in other research matters. I would like to thank my committee for their guidance and time throughout course of the degree. I thank Donna Helgeson for giving up her time to help with algorithms, Konstantinos Petrakopoulos for his help with Matlab coding, and Luc Girod for his help and advice with SfM processing. I thank Henry Brecher for his original maps and notes and for patiently answering my questions about processing techniques from ~40 years ago. I would also like to acknowledge Andrew Shoemaker for an unjudgmental ear and guidance through the chaos. A very warm thank you to Scott Anderson for being one of my biggest cheerleaders since day 1 of undergrad. I want to thank Jennifer Harris for transatlantic support and encouragement through this process and thank Ashley York and Emma Gencarelli for the same, but from this continent. I thank my parents Steve and Laura Child for everything they've done for me before and during the PhD process. Finally, I want to thank my husband, Besim for all of the post all-nighter breakfasts, clean laundry, and constant support over the years.

Table of Contents

List of Figures:

Chapter 1

Chapter 2

Chapter 3

List of Tables:

Chapter 1

Chapter 2

Chapter 3

List of Equations:

Chapter 1

Chapter 2

Chapter 3

Introduction

The Greenland and Antarctic ice sheets are both losing mass at increased rates: over the past two decades mass loss has increased by ~89% in Greenland (Shepherd et al., 2019a) and ~67% in Antarctica (Shepherd et al., 2018). Understanding the processes that drive mass loss and putting recent patterns of mass loss into a broader context of cryosphere-climate interactions requires data covering various spatial and temporal scales. In Antarctica, while remote-sensing data currently cover the entire continent, it has only done so since 1999. Without studies going back further than 20-years, it is difficult to know for certain whether current results are the result of currently changing climate, or long-term naturally occurring transitioning dynamics. The overarching theme of this study is to expand the temporal scale of Antarctic outlet glacier research using historic aerial photographs and innovative processing techniques.

Antarctica surface elevation changes

Over the past 25 years, Antarctica has undergone slight thickening in the interior and thinning around large swaths of the coast (Shepherd et al., 2018; Shepherd et al., 2019b; Schröder et al., 2019; Rignot et al., 2019). Antarctic surface elevation change over the past 25 years is estimated to be 2.3 ± 2.4 m/yr, causing a sea level rise of 4.6±1.2 mm (Shepherd et al., 2019b). Prior to the 1990s, there is no information about surface elevation variability or Antarctic mass loss.

Continent-wide surface elevation studies typically rely on radar and LiDAR satellite altimeters (McMillan et al., 2014; Helm et al., 2014; Shepherd et al., 2018; Schröder et al., 2019). Altimeters require corrections for firn compaction, waveform saturation (Zwally et al., 2002;

Helm et al., 2014), and isostatic adjustment (Whitehouse at al., 2012; McMillan et al., 2014). In East Antarctica, where ground-based data are sparse, isostatic adjustment is not well constrained. As a result, mass balance measurements have large errors (~9 times greater than for the Western Antarctic Ice Sheet (WAIS) and the Antarctic Peninsula (AP)) (Shepherd et al., 2018; Hanna et al., 2019). Consequently, mass balance estimates for Byrd Glacier, which has the world's largest catchment basin, disagree as to whether there is mass loss (e.g. -7.2 ± 3.4 Gt/yr (Sasgen et al., 2019)) or mass gain (e.g. 5 ± 18 Gt/yr (Gardner et al., 2019)). Furthermore, the latest Cryosat-2 digital elevation model (DEM) has errors of 10-180 m for this region in Antarctica (Slater et al., 2018).

Surface elevation thinning can be caused by increased surface melt (Cape et al., 2015; van den Broeke et al., 2009), increased calving rates (Hulbe et al., 2008; Benn et al., 2017), or increased basal melting (Pritchard et al., 2012; Bernales et al., 2017; Reese et al., 2017). Of these three, contributions from basal melting are estimated to be the highest (Depooter et al., 2013; Rignot et al., 2013; Pritchard et al., 2012) with Depooter et al. (2013) reporting 1,321 ± 144 Gt/yr and 1,454 ± 174 Gt/yr for calving and basal melt rates, respectively and Rignot et al. (2013) estimating calving rates of 1,089 ± 139 Gt/yr and a basal melt rate of 1325 ± 235 Gt/yr. Basal melt rates can affect the location of a glacier's grounding line—the boundary where glacier flow transitions from being grounded with bedrock to marine floating. The location of the grounding line can play a vital role in the stability of the world's ice sheets (Schoof, 2007; Weertman, 1974), particularly its location with respect to the bedrock slope. As a grounding line retreats up-flow, the speed of the glacier can increase which causes an increase in glacier ice discharge and a decrease in surface elevation (Scheuchl et al., 2014; Friedl et al., 2020). This phenomenon is

accredited as the main driver for the rapid retreat of outlet glaciers in Greenland (Joughin et al., 2012; Moon et al., 2014), the Antarctic Peninsula (AP) (Cook et al., 2016; Wouters et al., 2015), and possibly the West Antarctic Ice Sheet (WAIS) (Pollard and DeConto, 2009).

Grounding line migration is one way of assessing outlet glacier stability (Konrad et al., 2018), but identifying the location of a grounding line is difficult as it requires knowledge of a glacier's flexure point (the boundary where ocean tides do not cause vertical motion) or the boundary of where the glacier is in hydrostatic equilibrium (which requires ice thickness and surface elevation) (Vaughn, 1994; Fricker et al., 2002; Fricker et al., 2009; Brunt et al., 2010). As a result, accurately identifying the grounding line requires high spatial resolution information for surface elevation, ice thickness, or flexure measurements that are challenging to acquire for long temporal resolutions, making it difficult to monitor glacier stability. An alternative method of assessing outlet glacier stability is by monitoring just surface elevation changes over long temporal scales. Having a better understanding of the long-term trends of surface elevation change permits better prediction of those outlet glaciers that are most vulnerable and thus pose the greatest risk for increasing sea levels.

To expand the spatial and temporal extent of surface elevation changes for outlet glaciers flowing through the Transantarctic Mountains, photogrammetric techniques are used to process historic aerial photography collected over Antarctica from 1946-2000 by the United States Navy. Even with modern computational methods, typical photogrammetric processing of analog aerial photography is arduous and requires a great deal of information about the flight at the time of data collection and at least three identified points of ground control for every image. Flight

information is required (such as the plane's altitude, roll, yaw, and pitch), as well as the camera's focal length, and the geometry (fiducial mark and principle point locations) of an image. Much of this information has either never been digitized or has been lost since the time of data collection, and amassing *in situ* ground control for every aerial image would be an astronomical cost, both logistically and financially.

In Chapter 1, a new methodology is assessed using Structure-from-Motion (SfM) processing of historic analog aerial photography where ground control is established from present-day, high-resolution satellite data to produce digital elevation models (DEMs). SfM processing uses traditional photogrammetric concepts, but improves upon the methodology by utilizing algorithms that locate features in multiple images not laid out in a perfect grid. Furthermore, resulting errors are minimized from iterative cost functions that remove tie point outliers and reduce the effect of incorrectly placed ground control points (Carrivick et al., 2016 p. 38-50). SfM processing requires only three ground control points (GCPs) for an entire dataset and minimal camera metadata, which makes this workflow significantly less rigid than traditional photogrammetry. SfM studies have been conducted on the Antarctic Peninsula, where abundant ground-control exists and the workflow could rely on relief matching of a historic point cloud to a present-day point cloud (Kunz et al., 2012; Fieber et al., 2018). The methodology used herein differs in that ground control is determined by manually identifying latitude, longitude, and elevation of features within aerial images. This ensures that only exposed bedrock (never ice, snow, lateral moraines, or permafrost, all of which risk elevation change over time) is used in the stereo-parallax calculations, and an increased number of GCPs has shown to produce more accurate results in highly sloped regions.

A case study of this methodology is first performed to assess both its effectiveness and its accuracy. This case study takes place on Byrd Glacier using two sets of 0° nadir aerial images collected in the late 1970s. The results are compared to the elevations estimated using manual photogrammetric techniques carried out in 1980, which reveals that the SfM DEMs outperform the elevations derived manually ~40 years ago. The study is then expanded to use oblique aerial imagery collected in the early 1960s of seven outlet glaciers between 79°S to 86°S and estimate ~60-year elevation changes.

Basal Crevasses

A basal crevasse is a fracture that forms at the bottom of a glacier, and like surface crevasses is an expression of strain acting on a glacier. If a series of basal crevasses have uniform geometry and evenly spaced along the glacier, then the assumption is that strain rates have been constant over time; if crevasses are asymmetric in pattern and/or geometry, then it is likely the glacier has undergone shortly-lived increases in strain, possibly due to changes in external forces. Basal crevasses were first mentioned in literature in the early 1970s (Weertman, 1973) and first observed by Jezek et al. (1979) in ground penetrating radar, but have received little attention in the literature in both observational (Jezek et al., 1979; McGrath et al., 2012; Luckman et al., 2012; Vaughn et al., 2012; Jacobel et al., 2014) and theoretical (Rist et al., 1996; van der Veen, 1998) studies. Basal crevasses are important because of the role they play in the calving process. It is hypothesized that basal crevasses either propagate until they meet with downwardly propagating surface crevasses (Weertman, 1980; Nick et al., 2010; Bassis and Ma, 2015) or they are the initial trigger for rift formation (Walker and Gardner, 2019) (the main mechanism for

tabular icebergs). However, iceberg formation models have had difficulty in accurately constraining the effect from basal crevasse formation and propagation (Bassis and Jacob, 2013; Stern et al., 2019).

Basal crevasses are primarily found on the ice shelves of Antarctica (Jezek et al., 1979; Jezek and Bentley, 1983; Jezek, 1984; Rist et al., 1996; Rist et al., 2002; McGrath et al., 2012; Luckman et al., 2012; Vaughan et al., 2012; Logan et al., 2013), but they have been modeled (James et al., 2014; Murry et al., 2015) and observed in some Greenland outlet glaciers (Münchow et al., 2014; Lewis, 2015), as well as interpreted from data collected during basal hydrological events in Alaskan glaciers (Harper et al., 2010). This research focuses on basal crevasses located within the fjord of Byrd Glacier, East Antarctica.

Heights of the basal crevasses from Byrd Glacier range in size from 10-335 m. Crevasses considering abnormally large (165-335 m), can be identified in both present-day radar as well as historic radar echograms. These large basal crevasses can also be tracked from optical satellite data because they form surface depressions directly above, whereas relatively small basal crevasses (< 150m tall) do not form surface depressions. By tracking surface depressions along the Byrd Glacier flowline to the point of basal crevasse formation (which is assumed to be the grounding zone), a timeline is produced of initial basal crevasse propagation which expands over 600 years.

It was suggested in Clough (1975) that understanding the processes of basal crevasses and mapping their present locations provides a temporal map of the dynamics acting on an outlet

glacier at a specific moment in time. Byrd Glacier experienced a speed-up in ice flow, from 2005-2007, that was caused by a subglacial flooding event from two up-stream subglacial lakes. The additional basal water and speed-up created conditions for an abnormally large (~335 m) basal crevasse to form at the grounding line, which leads to the hypothesis that abnormally large basal crevasses only form during subglacial flooding events. Assembling a timeline of abnormally large crevasse initiations means it is possible to not only compile a timeline of past subglacial flooding events, but a timeline of external forcings as well. Quantifying the long-term patterns of subglacial flooding events aids in better understanding glacier variability that is not modulated by present-day warming conditions.

Research Questions

By expanding the temporal scale of Antarctic outlet glacier surface elevation change and basal crevasse research, this dissertation aims to answer the following questions:

- Can modern image processing techniques of historic aerial photography in conjunction of manually extracted ground control produce accurate digital elevation models of Antarctic Glaciers? (Chapter 1)
- Have Transantarctic Mountain outlet glaciers been losing mass for the last 60 years? (Chapter 2)
- Can abnormally large basal crevasses act as proxies for past subglacial flooding events? (Chapter 3)

Introduction Citations

Bassis, J.N. and Jacobs, S. (2013). Diverse calving patterns linked to glacier geometry. *Nature Geoscience*, *6*(10), 833-836.

Bassis, J.N. and Ma, Y. (2015). Evolution of basal crevasses links ice shelf stability to ocean forcing. *Earth and Planetary Science Letters*, *409*, 203-211.

Benn, D. I., Cowton, T., Todd, J., and Luckman, A. (2017). Glacier calving in Greenland. *Current Climate Change Reports*, *3*(4), 282-290.

Bernales, J., Rogozhina, I., and Thomas, M. (2017). Melting and freezing under Antarctic ice shelves from a combination of ice-sheet modelling and observations. *Journal of Glaciology*, *63*(240), 731-744.

Brunt, K.M., Fricker, H.A., Padman, L., Scambos, T.A., and O'Neel, S. (2010). Mapping the grounding zone of the Ross Ice Shelf, Antarctica, using ICESat laser altimetry. *Annals of Glaciology*, *51*(55), 71-79.

Cape, M.R., Vernet, M., Skvarca, P., Marinsek, S., Scambos, T., and Domack, E. (2015). Foehn winds link climate-driven warming to ice shelf evolution in Antarctica. *Journal of Geophysical Research: Atmospheres*, *120*(21), 11037-11057.

Carrivick, J.L., Smith, M.W., and Quincey, D.J. (2016). *Structure from Motion in the Geosciences*. John Wiley and Sons.

Clough, J.W. (1975). Abstracts of papers presented at the symposium but not published in full. *Journal of Glaciology*, *15*(73), 457.

Cook, A.J., Holland, P.R., Meredith, M.P., Murray, T., Luckman, A., and Vaughan, D.G. (2016). Ocean forcing of glacier retreat in the western Antarctic Peninsula. *Science*, *353*(6296), 283-286.

Depoorter, M.A., Bamber, J.L., Griggs, J.A., Lenaerts, J.T., Ligtenberg, S.R., van den Broeke, M.R., and Moholdt, G. (2013). Calving fluxes and basal melt rates of Antarctic ice shelves. *Nature*, *502*(7469), 89-93.

Fieber, K.D., Mills, J.P., Miller, P.E., Clarke, L., Ireland, L., and Fox, A.J. (2018). Rigorous 3D change determination in Antarctic Peninsula glaciers from stereo WorldView-2 and archival aerial imagery. *Remote Sensing of Environment*, *205*, 18-31.

Fricker, H.A., Allison, I., Craven, M., Hyland, G., Ruddell, A., Young, N., Coleman, R., King, M., Krebs, K., and Popov, S. (2002). Redefinition of the Amery ice shelf, East Antarctica, grounding zone. *Journal of Geophysical Research: Solid Earth*, *107*(2092).

Fricker, H.A., Coleman, R., Padman, L., Scambos, T.A., Bohlander, J., and Brunt, K.M. (2009). Mapping the grounding zone of the Amery Ice Shelf, East Antarctica using InSAR, MODIS and ICESat. *Antarctic Science, 21*(5), 515-532.

Friedl, P., Weiser, F., Fluhrer, A., and Braun, M.H. (2019). Remote sensing of glacier and ice sheet grounding lines: A review. *Earth-Science Reviews, 201*(102948).

Gardner, A.S., Moholdt, G., Scambos, T., Fahnstock, M., Ligtenberg, S., van den Broeke, M., and Nilsson, J. (2018). Increased West Antarctic and unchanged East Antarctic ice discharge over the last 7 years. *Cryosphere*, *12*(2), 521-547.

Hanna, E., Pattyn, F., Navarro, F., Favier, V., Goelzer, H., van den Broeke, M.R., Vizcaino, M., Whitehouse, P.L., Ritz, C., Bulthuis, K., and Smith, B. (2019). Mass balance of the ice sheets and glaciers–progress since AR5 and challenges. *Earth-Science Reviews, 201*(102976).

Harper, J.T., Bradford, J.H., Humphrey, N.F., and Meierbachtol, T.W. (2010). Vertical extension of the subglacial drainage system into basal crevasses. *Nature*, *467*(7315), 579-582.

Helm, V., Humbert, A., and Miller, H. (2014). Elevation and elevation change of Greenland and Antarctica derived from CryoSat-2. *The Cryosphere*, *8*(4), 1539-1559.

Hulbe, C.L., Scambos, T.A., Youngberg, T., and Lamb, A.K. (2008). Patterns of glacier response to disintegration of the Larsen B ice shelf, Antarctic Peninsula. *Global and Planetary Change*, *63*(1), 1-8.

Jacobel, R.W., Christianson, K., Wood, A.C., Dallasanta, K.J., and Gobel, R.M. (2014). Morphology of basal crevasses at the grounding zone of Whillans Ice Stream, West Antarctica. *Annals of Glaciology*, *55*(67), 57-63.

James, T.D., Murray, T., Selmes, N., Scharrer, K., and O'Leary, M. (2014). Buoyant flexure and basal crevassing in dynamic mass loss at Helheim Glacier. *Nature Geoscience*, *7*(8), 593-596.

Jezek, K.C., Bentley, C.R., and Clough, J.W. (1979). Electromagnetic sounding of bottom crevasses on the Ross Ice Shelf, Antarctica. *Journal of Glaciology*, *24*(90), 321-330.

Jezek, Kenneth C. and Charles R. Bentley. (1983). Field studies of bottom crevasses in the Ross Ice Shelf, Antarctica. *Journal of Glaciology*, *29*(101), 118-126.

Jezek, K.C., (1984). A modified theory of bottom crevasses used as a means for measuring the buttressing effect of ice shelves on inland ice sheets. *Journal of Geophysical Research: Solid Earth*, *89*(B3), 1925-1931.

Joughin, I., Alley, R.B., and Holland, D.M. (2012). Ice-sheet response to oceanic forcing. *Science*, *338*(6111), 1172-1176.

Konrad, H., Shepherd, A., Gilbert, L., Hogg, A.E., McMillan, M., Muir, A., and Slater, T. (2018). Net retreat of Antarctic glacier grounding lines. *Nature Geoscience*, *11*(4), 258-262.

Kunz, M., King, M.A., Mills, J.P., Miller, P.E., Fox, A.J., Vaughan, D.G., and Marsh, S.H. 2012. Multi-decadal glacier surface lowering in the Antarctic Peninsula. *Geophysical Research Letters*, *39*(19).

Lague, D., Brodu, N., and Leroux, J. (2013). Accurate 3D comparison of complex topography with terrestrial laser scanner: Application to the Rangitikei canyon (NZ). *ISPRS Journal of Photogrammetry and Remote Sensing*, *82*, 10-26.

Lewis, C.S. (2015). *Ice Shelf Melt Rates and 3D Imaging*. PhD, University of Kansas.

Logan, L., Catania, G., Lavier, L., and Choi, E. (2013). A novel method for predicting fracture in floating ice. *Journal of Glaciology*, *59*(216), 750-758.

Luckman, A., Jansen, D., Kulessa, B., King, E., Sammonds, P., and Benn, D.I. (2012). Basal crevasses in Larsen C Ice Shelf and implications for their global abundance. *The Cryosphere*, *6*(1), 113-123.

McGrath, D., Steffen, K., Rajaram, H., Scambos, T., Abdalati, W., and Rignot, E. (2012). Basal crevasses on the Larsen C Ice Shelf, Antarctica: Implications for meltwater ponding and hydrofracture. *Geophysical Research Letters*, *39*(16).

McMillan, M., Shepherd, A., Sundal, A., Briggs, K., Muir, A., Ridout, A., Hogg, A., and Wingham, D. (2014). Increased ice losses from Antarctica detected by CryoSat-2. *Geophysical Research Letters*, *41*(11), 3899-3905.

Moon, T., Joughin, I., Smith, B., Van Den Broeke, M.R., Van De Berg, W.J., Noël, B., and Usher, M. (2014). Distinct patterns of seasonal Greenland glacier velocity. *Geophysical Research Letters*, *41*(20), 7209-7216.

Münchow, A., Padman, L., and Fricker, H.A. (2014). Interannual changes of the floating ice shelf of Petermann Gletscher, North Greenland, from 2000 to 2012. *Journal of Glaciology*, *60* (221), 489-499.

Murray, T., Selmes, N., James, T.D., Edwards, S., Martin, I., O'Farrell, T., Aspey, R., Rutt, I., Nettles, M., and Baugé, T. (2015). Dynamics of glacier calving at the ungrounded margin of Helheim Glacier, southeast Greenland. *Journal of Geophysical Research: Earth Surface*, *120*(6), 964-982.

Nick, F.M., Van der Veen, C.J., Vieli, A., and Benn, D.I. (2010). A physically based calving model applied to marine outlet glaciers and implications for the glacier dynamics. *Journal of Glaciology*, *56*(199), 781-794.

Paolo, F.S., Fricker, H.A., and Padman, L. (2015). Volume loss from Antarctic ice shelves is accelerating. *Science*, *348*(6232), 327-331.

Pollard, D. and DeConto, R.M. (2009). Modelling West Antarctic ice sheet growth and collapse through the past five million years. *Nature*, *458*(7236), 329-333.

Pritchard, H., Ligtenberg, S.R., Fricker, H.A., Vaughan, D.G., van den Broeke, M.R., and Padman, L. (2012). Antarctic ice-sheet loss driven by basal melting of ice shelves. *Nature*, *484*(7395), 502-505.

Rignot, E., Jacobs, S., Mouginot, J., and Scheuchl, B. (2013). Ice-shelf melting around Antarctica. *Science*, *341*(6143), 266-270.

Rignot, E., Mouginot, J., Scheuchl, B., van den Broeke, M., van Wessem, M.J., and Morlighem, M. (2019). Four decades of Antarctic Ice Sheet mass balance from 1979–2017. *Proceedings of the National Academy of Sciences*, *116*(4), 1095-1103.

Rist, M.A., Sammonds, P.R., Murrell, S.A.F., Meredith, P.G., Oerter, H., and Doake, C.S.M. (1996). Experimental fracture and mechanical properties of Antarctic ice: preliminary results. *Annals of Glaciology*, *23*, 284-292.

Rist, M.A., Sammonds, P.R., Oerter, H., and Doake, C.S.M. (2002). Fracture of Antarctic shelf ice. *Journal of Geophysical Research: Solid Earth*, *107*(B1), pp.ECV-2.

Sasgen, I., Konrad, H., Helm, V., and Grosfeld, K. (2019). High-Resolution Mass Trends of the Antarctic Ice Sheet through a Spectral Combination of Satellite Gravimetry and Radar Altimetry Observations. *Remote Sensing*, *11*(144).

Scheuchl, B., Mouginot, J., Rignot, E., Morlighem, M., and Khazendar, A. (2016). Grounding line retreat of Pope, Smith, and Kohler Glaciers, West Antarctica, measured with Sentinel-1a radar interferometry data. *Geophysical Research Letters*, *43*(16), 8572-8579.

Schoof, C. (2007). Ice sheet grounding line dynamics: Steady states, stability, and hysteresis. *Journal of Geophysical Research: Earth Surface*, *112*(F3).

Schröder, L., Horwath, M., Dietrich, R., Helm, V., Van Den Broeke, M.R., and Ligtenberg, S.R. (2019). Four decades of Antarctic surface elevation changes from multi-mission satellite altimetry. *The Cryosphere*, *13*(2), 427-449.

Shepherd, A., Ivins, E., Rignot, E., Smith, B., Van Den Broeke, M., Velicogna, I., Whitehouse, P., Briggs, K., Joughin, I., Krinner, G., and Nowicki, S. (2018). Mass balance of the Antarctic Ice Sheet from 1992 to 2017. *Nature*, *558*, 219-222.

Shepherd, A., Gilbert, L., Muir, A.S., Konrad, H., McMillan, M., Slater, T., Briggs, K.H., Sundal, A.V., Hogg, A.E., and Engdahl, M. (2019) (B). Trends in Antarctic Ice Sheet Elevation and Mass. *Geophysical Research Letters*. *46*(14), 8174-8183.

Shepherd, A., Ivins, E., Rignot, E., and Fettweis, X. (2019) (A). Mass balance of the Greenland Ice Sheet from 1992 to 2018. *Nature, 579*, 233-239.

Slater, T., Shepherd, A., McMillan, M., Muir, A., Gilbert, L., Hogg, A.E., Konrad, H., and Parrinello, T. (2018). A new digital elevation model of Antarctica derived from CryoSat-2 altimetry. *The Cryosphere*, *12*(4), 1551-1562.

Stern, A.A., Adcroft, A., and Sergienko, O. (2019). Modeling Ice Shelf Cavities and Tabular Icebergs Using Lagrangian Elements. *Journal of Geophysical Research: Oceans*, *124*(5), 3378-3392.

van den Broeke, M., Bamber, J., Ettema, J., Rignot, E., Schrama, E., van de Berg, W.J., van Meijgaard, E., Velicogna, I., and Wouters, B. (2009). Partitioning recent Greenland mass loss. *Science*, *326*(5955), 984-986.

Van der Veen, C.J. (1998). Fracture mechanics approach to penetration of bottom crevasses on glaciers. *Cold Regions Science and Technology*, *27*(3), 213-223.

Vaughan, D.G. (1994). Investigating tidal flexure on an ice shelf using kinematic GPS. *Annals of Glaciology*, *20*, 372-376.

Vaughan, D.G., Corr, H.F., Bindschadler, R.A., Dutrieux, P., Gudmundsson, G.H., Jenkins, A., Newman, T., Vornberger, P., and Wingham, D.J. (2012). Subglacial melt channels and fracture in the floating part of Pine Island Glacier, Antarctica. *Journal of Geophysical Research: Earth Surface*, *117*(F3).

Walker, C.C. and Gardner, A.S. (2019). Evolution of ice shelf rifts: Implications for formation mechanics and morphological controls. *Earth and Planetary Science Letters*, *526*(115764).

Weertman, J. (1973). Can a water-filled crevasse reach the bottom surface of a glacier. *IASH publ*, *95*, 139-145.

Weertman, J. (1974). Stability of the junction of an ice sheet and an ice shelf. *Journal of Glaciology*, *13*(67), 3-11.

Weertman, J. (1980). Bottom crevasses. *Journal of Glaciology*, *25*(91), 185-188.

Whitehouse, P.L., Bentley, M.J., and Le Brocq, A.M. (2012). A deglacial model for Antarctica: geological constraints and glaciological modelling as a basis for a new model of Antarctic glacial isostatic adjustment. *Quaternary Science Reviews*, *32*, 1-24.

Wouters, B., Martin-Español, A., Helm, V., Flament, T., van Wessem, J.M., Ligtenberg, S.R., Van den Broeke, M.R., and Bamber, J.L. (2015). Dynamic thinning of glaciers on the Southern Antarctic Peninsula. *Science*, *348*(6237), 899-903.

Zwally, H.J., Schutz, B., Abdalati, W., Abshire, J., Bentley, C., Brenner, A., Bufton, J., Dezio, J., Hancock, D., Harding, D., and Herring, T. (2002). ICESat's laser measurements of polar ice, atmosphere, ocean, and land. *Journal of Geodynamics, 34*(3-4), 405-445.

Chapter 1
Applying Structure-from-Motion techniques to process historic aerial imagery with high-resolution satellite data for ground control of Byrd Glacier

1.1 Introduction

Quantifying how the cryosphere responds to climate forcings is essential for predictions of ice sheet mass loss and sea level rise. Unfortunately, records of Antarctic glacier behavior only extend a few decades — the extent of the modern satellite era. As such, glacier characteristics, including ice velocity, surface elevation, and crevasse patterns, are only available from the early 1990s to present. Infrequent images from older satellites (e.g. early generation Landsat, and spy satellites) consist of coarse resolutions and/or significant cloud cover. As a result, little is known about Antarctic glacier behavior prior to 1990. In this study, we outline the methodology for using historic aerial imagery (collected prior to 1980) to quantify glacier behavior. By extending the temporal scale of glaciology data, we improve our understanding of ice sheet behavior in a changing climate, which is essential for physically based sea level rise projections.

The 4th IPCC report specifically identified the need for high-temporal resolution remote sensing data to improve understanding of glaciological processes (Anisimov et al., 2007). In the 5th IPCC report (~six years later), much more effort was put into launching new polar-observing satellites as well as collecting additional airborne data (Vaughn et al., 2013). While the spatial coverage of Antarctic observations has improved, the temporal timeline of data collection still remains short. Aerial imagery has been collected since the 1930s in Antarctica, but only a small fraction of the data has been used in analytical research. This imagery was originally collected for topographic

mapping, but the data have largely been neglected since then. A major reason why this historic aerial imagery in Antarctica has been underutilized is that it is inherently difficult to process.

Using digitally scanned historical imagery to render accurate terrain surfaces has been done successfully by many others (Cook et al., 2005; Fox and Cziferszky, 2008; Guzzetti et al., 2012; Bjørk et al., 2012; Schiefer and Gilbert, 2007; etc.). However, processing historical imagery is a non-trivial task because there is no exchangeable image file (EXIF) information. As a result, there is a large manual component involved in rendering elevations and ortho-images. In Antarctica there is an additional obstacle: the lack of ground control points. Ground control points (GCPs) are essential to accurately geolocate historic images. We employ a new method of utilizing manually extracted GCPs from high-resolution digital elevation models (DEMs). This technique has been applied to small Arctic glaciers (Girod et al., 2018; Nielsen, 2017), but never to Antarctic glaciers, which are often wider than individual images (therefore lacking ground control points). To assess the applicability of SfM processing with remotely extracted GCPs, this methodology is applied to an extensive collection of 1970s aerial photographs of Byrd Glacier, East Antarctica to create high-resolution elevation and velocity products.

In December 1978 and January 1979, two sets of aerial images were collected over Byrd Glacier, as part of a large-scale research project (Hughes and Fastook, 1981). The original image processing was done in 1980 after which the images went missing for 36 years. In 2016, we located the original images in the basement of the USGS Library in Reston, VA; they were then sent to the EROS center in Sioux Falls, ND where they were digitally scanned at 1,000 dpi. We use modern-day structure-from-motion (SfM) software to process these images and compare the

elevation and velocity results with those that were manually derived in the 1980s (Brecher, 1982). Real-world XYZ values were assigned from GCPs extracted from high resolution satellite data. To the best of our knowledge, no other studies in Antarctica using SfM processing with manually extracted ground control. This workflow, which relies on modern processing techniques applied to historic images with little ground control, can be applied to other aerial images. Over 300,000 aerial photographs of Antarctica were collected from 1930-2000, but have remained untouched for decades, largely due to arduous processing logistics. Here, we prove the validity of our processing technique, which can later be applied to this large dataset of historic images.

1.2 Study Site

Byrd Glacier is located at ~80.4°S, where it flows through the Transantarctic Mountains and terminates in the Ross Ice Shelf (RIS). The catchment basin of Byrd Glacier, which is the largest in the world, is 933,744 km^2 (Rignot et al., 2019). The glacier trunk is ~100 km long and ~25 km wide and is bounded by the Britannia Range to the north and the Churchill Mountains to the south. At the grounding line, the average ice thickness is ~2000 m, and the ice is moving at a velocity of ~850 m/yr (Stearns, 2007).

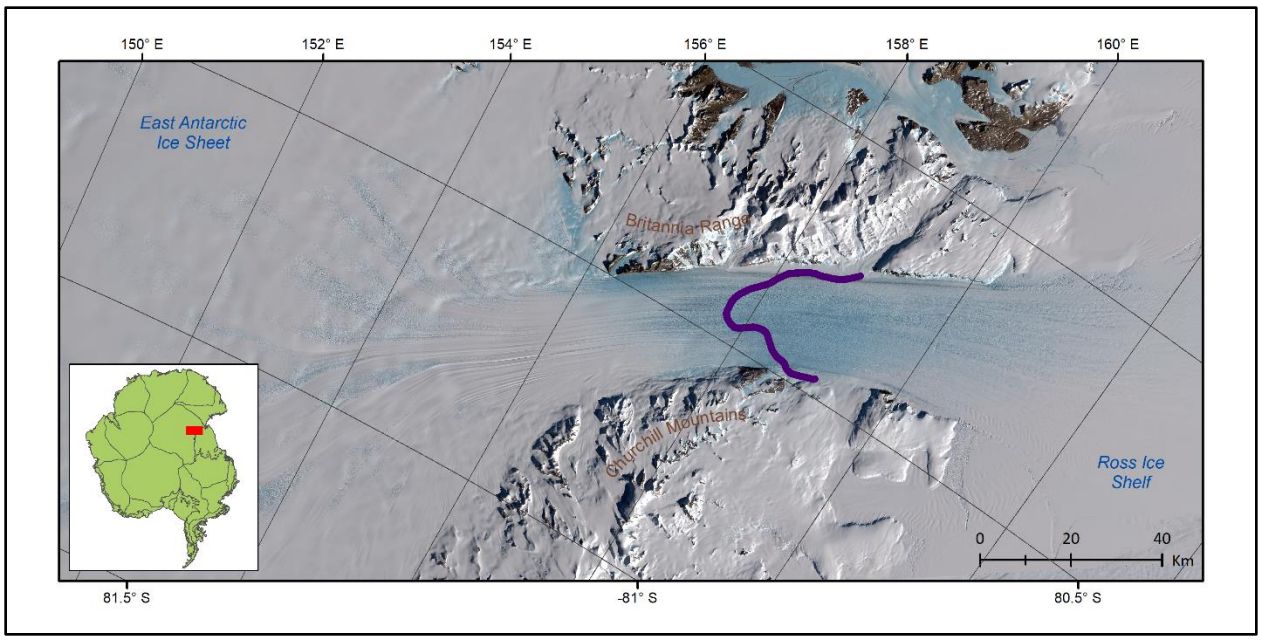

Figure 1.1: Location of study, Byrd Glacier, highlighted by red box in lower left map inset. The direction of flow for this figure and all following figures is from the left to the right of the map and the thick violet line denotes the grounding line. The background image is a band combination composite of Bands 3, 4, and 5 from Landsat-8 OLI acquired on January 28, 2019 (also used for all subsequent figures).

Byrd Glacier is the first Antarctic glacier observed to accelerate following the rapid drainage of a subglacial lake in its catchment (Stearns et al., 2008; Carter et al., 2017). The surface of Byrd Glacier is heavily crevassed and surrounded by steeply sloped mountains. These characteristics make Byrd Glacier a good candidate for SfM processing because textured surfaces produce the best surfaces from stereo-parallax calculations. In this region of Antarctica, there is no vegetation, little snowfall, and no man-made structures, so the DEM construction of the topography is actually a digital terrain model (DTM), but is referred to as DEM throughout the rest of this chapter.

1.3 Data

We use a combination of optical imagery, GPS, and vector data to create and validate historic DEMs. To produce historical surface elevations, ground control must be applied to image

geometry in order to calculate absolute ground relief. Our ground control is manually extracted using present-day high-resolution elevation data. The GPS and vector data are used to register the historical DEMs to absolute elevations and assess the accuracy of the results.

1.3.1 Aerial Imagery

1.3.1.1 Imagery

Aerial photographs were collected on December 6, 1978 and January 31, 1979 (56 days apart). All images were acquired using a Wild-Heebrugg RC8 Aerial Camera that captured vertical (0º nadir) images on 9x9 inch Kodak Safety Film. Film was scanned by the USGS EROS center at 1,000 dpi, 25 micrometers, in 2016.

The plane collecting the imagery was a C-130 flown by the U.S. Navy VXE-6 squadron at an altitude of ~7,000 - 8,000m. At this altitude and a focal length of 152.276 mm, images were captured at an approximate map scale of 1:48,000-1:50,000 and a spatial scale of 1.5-2 m. A total of 568 aerial photographs were captured from 15 flights over the glacier in two flight days. All flights were flown parallel to ice flow with the exception of one semi-orthogonal flight on December 6, 1978. A malfunction in two of the instrument lights at the edge of the frame occurred during the 1978 acquisition, resulting in white stripes in all images collected on that day.

1.3.1.2 Original Study (Brecher, 1982)

The aerial photographs were initially processed in 1980 on a stereo comparator where XYZ positions were estimated by simultaneously using a least-squares adjustment on the two blocks

of photographs (Brecher, 1982). The relative horizontal and vertical errors were estimated at 0.8 m and 1.8 m, respectively. *In situ* ground control was established from trilateration measured from Jason-1 Microwave Radiometer (JMR-1) doppler positioning equipment. A total of 13 GCPs were measured from stable relief surrounding Byrd Glacier. Images from both collection dates were used to create DEMs as well as orthorectified mosaics of each epoch. Only 322 images were needed to generate the DEM and photo-mosaics (152 from 1978 and 170 from 1979). Velocities were derived from the orthorectified images by manually identifying over 600 common features between the two time periods, with an approximated uncertainty of ~5 m (Brecher, 1982).

Several years after the original data were published (Brecher, 1982), an error in the polar stereographic calculation was found for several velocity points (Brecher, NSIDC). However, the difference between the published and corrected locations was found to be negligible and did not affect the original velocity results.

1.3.2 High Resolution DEM

A high-resolution DEM is essential for remotely identifying accurate GCPs. The only high-resolution DEM currently available over Byrd Glacier is the Regional Elevation Model of Antarctica (REMA version 3.x; Howat et al., 2019). This dataset is produced by mosaicing DEM strips derived from DigitalGlobe's WorldView sensor from 2016-2017. REMA is publicly available at the Polar Geospatial Center (PGC) at a horizontal resolution of 2 m and projected to WGS84 Antarctic Polar Stereographic. The DEM strips that comprise REMA are based on the WGS84 ellipsoid and created from a surface extraction TIN-based search-space minimization

(SETSM) algorithm after Noh and Howat (2015). These DEMs are created without ground control which means that the geolocation is approximated from the sensor's rational polynomial coefficients (RPCs), and the subsequent error of this product is entirely dependent on the accuracy of the RPCs (Noh and Howat, 2015). Systematic error estimates are difficult to establish because there is currently no formal metadata for REMA's horizontal or vertical accuracies. Unprocessed WorldView imagery has a vertical accuracy of ~5 m excluding terrain effects (DigitalGlobe, 2014). The online documentation provided by PGC reports the vertical error to be 3.5 m; however, Noh and Howat (2017) report accuracies of ~2-3 m in all directions and ~0.2 m for DEMs co-registered to dense ground control. An error estimate of ~0.2 m in the Transantarctic Mountains is unlikely due to image collection geometry (e.g. high degrees of nadir) and very sparse ground control. A comparison of an SETSM DEM with LiDAR data resulted in errors of 4-5 m in regions of high-sloped terrain (Glennie, 2017). Throughout the rest of this chapter, the individual DEM strips and mosaics are referred to as the "present-day DEM".

1.3.2.1 Rock Mask

We use a publicly available rock mask (Burton-Johnson et al., 2016) to co-register stable terrain (e.g. rock outcrops) in the historic DEMs to the present-day DEM (REMA). The rock mask was generated from Landsat 8 images to calculate a normalized difference snow index (NDSI) over Antarctica; because the spatial extent of Landsat is limited to 82.6°S and the spatial resolution of the bands (3 and 6) that comprise the NDSI is 30 m, we verify all rock outcrop boundaries using WorldView ortho-imagery (posted at 2 m).

1.3.2.2 GPS Data

From 2010-2013, a series of NetR9 Trimble GPS sites were deployed on Byrd Glacier including three reference sites on exposed bedrock. The GPS data has a precision of 3 cm. We use the GPS XYZ values to evaluate the absolute accuracy of the SfM processed elevations.

1.4 Methodology

1.4.1 Ground Control Points

Traditional ground control is typically established using *in situ* geodetic surveys. In Antarctica, this type of ground control is limited due to inaccessibility, highly sloped relief, and the harsh environment. Byrd Glacier is no exception; there is not enough *in situ* ground control to produce accurate elevations from the acquired aerial images. Here, we describe a new methodology that utilizes manually extracted GCPs from a present-day DEM as ground control for the aerial images. This method allows for GCP extraction of mountain peaks and other distant and isolated terrain that would otherwise be near-impossible to measure. Ground features are only of stable, unchanging terrain; we do not use surface features (e.g. ice, permafrost) that may have undergone substantial motion over the past 40 years. While the Transantarctic Mountains are uplifting at a rate of 3.0 mm/yr due to isostatic adjustment from the Last Glacial Maximum (Argus et al., 2014; Peltier et al., 2015), the cumulative uplift of 0.12 m over the 40 years of our study is well within our margin of vertical error.

1.4.1.1 Blunder/Cloud/Shadow Masking

Before GCPs can be identified, the present-day DEM (REMA) is corrected for blunder elevations. These blunders originate from effects of shadows, clouds, and the high degree of nadir with which the imagery was collected. Noh and Howat (2017) acknowledge that the SETSM algorithm has trouble processing some surfaces like shadowed regions, but that this occurs when shadows are just the result of "low sun angles." Conversely to this, other studies have obtained more accurate elevation results from imagery collected at low sun angles (Martha et al., 2010), and we find miscalculated elevations from SETSM-processed imagery collected at both high and low sun angles. To remove potential blunders, we opt for the conservative approach of clipping all shadowed regions within the DEMs, rather than classifying acceptable elevations based on sun angle. Polygons are manually drawn over shadowed regions identified in orthoimagery, and then removed from the DEMs. We ensure that topographic displacement in the orthoimagery is considered by creating polygon boundaries that are larger than the actual shadowed region.

The SETSM algorithm, which is used to create the present-day DEM, does contain a cloud detection component (Noh and Howat, 2015), but it misses a significant percentage of cloud coverage. To ensure cloud-free data, and because it is extremely difficult to determine if the DEM contains clouds solely from looking at the DEM, we follow the technique described in the blunder removal. Each corresponding orthoimage is examined for clouds, manually draw polygons around the clouds, and eliminate these regions from the DEM strips.

The final issue with the present-day DEM results from the high degree of nadir with which the imagery was collected. This high degree of nadir (angle of 10°-30°) means that terrain outside of the satellite's field of view (e.g. the backside of mountains) is not captured. However, the SETSM algorithm does estimate elevations outside of the field of view by filling the regions with results from a RADARSAT-derived DEM, posted at 250 m. We identify the high-nadir shadow zones from both the ortho-imagery and the DEM. In the orthoimagery, these zones appear distorted with a wave-like pattern. In the DEM, there are either clusters of > 4 pixels with the same elevation (due to the lower resolution of the RADARSAT DEM), or very sharp boundaries where perfect rectangles of random values are found. These shadow zones are also manually deleted from the DEM strips.

1.4.1.2 Co-registering/Mosaicking

To ensure accurate relative elevations for the present-day DEMs, each individual DEM strip is registered to the DEM strip immediately down-flow. Registering DEMs is necessary because while the DEMs all have the same ground resolution, their grids are not aligned and even sub-pixel misalignment causes considerable bias when estimating surface elevation change (Nuth and Kääb, 2011; Paul et al., 2015; Paul et al., 2017). Other errors in an elevation dataset, outside of processing – atmospheric effects, steep relief slopes, different sensors used to collect data, time of year – can also cause erroneous elevation values (Paul et al., 2017). Co-registering one DEM to another minimizes these errors (Nuth and Kääb, 2011).

The first step of the co-registration process is to resample all present-day DEM strips from 2 m to 5 m using cubic convolution and projecting them to WGS84 Antarctic Polar Stereographic.

Each DEM is then co-registered to its immediate neighbor using the Python module PyBob, (McNabb, 2018). The co-registration method that is applied (after Nuth and Kääb, 2011) is a robust analytical solution that corrects for bias and errors between DEM pairs by using the pairs' elevation difference residuals and the terrain's aspect and slope. After the strip DEMs are co-registered, they are mosaicked together to create a DEM of the entire glacier.

1.4.1.3 Identifying GCPs

Stable terrain was identified from WorldView imagery orthorectified with REMA by PGC for potential GCP locations. The imagery could not be used to determine absolute locations because the high degree of nadir (> 10°) of many images caused topographic displacement and occlusion effects. Since most image strips were collected at a range of degrees of nadir, the planimetric accuracy varied throughout the entire ortho-dataset. Therefore, the WorldView imagery was only used as a guide. To avoid feature displacement, we choose GCPs that are local elevation high points and easily identifiable within the DEMs. This approach ensures that the error relies solely on the DEMs and not the individual orthoimages.

SfM only requires three GCPs for stereo-processing, but more GCPs provide better bundle adjustment results (Girod et al., 2018). The bundle adjustment estimates accuracy of every GCP and applies it to the processing based on the accuracy of the placed location. A larger number of correctly placed GCPs means the bundle adjustment is more likely to correct misplacements. The exact number of GCPs necessary for accurate elevations varies from project to project, but research shows that more GCPs can improve accuracy to twice that of the image's pixel ground sample distance (GSD) (Agüera-Vega et al., 2017; Sanz-Ablanedo et al., 2018). In classic

photogrammetric processing, accurate results are achieved with evenly distributed GCPs in a triangular grid (Sanz-Ablanedo et al., 2018). This arrangement reduces the horizontal distance to any GCP. In our case study, exposed bedrock is not evenly distributed throughout our study-site making a perfectly distributed grid of triangulated ground control unrealistic.

We initially used 39 GCPs for the 1978 mosaic, and 42 GCPs for the 1979 mosaic, which averages to 1-2 GCPs per image in the mosaic with exposed bedrock. Using so few GCPs means the SfM processing is forced to resolve the XYZ of more features and over larger regions than when more GCPs are applied. Due to Byrd Glacier being ~20 km wide and the spatial coverage width of each photo is ~ 10.5 km, a significant number of aerial images contain no stable terrain. We find that the elevation results for steep terrain and smooth features (e.g. snow) are poor and unrepresentative of the actual terrain. To improve these results, we increase the number of GCPs to 141 and 162 for the 1978 and 1979 image sets. Other studies utilizing SfM processing for glacier elevations also find that increasing the number of GCPs increases the overall accuracy of the final DEM (Gindraux et al., 2017; Tonkin and Midgley, 2016). The DEM's absolute orientation was established by applying at least one GCP and as many as ten GCPs for every image containing exposed bedrock. This modification improved the ground control coverage from a GCP per 57-61 km^2 to one GCP per 17 km^2 .

1.4.2 Elevation Processing

A photographic image is a collection of reflected photons of objects. In the case of analog film, the reflected photons pass through a lens before the light intensity values are recorded (Paine and Kiser, 2012, p. 10). Recorded features on the film are distorted and cannot be used for spatial

analysis until the distortion is corrected. SfM software in conjunction with real world XYZ coordinates correct the distortion and generate surface elevations and orthorectified imagery. In this study, aerial images are processed with a SfM software called MicMac. MicMac is an open-source SfM software written by the National Institute of Geographic and Forestry Information (IGN) and the National School of Geographic Sciences (ENSG) (Rapnik et al., 2017). The SfM software works particularly well for our purposes because some inputs like plane altitude and focal equivalent, which require manual user input in traditional photogrammetry processing, are calculated by the software on the fly.

The SfM processing begins first with resolving the interior orientation to ensure all images contain the same image geometry and is followed by applying a relative coordinate system to the tie points. Absolute XYZ values are manually placed at GCP locations within the images before running the bundle adjustment. The final step is stereo-matching, where XYZ values are estimated and output as a 3-dimensional point cloud.

Image Set	# of Images	Flight Path Length (km)	# of Tie Points (millions)	# of GCPs
1978	141	560.316	3.7	143
1979	162	509.300	2.7	136

Table 1.1: Image set parameters

1.4.2.1 Interior Orientation

Digital imagery contains EXIF metadata, which includes film geometry and camera calibration information, in a file that is necessary for estimating relief from an image. Digital scans of analogue film, like the Byrd Glacier imagery, do not have an EXIF file so the file must be manually generated. The USGS has a camera calibration report, but this information only applies

to the actual film and not to the digital scans. In our images, the fiducial mark locations on the scanned film do not match those reported by the USGS. This offset is likely film distortion due to non-ideal storage conditions, and asymmetrical scanning of each negative. The analogue film geometry is in a coordinate system where the image grid columns are X and rows Y and units are in millimeters. To process the imagery in MicMac, this coordinate system has to be established for the digital scans. We determine the film geometry by measuring in Photoshop the distance between the N-S and W-E fiducial marks (vertical and horizontal directions respectively) in millimeters. The XY coordinates of the four fiducial mark locations are also located in Photoshop. The four fiducial marks of each image are then manually identified in MicMac to apply the coordinate system to the digital scans. This step is necessary because minor shifting of the film occurred during the scanning process which causes the XY coordinates of the fiducial marks to vary in the digital scans and can affect the amount of necessary overlap between images. Identifying the fiducial marks also establishes the interior boundary of the image. We resample the images to a resolution of 25 microns and create a normalized geometry. Figure 1.2B is a schematic showing the result of normalizing a skewed digitized photograph. Normalizing ensues that all of the images contain the same pixel size and grid alignment, without which tie point identification would be impossible.

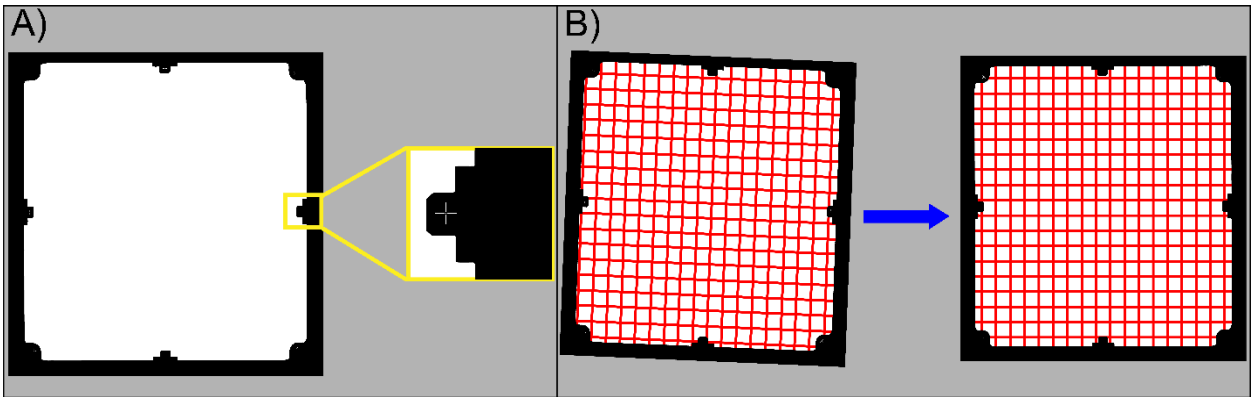

Figure 1.2: Establishing interior orientation: A) The "skeleton" of an aerial image with the border and the actual image whited out. The yellow box is highlighting 1 of the 4 fiducial marks and the callout to the right is an enlargement of that fiducial mark. B) The process of normalizing the aerial photographs where each image is positioned with the same grid spacing and alignment.

1.4.2.2 Relative Orientation

Using the normalized images, MicMac identifies common features (e.g. tie points) within each image using the Scale-Invariant Feature Transformation (SIFT) algorithm (Lowe, 2004). All of the images have black borders and some text containing information about the flight. Unfortunately, the software treats the border and text as ground features and includes them in the initial tie point extraction. We manually mask out the text and borders for each image. We also mask out the white stripes visible in the 1978 dataset. After masking, 3.7 million tie points for the 1978 data and 2.7 million tie points for the 1979 data remain. The additional million tie points in the 1978 set are attributed primarily to one cross flight path flown that day. We estimate relative locations (image coordinates in millimeters) of the tie points using the Fraser (1997) calibrated distortion model. Camera distortion parameters are calculated using the least squares method which iterates until the calculated residuals reach an optimal value. The resulting average residuals for the two sets of data are 0.91 and 0.95 of a pixel (~1.2 m). The image (relative) coordinates are what the software employs to perform a transformation between real-world and image XYZ position.

1.4.2.3 Absolute Orientation

GCPs identified from the present-day DEMs are applied to the relative coordinate system of the tie points to relate the tie points to real-world (absolute) ground positioning. The GCPs are manually positioned in the aerial imagery in MicMac. The interior image information is then transferred to absolute XYZ values of the GCPs. Following this, a bundle adjustment is executed to minimize error between light-ray bundles and GCP locations by adjusting the camera's orientation and position (Triggs et al., 1999). The residuals calculated by the bundle adjustment represent the distance the GCPs are estimated as "offset" from the manually placed GCPs. For the 1978 and 1979 image set, the average residuals are 1.00 and 0.96 pixels, respectively. These pixel residual values are comparable to errors quoted by other studies using historic aerial imagery (Magnússon et al., 2016). The bulk application residuals provide one resource for the overall error of the GCPs and the distance to its corresponding point in the point cloud.

Image Set	GCP Average Residual (pixels)	X-Shift (m)	Y-Shift (m)	Z-Shift (m)	Reprojection Error (pixels)
1978	1.005	-0.077	0.058	0.037	3.062
1979	0.959	-0.005	-0.015	0.029	2.046

Table 1.2: Bundle adjustment shifts after 8 iterations

1.4.2.4 DEM

The final step is to use the geolocated aerial images to create gridded DEMs. MicMac generates latitude and longitude coordinates with elevations in the form of point clouds, which first need to be filtered for spurious points which is done in the software CloudCompare. Spurious points are points outside of the known local minimum and maximum elevations, as well as points that are clearly erroneous elevations. Potential causes of such points are bad radiometric calibration,

homogeneous features, film distortion, and inaccurately placed GCPs. We convert filtered point clouds into gridded raster format. Gridded elevation values are an average of the points that fall within a given grid cell (CloudCompare Documentation).

MicMac produces data at 1 m spacing, but after editing the point clouds, we produce a gridded 10 m DEM for both 1978 and 1979 datasets. We find that this coarser resolution still represents the ground terrain well and also acts to fill in data gaps that would otherwise remain at the 1 m resolution.

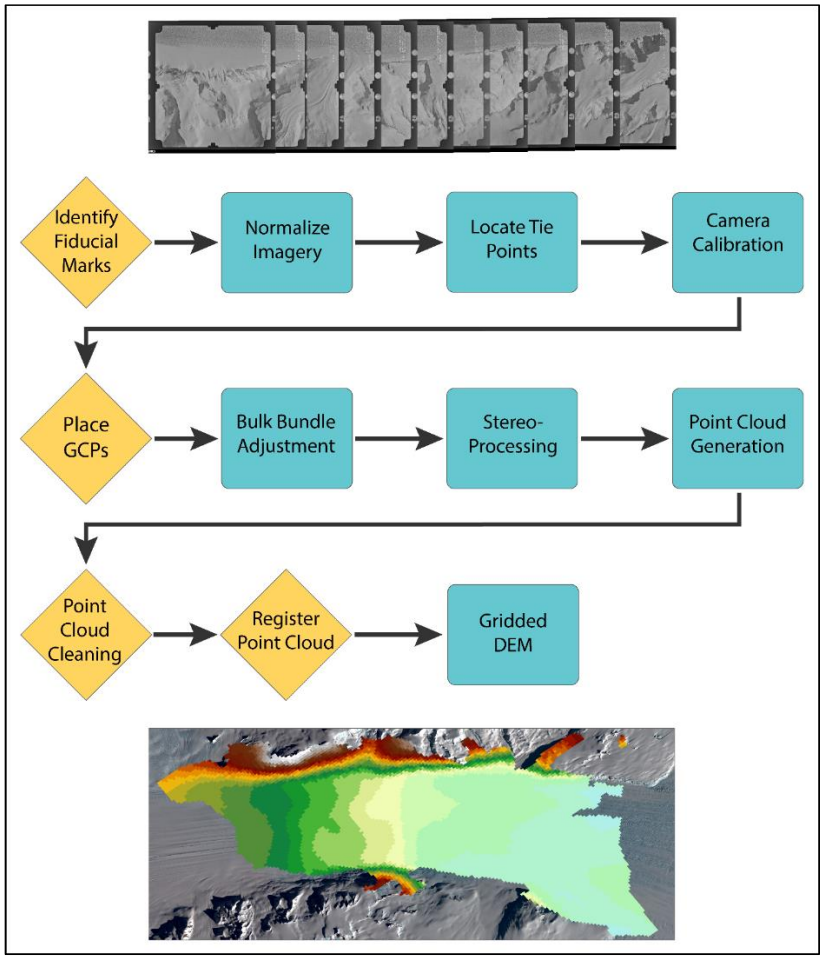

Figure 1.3: Workflow of SfM processing steps to use historic aerial images to produce a gridded DEM. Yellow diamond shapes represent manual processing steps; the teal rectangles are automated steps. The DEM at the bottom of the figure is a very course version (1,000 m resolution) of the 1979 results.

1.4.3 Velocity

White stripes in the 1978 set of images make it impossible for the SfM processing to produce an orthorectified mosaic. This means that we are unable to derive any glacier surface velocities from feature tracking of optical imagery, which is the traditional method for deriving velocities from optical images (Scambos et al., 1992; Fahnestock et al., 1992). Instead, we use surface slopes, which are a biproduct of the DEMs that we generate from the historical images. Velocity determined from feature tracking techniques requires that elements within a data set remain the same from one time period to the next in order to track their displacement. While elevations will change between epochs, over a short time period (56 days) the relative shape of the terrain, such as the slope, remains fairly constant.

We estimate velocities using the Optically Sensed Images and Correlation (COSI-Corr) software. COSI-Corr tracks the displacement of features between two images, outputting a grid of displacement values (Leprince et al., 2007). The software also produces a grid of signal to noise ratio (SNR). SNR allows us to assess the quality of the calculated correlation. We discard any values with an SNR >0.9 pixels and manually edit the velocities to remove vectors with bearings that are not in the same direction as ice flow (~5%).

1.4.4 Data Validation

Factors likely to influence the accuracy of SfM processing of historic aerial imagery are film distortion, < 60% of overlap between images, incorrect elevation values from the present-day DEM, and misplacement of GCPs. To determine how well our methodology works for deriving DEMs from analog film with manually located GCPs, we estimate the vertical error in the

historic elevations. The vertical error is assessed by comparing the stable terrain of the historic DEMs with independent present-day elevations, present-day DEMs, and one historic DEM to another. We also compare our results with the elevations calculated by Brecher (1982).

1.4.4.1 DEM Registration

Before any validation is carried out, and the point clouds are converted to grid format, both point clouds are registered to the GPS data in CloudCompare. Aerial images are draped over the point cloud to increase the accuracy of our GPS placement on the images (Figure 1.4). We recognize that three *in situ* data points is less than the optimal number of GCPs needed to accurately register an image (Barrand et al., 2009), but this is the only absolute elevation data of stable terrain available for Byrd Glacier.

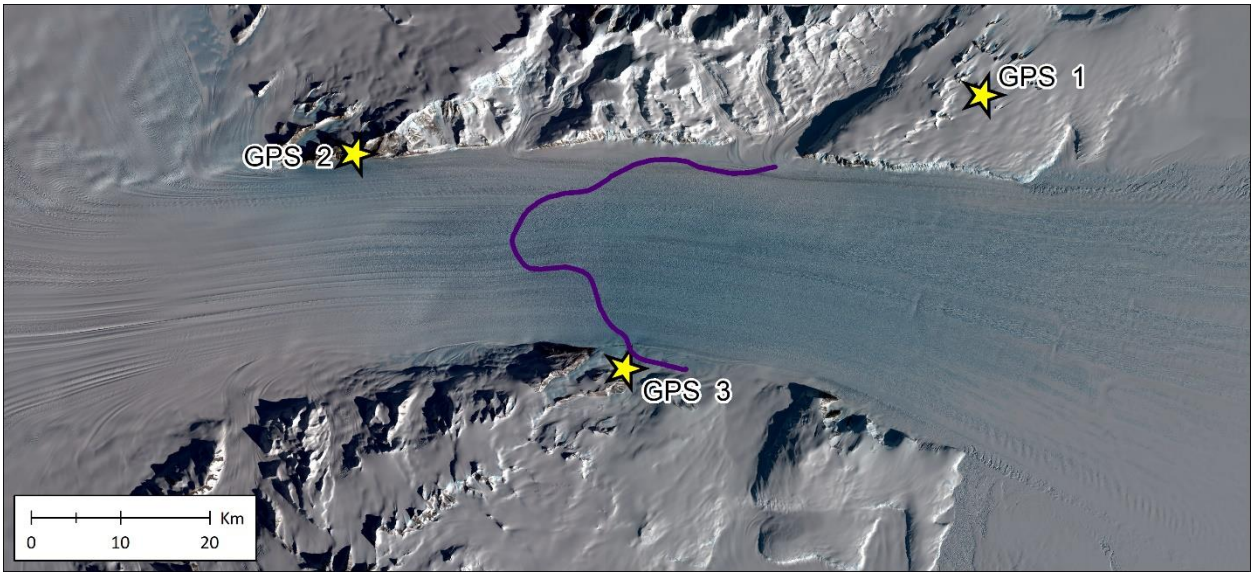

Figure 1.4: GPS locations represented by stars.

1.4.4.2 Data Comparison

1.4.4.2.1 Elevations

When the historic images were originally processed in 1980, the results had a horizontal and vertical datum projected in International 1924 (Brecher, 1982). The SfM DEMs that we produce in this study are projected in reference to the WGS84 ellipsoid. As a result, the 1980 grids had to be transformed to the same ellipsoid in order to complete our comparison. To transform the data to the WGS84 ellipsoid, we use a local geodetic datum with the Standard Molodensky three-parameter ($\Delta\phi,\ \Delta\lambda,\ \Delta h$) formula (NIMA, 2000):

$$\begin{aligned} \phi_{WGS84} &= \phi_{Local} + \Delta\phi \\ \lambda_{WGS84} &= \lambda_{Local} + \Delta\lambda \\ h_{WGS84} &= h_{Local} + \Delta h \end{aligned} \qquad (1.1)$$

Where ϕ_{Local}, λ_{Local}, and h_{Local} are local geodetic latitude, longitude, and elevation, respectively. In this case, the local geodetic datum and shift parameters are referenced from the 1987 Camp McMurdo Area, Antarctica (Boyle, 1987).

The elevations derived in the 1980s do not have spatial coverage beyond the glacier boundaries (Brecher, 1982), which means that the original dataset does not have any XYZ values on stable terrain. This issue was resolved in Schenk et al. (2005) by reprocessing small sections of the imagery along four regions on the edge of the glacier, but that is beyond the scope of our study. Consequently, Brecher's (1982) results could not be registered to the SfM results, and we cannot

do a direct comparison. Instead, we conduct a relative comparison by calculating the r-squared values of vertical differences between the Brecher (1982) elevations and the SfM elevations.

1.4.4.2.2 Velocities

The velocities that were manually derived in the 1980s are presented solely as speed contours (Brecher, 1982). To compare our velocity results, derived from slope feature-tracking, with these historic velocities, we first need to convert the contours to a raster grid with a spatial resolution of 500 m. Like the Brecher (1982) elevation dataset, the Brecher (1982) velocity spatial coverage does not extend to any stable terrain.

1.5 Results and Discussion

1.5.1 DEM Products

The point cloud generated from the 1978 mosaic of historic aerial photographs contains ~52 million points, and the point cloud from the 1979 mosaic contains ~33 million points. Both DEMs cover ~2400 km^2 over the lower trunk of Byrd Glacier (see Figure 1.5 for results). The extents of the two mosaics differ slightly due to image overlap and flight path. In regions where image overlap was < 60%, spurious points were apparent in the point cloud and filtered. These regions include the southern downflow region in the 1978 dataset and the southern up-flow region in the 1979 set. For those images with 60% or more overlap, the SfM processing performed extremely well over regions of exposed bedrock and crevassing.

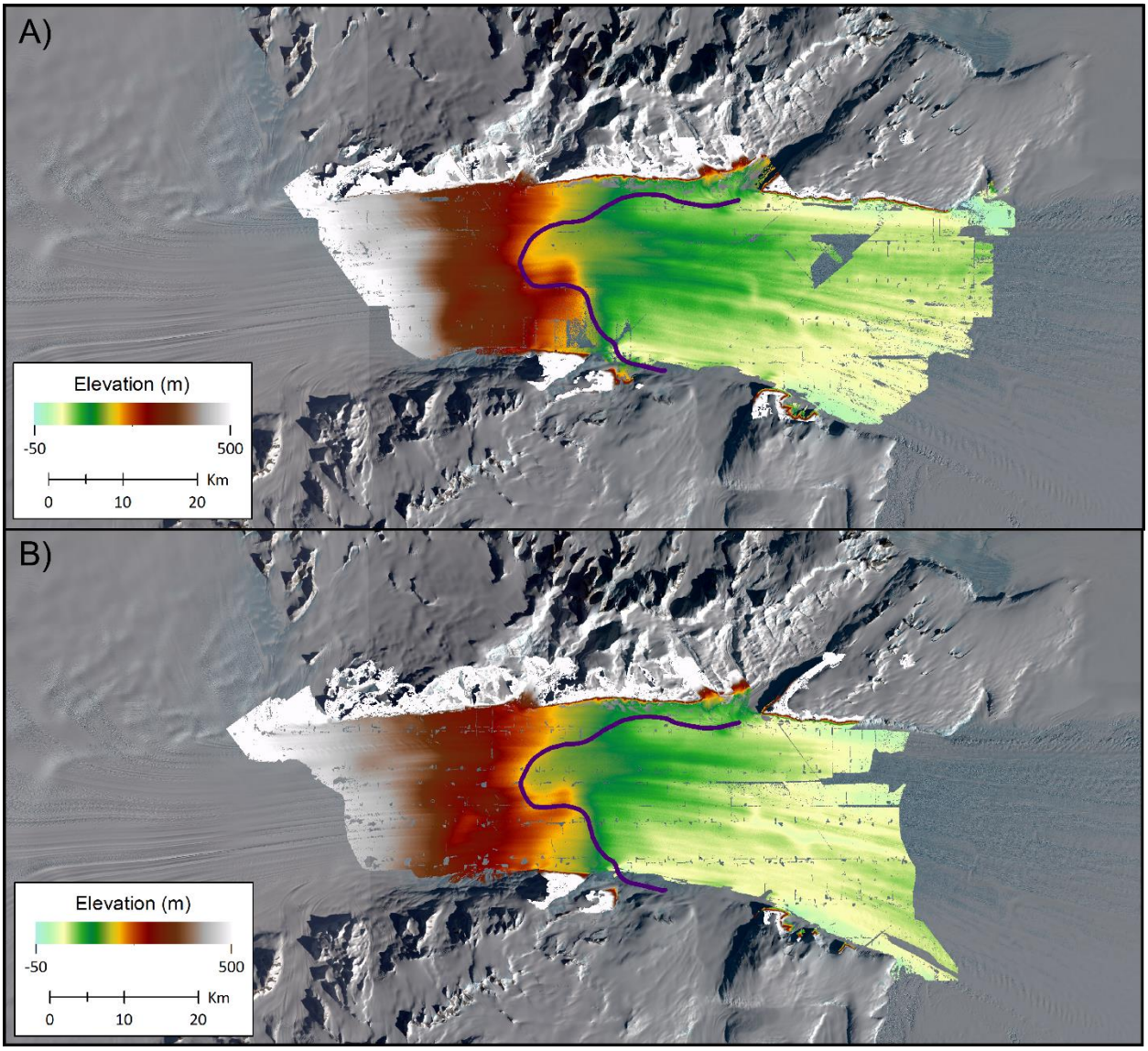

Figure 1.5: 10m DEM results for the 1978 (A) and 1979 (B) image sets. The upper end of the elevation scale is set to 550m to highlight the glacier's surface features, and the violet line represents the grounding zone which is calculated from hydrostatic equilibrium.

Our results show that increasing the number of GCPs did help improve elevations for extremely steep relief and over-hanging cliffs. Unfortunately, increasing the number of GCPs on the stable terrain did nothing to improve the processing of non-textured features such as smooth snow. A significant portion of Byrd Glacier is covered in surface crevasses, so this did not affect the

majority of the main trunk, but it did mean that large expanses of the surrounding solely snow-covered terrain was eliminated due to incorrect elevations.

Brecher's (1982) elevation data is made up of 1,467 irregularly distributed discrete points along the entirety of Byrd Glacier. When the data is interpolated to a 500 m grid (Figure 1.6), the point density causes "bulls-eyes" in the raster. The coarse resolution (500 m) makes it difficult to directly compare with the high-resolution (10 m) SfM DEMs. Instead, we calculate the elevation differences at the discrete points rather than each interpolated grid cell.

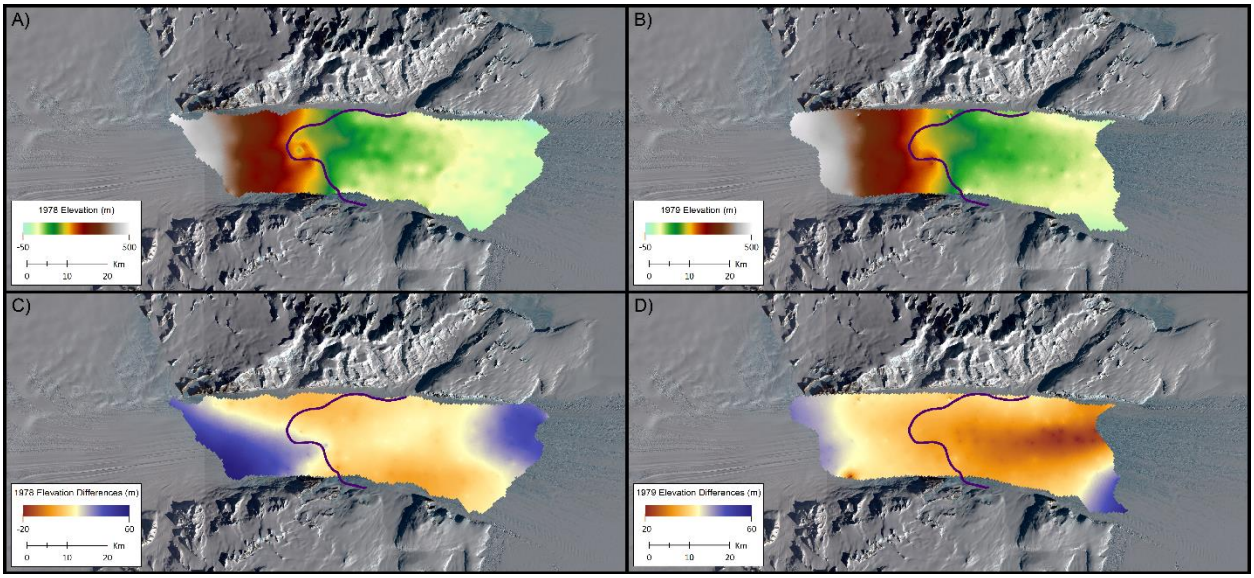

Figure 1.6: 1978 (A) and 1979 (B) DEMs interpolated from the XYZ values transferred from the International 1924 ellipsoid. C and D are the 1978 and 1978 results from differencing the originally processed elevations from the SfM elevations.

Differencing the manually generated DEMs with the SfM DEMs results in a mean of -21.88 m (1978) and -10.26 m (1979) with standard deviations of 14.79 and 14.17 respectively. The RMSE for both the 1978 and 1979 DEMs is 2.09 m. One possible cause for the mean elevation difference to be so high is the ellipsoid transformation. The XYZ shift calculated from the

Standard Molodensky method has a total accuracy of 5-10 m (Janssen, 2009, ICSM, 2014). Without any stable terrain coverage, there is no way of registering the SfM DEMs with the Brecher (1982) data points. Nuth and Kääb (2011) found that co-registering various elevation datasets resulted in a correction of 5-70% of a shifted gridded dataset. It is very likely the if these 1980 processed data were registered with the SfM elevations that the mean difference of DEM (DoD) would be significantly less.

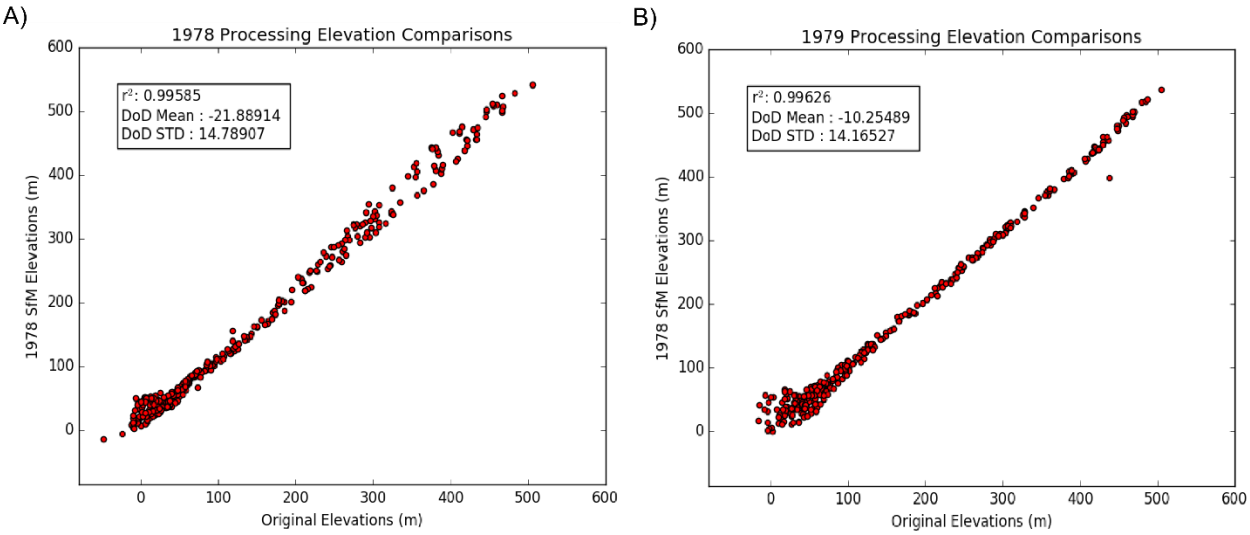

Figure 1.7: Scatter plots of the original DEM processing values with the SfM processing elevations for 1978 (A) and 1979 (B).

1.5.2 DEM Error Analysis

The validity of the SfM DEMs is assessed workflow by calculating the RMSE and standard deviation of various elevation differences. The RMSE of the DEM grids post-point cloud registration to the GPS data is 0.50 m (1978) and 2.30 m (1979). The two SfM DEMs were compared for all exposed bedrock, regardless of slope, and the average elevation difference for the two sets (N = 546,302) is -4.08 m with a σ of 15.45 m. The same calculation is performed

over exclusively stable terrain (slope < 20°), which results in a new mean of (N = 153,343) is -8.33 m, and the σ is 7.57 m.

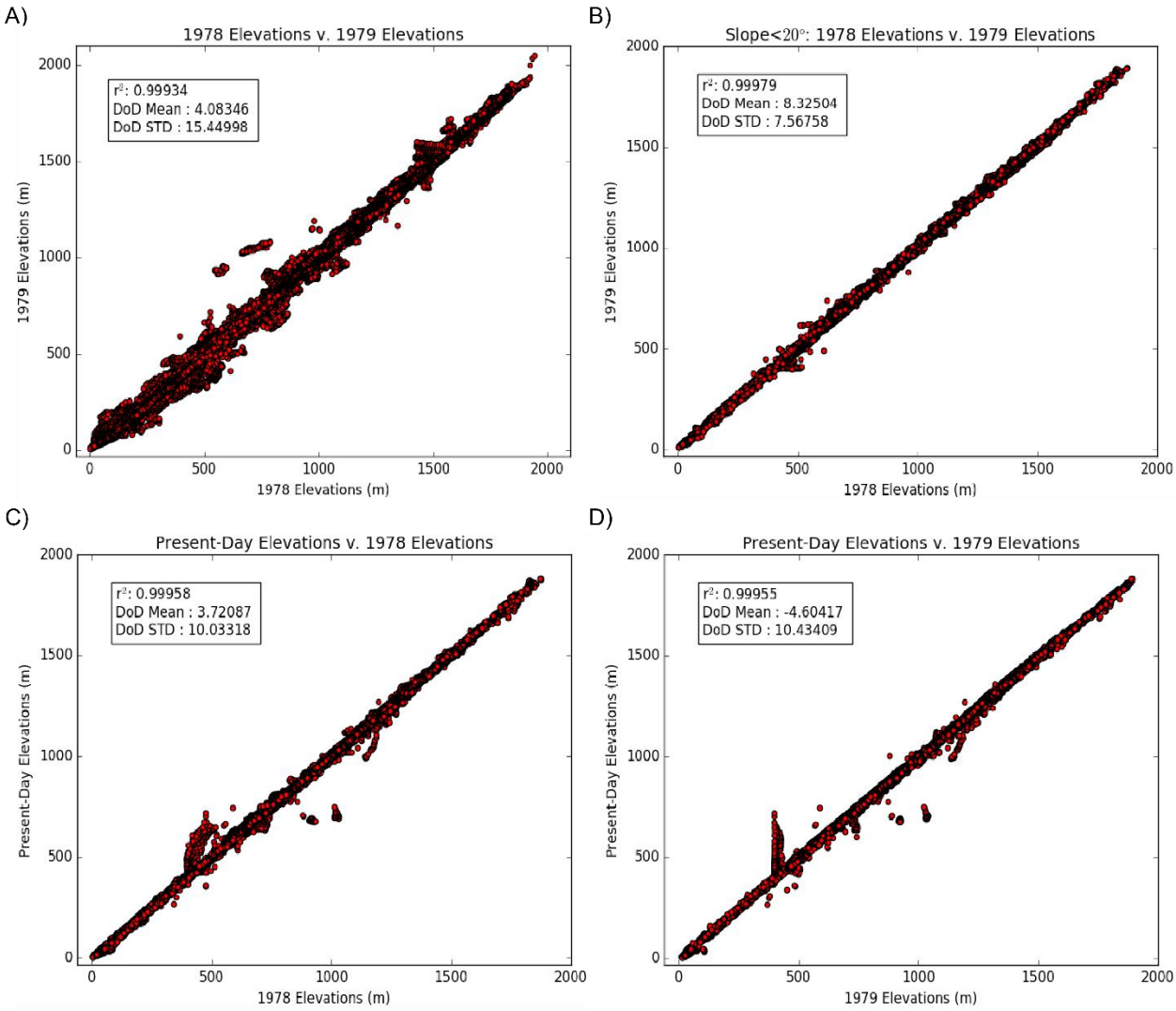

Figure 1.8: DEMs of difference (DoD) of historical DEMs and stable terrain: Mean and DoD STD values are the mean and standard deviations (in meters) of the elevation differences calculated from the plotted variables. A) Scatter plot of the 1978 elevations and the 1979 elevations over stable terrain. B) Scatter plot of the 1978 elevations and the present-day elevations for stable terrain < 20°.

Comparisons of both DEMs to the present-day DEM over bedrock where slope is < 20°reveal the mean difference for 1978 and 1979 is 3.72 m and -4.60 m; the RMSE is 10.03 m and 10.43 m. Outliers in Figure 1.8 C and D are caused by the present-day DEM (in particular, around the 500,

500 location), which are located near cliff edges where the SRTSM algorithm has difficulty rendering elevation values.

1.5.3 Velocity

Velocities derived from feature tracking of surface elevation slopes produces speeds that range in value from ~600 to ~875 m/yr. These values agree well with Brecher (1982) and with the field study conducted at the same time as the aerial data collection (Hughes and Fastook, 1981). Unfortunately, the results cannot be further validated because there are no available satellite images collected during December 1978 and January 1979 or other velocity products.

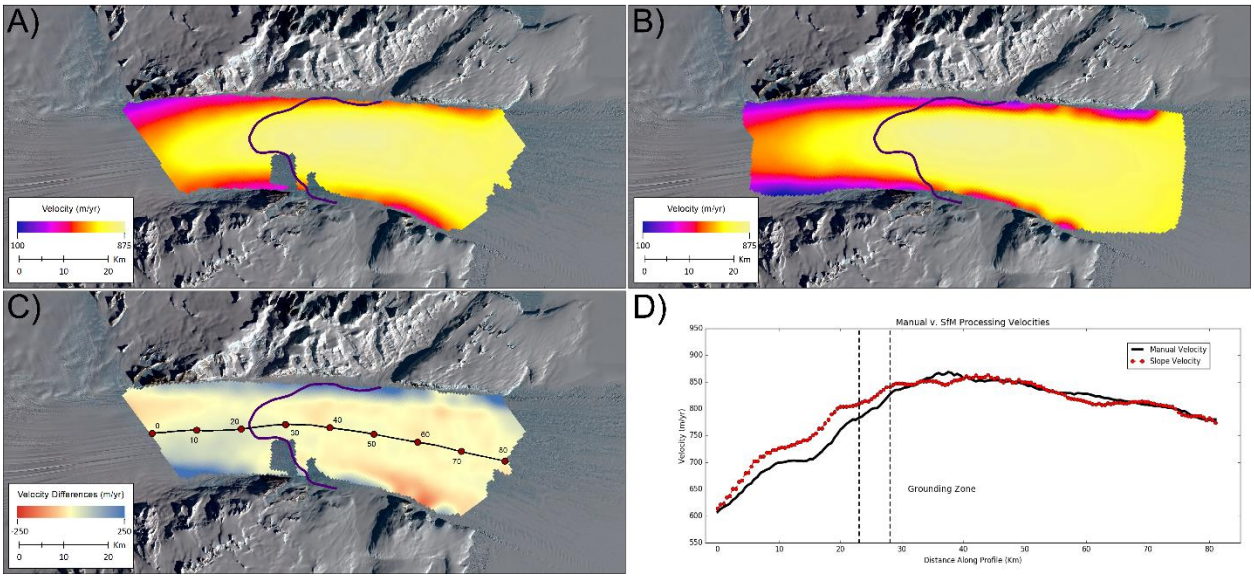

Figure 1.9: Velocity products: (A) Velocities from elevation slopes—the missing section in the middle of the grid is due to poor correlations and the space was too large to interpolate accurate magnitudes. B) Brecher (1982) gridded velocities from contours. C) Difference map of the two velocities. The line and labeled points correlate with the profile plot in D. The points represent points along the profile in Kilometers. D) Profile of the black central line from A, B, and C of both velocities.

We calculate the velocity differences by subtracting the slope velocity from the original velocity data. The mean and standard deviation of the velocity differences (N = 6,974) are -21.93 m/yr

and 61.63 m/yr, respectively. The majority of the difference values ±100 m/yr are located on the edges of the glacier which is where several of the COSI-Corr results contained NoData gaps. These large values are likely due to the interpolation of the slope velocities. After removing all differences outside of one standard deviation (N = 5,767), the mean then becomes 0.44 m/yr and the standard deviation 28.58 m/yr.

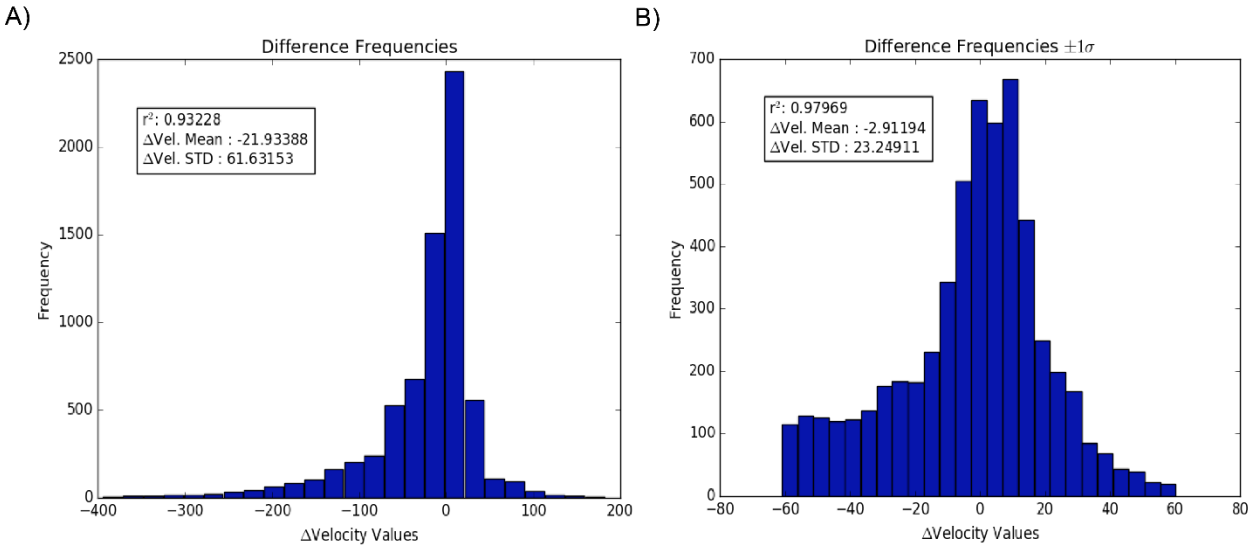

Figure 1.10: Velocity differencing frequency histograms: Frequency histogram of all of the velocity (m/yr) differences (A) and frequency histogram of differences that fall within one standard deviation of the mean (B).

1.5.4 Data Observations

1.5.4.1 Grounding Line Migration

The grounding line is the location where the glacier shifts from being grounded on bedrock, to floating on the ocean and the grounding zone is the region where this transition occurs. Migration of the grounding line's position is an indicator of a glacier losing or gaining in mass (Konrad et al., 2018). Reusch and Hughes (2003) estimate Byrd Glacier's grounding line migration by comparing 1978/79 field work results of tidally influenced elevation changes with the boundary of hydraulic equilibrium calculated by Rignot and Jacobs (2002). The 1978/79

fieldwork did not identify the grounding line, but instead the glacier's point of flexure (Hughes and Fastook, 1981). The point of flexure and the hydrostatic equilibrium boundary make up the up and down flow limits of the grounding zone and their locations can differ by as much as 10 km (Brunt et al., 2010). In assuming these two different boundaries of the grounding zone are the actual grounding line, Reusch and Hughes (2003) conclude that Byrd Glacier's grounding line has migrated ~20 km upstream, which is an indicator the Glacier has been losing mass. These conclusions were reassessed comparing hydraulic equilibrium boundary migration for the last ~40 years. The boundaries were estimated using the 1979 SfM high-resolution DEMs and the present-day DEM with ice thickness data collected by the Center for Remote Sensing of Ice Sheets (CReSIS). Hydrostatic equilibrium is calculated by:

$$\Delta h' = \bar{h} - \frac{z(\rho_w - \rho_i)}{\rho_w}, \qquad (1.2)$$

where, $\bar{h}$ is the surface elevation, z the ice thickness, ρ_w is the density of ocean water and ρ_i the density of ice. A glacier is in hydrostatic equilibrium where equation 1.2 is approximately 0. Both the present-day and historic equilibrium boundaries are mapped in Figure 1.11. The 1979 equilibrium boundary is located slightly downflow of the present-day DEM boundary by ~800m.

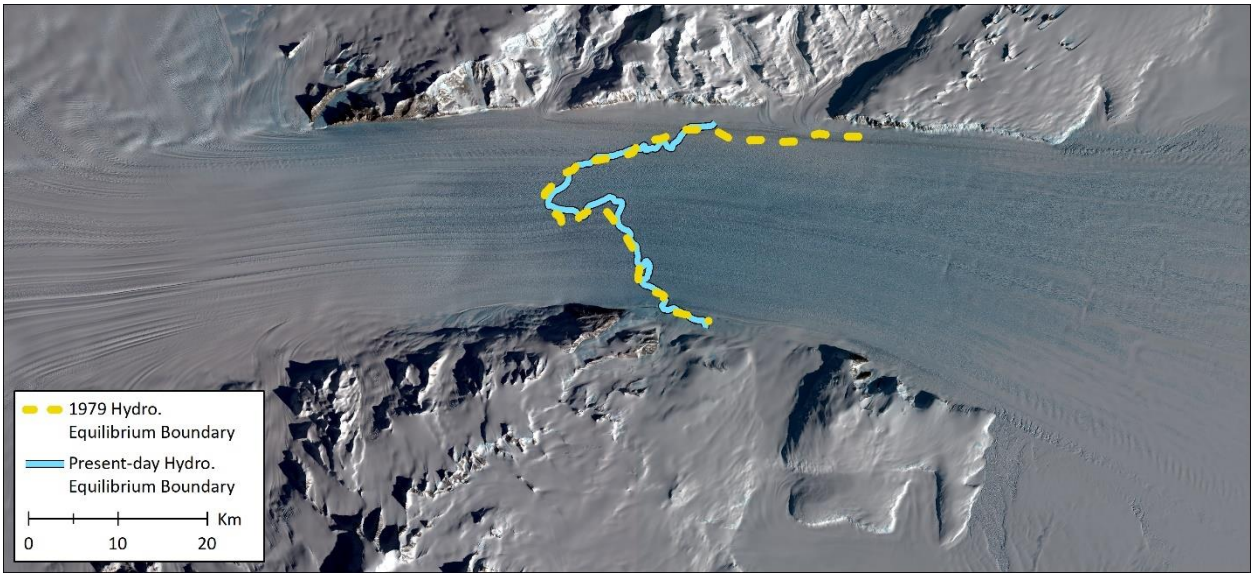

Figure 1.11: The hydrostatic equilibrium boundaries, calculated from both elevation sets, representing the grounding line. The cyan line represents the present-day hydrostatic equilibrium and the yellow dashed line the 1979 boundary.

One possible source for differences in these hydrostatic equilibrium boundaries is the variability in grid resolutions from datasets (CReSIS ice thickness grid: 500 m; SfM DEM: 10 m; present-day DEM: 5 m). Another potential cause for differences in boundary locations could be due to changes in the ice bottom surface from new crevassing, evolving subglacial tunnels, and melting. The thickness data were collected in the 2011-2012 austral summer, so it is expected that any changes in basal crevasses or melt would mean the basal surface from 1979 would be altered 33 years later. While the exact reasons are beyond the scope of this study, it seems likely that the conclusion drawn by Reusch and Hughes (2003) was incorrect and due likely to comparing two separate components of the grounding zone.

1.5.4.2 Surface Depressions

Surface depressions on Byrd Glacier, found on the floating portion of the trunk, are located directly above basal crevasses. We observe from satellite imagery that these depressions remain

visible for decades within the trunk and continue to persist as features in the ice surface as ice flows from Byrd Glacier to the terminus of the Ross Ice. The geometry of these depressions evolves (e.g. changes in concavity), and we assume this is a result of the changing geometry of the underlying basal crevasse. Highly detailed elevation data from different time periods provide information about the changing conditions of the glacier's basal surface.

Figure 1.12 highlights a surface depression in the 1979 DEM and the present-day DEM. We know this depression is directly above a basal crevasse from radar echogram data and observations of other basal crevasses/surface depression that manifested post-1979 data collection. This surface depression has migrated ~30.5 km over the 38-year period the historical data and the present-day satellite data were collected. The depression depth in 1979 is ~34 m and it shallows to ~22 m in 2017. Assuming uniform change, the depression has undergone a depth decrease of ~0.32 m/yr.

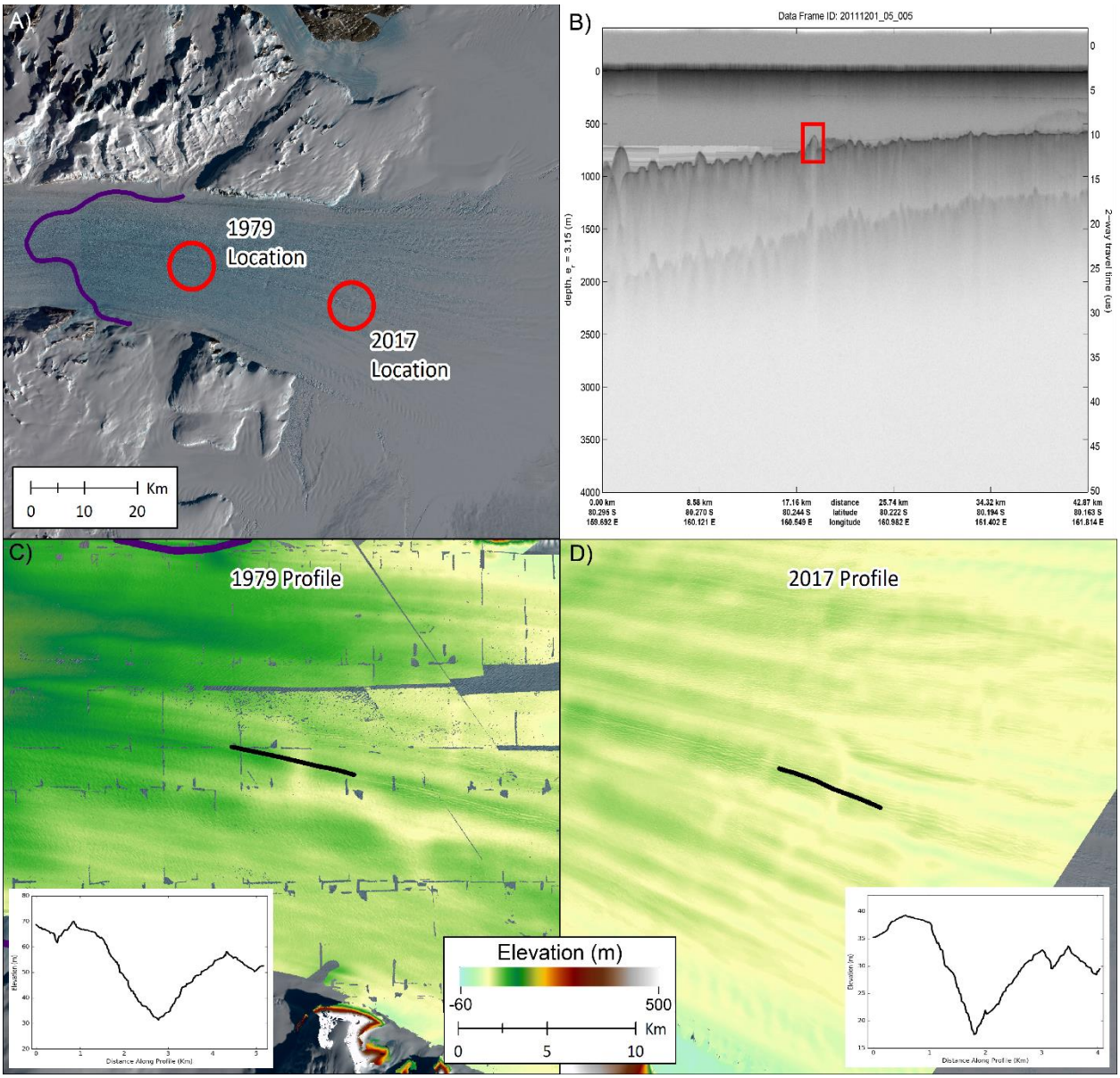

Figure 1.12: Surface depression geometry: A) The surface depression locations in 1979 and 2017, circled in red. B) CReSIS echogram collected in 2011. The basal crevasse responsible for the surface depression is in the red box. C) and D) are the 1979 and 2017 DEMs with black lines over the depressions and plots of the surface elevations in the lower left and right corners.

1.6 Conclusion

We find that using manually extracted GCPs to apply absolute locations to historic aerial imagery in SfM processing produces accurate results without requiring *in situ*, evenly spaced

ground control, or other traditionally necessary photogrammetric parameters like flight altitude and photo center XY. The elevation comparisons of both historic DEMs with present-day DEMs gives an average vertical error of the processing of ~1.4m. The grid spatial resolution and error estimate are of comparable quality to digitally processed modern-day data that the SfM historic results may be used in further analysis of glacier dynamics.

The process requires a large manual component that is non-trivial, but cost-effective, and the results are DEMs of spatial resolutions never available to researchers at the time of original processing. Re-processing historic data with latest SfM methodologies produces high resolution DEMs of glacier surface that have never been observed before. Such high resolutions allow for better analysis of glacier dynamic evolution by better constraining elevation and validating time-dependent modelling. We show this by modeling the hydrostatic equilibrium boundary of Byrd Glacier using both the historic and present-day DEMs. Our results contrast previous studies that modeled the grounding zone as migrating significantly inland and concluded Byrd Glacier as a risk for being unstable. Our high-resolution SfM results instead show that the grounding zone of Byrd Glacier has remained stable for the past ~40 years. Unfortunately, for the rest of Antarctica, high density aerial image coverage from a single flight campaign is rare, but over ~175,000 oblique aerial images were collected from the 1940s to the 1970s that require significantly less images to cover the same spatial area. This methodology will be applied to future research using trimetrogon aerial imagery collected in the 1960s, for better understanding surface elevation changes of the largest outlet glaciers flowing through the Transantarctic Mountains.

Chapter 1 Citations

Agüera-Vega, F., Carvajal-Ramírez, F., and Martínez-Carricondo, P. (2017). Assessment of photogrammetric mapping accuracy based on variation ground control points number using unmanned aerial vehicle. *Measurement, 98*, 221-227.

Anisimov, O.A., Vaughan, D.G., Callaghan, T.V., Furgal, C., Marchant, H. Prowse, T.D., Vilhjálmsson, H., and Walsh, J.E. (2007). Polar regions (Arctic and Antarctic). *Climate Change 2007: Impacts, Adaptation and Vulnerability. Contribution of Working Group II to the Fourth Assessment Report of the Intergovernmental Panel on Climate Change*, Parry, M.L., Canziani, O.F., Palutikof, J.P., van der Linden, P.J., and Hanson, C.E. Eds., Cambridge University Press, Cambridge, 653-685.

Barrand, N. E., Murray, T., James, T.D., Barr, S.L., and Mills, J.P. (2009) "Optimizing photogrammetric DEMs for glacier volume change assessment using laser-scanning derived ground-control points." *Journal of Glaciology, 55*(189), 106-116.

Boyle, M. J. (1987). *Department of Defense World Geodetic System 1984-It's definition and relationship with local geodetic systems*. DMA Technical Report 83502.2., Washington, D.C.

Bjørk, A.A., Kjær, K.H., Korsgaard, N.J., Khan, S.A., Kjeldsen, K.K., Andresen, C.S., Box, J.E., Larsen, N.K., and Funder, S. (2012). An aerial view of 80 years of climate-related glacier fluctuations in southeast Greenland. *Nature Geoscience, 5*(6), 427-432.

Brecher, H.H. (1982). Photographic determination of surface velocities and elevations on Byrd Glacier. *Antarctic Journal. US*, *17*(5), 79-81.

Brecher, H. H. "Velocity data for Byrd Glacier." National Snow and Ice Data Center. https://nsidc.org/sites/nsidc.org/files/files/byrd_velmap.txt, April 13, 2017.

Brunt, K.M., Fricker, H.A., Padman, L., Scambos, T.A., and O'Neel, S. (2010). Mapping the grounding zone of the Ross Ice Shelf, Antarctica, using ICESat laser altimetry. *Annals of Glaciology*, *51*(55), 71-79.

Burton-Johnson, A., Black, M., Fretwell, P., and Kaluza-Gilbert, J. (2016). An automated methodology for differentiating rock from snow, clouds and sea in Antarctica from Landsat 8 imagery: a new rock outcrop map and area estimation for the entire Antarctic continent. *The Cryosphere*, *10*, 1665-1677.

Carter, S.P., Fricker, H.A., and Siegfried, M.R. (2017). Antarctic subglacial lakes drain through sediment-floored canals: theory and model testing on real and idealized domains. *The Cryosphere*, *11*, 381-405.

Compare, Cloud. "User manual version 2.6. 1." (2017).

Cook, A.J., Fox, A.J., Vaughan, D.G., and Ferrigno, J.G. (2005). Retreating glacier fronts on the Antarctic Peninsula over the past half-century. *Science, 308*(5721), 541-544.

DigitalGlobe, (2014). Geolocation Accuracy of WorldView Products (White Paper).

Fahnestock, M.A., Scambos, T.A., and Bindschadler, R.A. (1992). Semi-automated ice velocity determination from satellite imagery. *Eos, 73*, 493.

Fox, A.J. and Cziferszky, A. (2008). Unlocking the time capsule of historic aerial photography to measure changes in Antarctic Peninsula glaciers. *The Photogrammetric Record, 23*(121), 51-68.

Fraser, C.S. (1997). Digital camera self-calibration. *ISPRS Journal of Photogrammetry and Remote Sensing, 52*(4), 149-159.

Fricker, H.A., Coleman, R., Padman, L., Scambos, T.A., Bohlander, J., and Brunt, K.M. (2009). Mapping the grounding zone of the Amery Ice Shelf, East Antarctica using InSAR, MODIS and ICESat. *Antarctic Science, 21*(5), 515-532.

Gindraux, S., Boesch, R., and Farinotti, D. (2017). Accuracy assessment of digital surface models from unmanned aerial vehicles' imagery on glaciers. *Remote Sensing, 9*(186).

Girod, L., Nielsen, N.I., Couderette, F., Nuth, C., and Kääb, A. (2018). Precise DEM extraction from Svalbard using 1936 high oblique imagery. *Geoscientific Instrumentation, Methods and Data Systems, 7*(4), 277-288.

Guzzetti, F., Mondini, A.C., Cardinali, M., Fiorucci, F., Santangelo, M., and Chang, K.T. (2012). Landslide inventory maps: New tools for an old problem. *Earth-Science Reviews, 112*(1-2), 42-66.

Howat, I.M., Porter, C., Smith, B.E., Noh, M.J., and Morin, P. (2019). The reference elevation model of Antarctica. *The Cryosphere, 13*(2), 665-674.

Hughes, T.J. and Fastook, J.L. (1981). Byrd Glacier: 1978–1979 field results. *Antarctic Journal US, 16*(5), 86-89.

ICSM. (2014). Geocentric Datum of Australia Technical Manual, Version 2.4.

Janssen, V. (2009). Understanding coordinate reference systems, datums and transformations. *International Journal of Geoinformatics, 5*(4), 41-53.

Konrad, H., Shepherd, A., Gilbert, L., Hogg, A.E., McMillan, M., Muir, A., and Slater, T. (2018). Net retreat of Antarctic glacier grounding lines. *Nature Geoscience, 11*(4), 258-262.

Kraus, K., Harley, I. A., and Kyle, S. (2011). *Photogrammetry. Geometry from Images and Laser Scans*. Berlin, Boston: De Gruyter.

Leprince, S., Barbot, S., Ayoub, F., and Avouac, J. (2007). Automatic and precise orthorectification, coregistration, and subpixel correlation of satellite images, application to ground deformation measurements. *IEEE Transactions on Geoscience and Remote Sensing, 45*(6), 1529-1558.

Lowe, D. G. (2004). Distinctive image features from scale-invariant keypoints. *International journal of computer vision, 60*(2), 91-110.

Magnússon, E., Belart, J.M.C., Pálsson, F., Ágústsson, H., and Crochet, P. (2015). Geodetic mass balance record with rigorous uncertainty estimates deduced from aerial photographs and LiDAR data-case study from Drangajökull ice cap, NW-Iceland. *Cryosphere Discussions*, *9*(5).

Martha, T.R., Kerle, N., van Westen, C.J., Jetten, V., and Vinod Kumar, K. (2010). Effect of sun elevation angle on DSMs derived from Cartosat-1 data. *Photogrammetric Engineering and Remote Sensing*, *76*(4), 429-438.

McNabb, Robert. (2019). PyBob: A Python package of geospatial tools, v0.25.

National Imagery and Mapping Agency Technical Report 8350.2, Third Edition. (2000). National Imagery and Mapping Agency, 3 January 2000.

Nielsen, N.I. (2017). *Recovering Data with Digital Photogrammetry and Image Analysis Using Open Source Software*. Master's thesis, University of Oslo.

Noh, M.J. and Howat, I.M. (2015). Automated stereo-photogrammetric DEM generation at high latitudes: Surface Extraction with TIN-based Search-space Minimization (SETSM) validation and demonstration over glaciated regions. *GIScience and Remote Sensing*, *52*(2), 198-217.

Noh, M.J. and Howat, I.M. (2017). The surface extraction from TIN based search-space minimization (SETSM) algorithm. *ISPRS Journal of Photogrammetry and Remote Sensing*, *129*, 55-76.

Nuth, C. and Kääb, A. (2011). Co-registration and bias corrections of satellite elevation data sets for quantifying glacier thickness change. *The Cryosphere*, *5*(1), 271-290.

Paine, D. P. and Kiser, J. D. (2012). *Aerial photography and image interpretation*. John Wiley and Sons.

Paul, F., Bolch, T., Kääb, A. Nagler, T., Nuth, C., Scharrer, K., Shepherd, A., Strozzi, T., Ticconi, F., Bhambri, R., and Berthier, E. (2015). The glaciers climate change initiative: Methods for creating glacier area, elevation change and velocity products. *Remote Sensing of Environment, 162*, 408-426.

Paul, F., Bolch, T., Briggs, K., Kääb, A., McMillan, M., McNabb, R., Nagler, T., Nuth, C., Rastner, P., Strozzi, T., and Wuite, J. (2017). Error sources and guidelines for quality assessment

of glacier area, elevation change, and velocity products derived from satellite data in the Glaciers_cci project. *Remote Sensing of Environment*, *203*, 256-275.

Reusch, D. and Hughes, T. (2003). Surface “waves” on Byrd Glacier, Antarctica. *Antarctic Science*, *15*(4), 547-555.

Rignot, E., and Jacobs, S. S. (2002). Rapid bottom melting widespread near Antarctic ice sheet grounding lines. *Science*, *296*(5575), 2020-2023.

Rignot, E., Mouginot, J., Scheuchl, B., van den Broeke, M., van Wessem, M.J., and Morlighem, M. (2019). Four decades of Antarctic Ice Sheet mass balance from 1979–2017. *Proceedings of the National Academy of Sciences*, *116*(4), 1095-1103.

Rupnik, E., Daakir, M. and Deseilligny, M.P. (2017). MicMac–a free, open-source solution for photogrammetry. *Open Geospatial Data, Software and Standards*, *2*(14).

Sanz-Ablanedo, E., Chandler, J., Rodríguez-Pérez, J., and Ordóñez, C. (2018). Accuracy of unmanned aerial vehicle (UAV) and SfM photogrammetry survey as a function of the number and location of ground control points used. *Remote Sensing*, *10*(1606).

Scambos, T.A., Dutkiewicz, M.J., Wilson, J.C., and Bindschadler, R.A. (1992). Application of image cross-correlation to the measurement of glacier velocity using satellite image data. *Remote Sensing of Environment*, *42*(3), 177-186.

Schenk, T., Csatho, B., van der Veen, C.J., Brecher, H., Ahn, Y., and Yoon, T. (2005). Registering imagery to ICESat data for measuring elevation changes on Byrd Glacier, Antarctica. *Geophysical Research Letters*, *32*(L23S05).

Schiefer, E. and Gilbert, R. (2007). Reconstructing morphometric change in a proglacial landscape using historical aerial photography and automated DEM generation. *Geomorphology*, *88*(1-2), 167-178.

Shepherd, A., Fricker, H.A., and Farrell, S.L. (2018). Trends and connections across the Antarctic cryosphere. *Nature*, *558*(7709), 223-232.

Stearns, L.A. (2007). Outlet glacier dynamics in east Greenland and East Antarctica. PhD, University of Maine.

Stearns, L.A., Smith, B.E., and Hamilton, G.S. (2008). Increased flow speed on a large East Antarctic outlet glacier caused by subglacial floods. *Nature Geoscience*, *1*(12), 827-832.

Tonkin, T. and Midgley, N. (2016). Ground-control networks for image based surface reconstruction: An investigation of optimum survey designs using UAV derived imagery and structure-from-motion photogrammetry. *Remote Sensing*, *8*(786).

Triggs, B., McLauchlan, P.F., Hartley, R.I., and Fitzgibbon, A.W. (1999). Bundle adjustment—a modern synthesis. *International workshop on vision algorithms*, 298-372.

Vaughan, D.G., Comiso, J.C., Allison, I., Carrasco, J., Kaser, G., Kwok, R., Mote, P., Murray, T., Paul, F., Ren, J., Rignot, E., Solomina, O., Steffen, K., and Zhang, T. (2013). Observations: Cryosphere. In: Climate Change 2013: The Physical Science Basis. Contribution of Working Group I to the Fifth Assessment Report of the Intergovernmental Panel on Climate Change. 317-382.

Chapter 2
60-year surface elevation changes of major Transantarctic outlet glaciers

2.1 Introduction

Understanding the relationship between ice sheet mass balance and climate is crucial for sea level projections. The amount of ice contained within the Antarctic Ice Sheet has the potential to increase sea levels by ~60 m (Fretwell et al., 2013), which makes quantifying ice sheet mass balance is non-trivial. Scientists rely on mass balance measurements because they are a good evaluation of the state of glaciers and ice sheets. Unfortunately, large uncertainties in mass balance estimates exist, due to glacial isostatic adjustment and sparse accumulation rate measurements, and are particularly impactful in East Antarctica where mass change is estimated at 5 ± 46 Gt/yr from 1992-2017 (Shepherd et al., 2018). Due to data limitations, the oldest Antarctic mass balance estimates are from the early 1990s (Shepherd et al., 2018; Shepherd et al., 2019); assessing earlier mass balances requires gaps in data to be filled in with climate models. The results from these studies vary due to the coarse grid resolutions (~27 km) that smooth out regional spatial variations of parameters like surface slope (van Wessem et al., 2018).

Aside from surface mass balance estimates, the stability of an ice sheet and/or glacier is often determined from the geodetic mass balance (estimates of surface elevation change). Surface elevation change studies have been conducted for the entire Antarctic Ice Sheet, but as with mass balance studies, glaciers located below 80°S are not included or have high errors, due to orbital path limits of satellites (McMillan et al., 2014; Schröder et al., 2019). This omission is particularly true for outlet glaciers flowing through the Transantarctic Mountains, where

altimetric satellites only began regularly collecting data after 2012. Furthermore, altimetric data can be faulty due to the steep terrain and heavily crevassed ice surfaces. To overcome these issues, we utilize historic aerial photographs and innovative processing techniques to produce the longest temporal range (~60 years) of surface elevation changes in Antarctica, of high resolution (250 m).

In this study, we extract data from a resource not widely used in Antarctica — trimetrogon aerial (TMA) imagery collected by the U.S. Navy over outlet glaciers spanning from 63°S to 90°S from 1946-2000. We manually collect ground control points (GCPs) from high-resolution optical satellite imagery at high degrees of nadir which allows for data capture through the spatial extent of this study. The processing is done with structure-from-motion (SfM) software, and the results are reconstructed glacier surfaces from ~60 years ago. By comparing the historic DEMs with present-day surface elevations, we are able to gain a better insight into the long-term behavior of outlet glaciers that had been largely unmonitored prior to 2012.

2.2 Study Site

Figure 2.1 highlights the location of the seven outlet glaciers flowing into the Ross Ice Shelf (RIS) focused on in this study: Darwin/Hatherton Glacier, Byrd Glacier, Nimrod Glacier, Beardmore Glacier, Shackleton Glacier, Amundsen Glacier, and Scott Glacier.

Glacier	Grounding Line Velocity ($m\ y^{-1}$)	Thickness (m)	Area (km^2)	Length (m)	Grounding Line Width (m)
Scott	220	963	1890	140	23
Amundsen	150	948	730	76	12
Shackleton	80	672	1110	114	12
Beardmore	390	893	5260	211	22
Nimrod	340	820	3250	145	24
Byrd	830	2190	6200	175	23
Darwin/Hatherton	90	620	1240	150	10

Table 2.1: Parameters of the seven outlet glaciers. Velocity (Rignot et al., 2011) and thickness (Fretwell et al., 2013) values are from the central flow line over each glacier's grounding line. Glacier area is based on the present-day DEM spatial coverage currently available and not necessarily based on full glacier area.

We focus on elevation changes occurring on the grounded portion of the glaciers. By excluding the floating, down-flow segment of the glacier, we interpret any fluctuations in elevation to be due to either surface accumulation/ablation or changes in velocity.

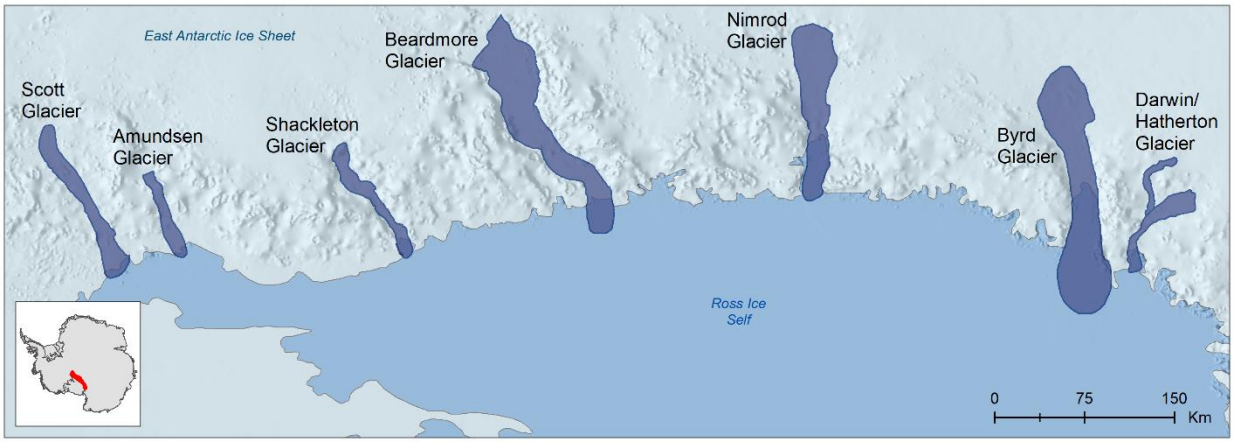

Figure 2.1: Map highlighting the East Antarctic outlet glaciers from this study with the inset map at the lower left showing the location in Antarctica. The glaciers are highlighted with violet polygons and ice is flowing from the top of the figure towards the direction of the Ross Ice Shelf. The background image is a 1 km hillshade of Slater et al. (2018)'s elevation dataset.

2.3 Data

2.3.1 Historic DEM: Trimetrogon Aerial Imagery

From 1946-2000, the United States Navy collected ~330,000 aerial photos in Antarctica (Figure 2.2), ~160,000 of which were trimetrogon aerial (TMA) images. TMA images consist of three photographs acquired simultaneously: at the same time that a vertical (or 0° nadir) image is being captured, so are two high oblique (> 30º nadir) images from each side of the airplane.

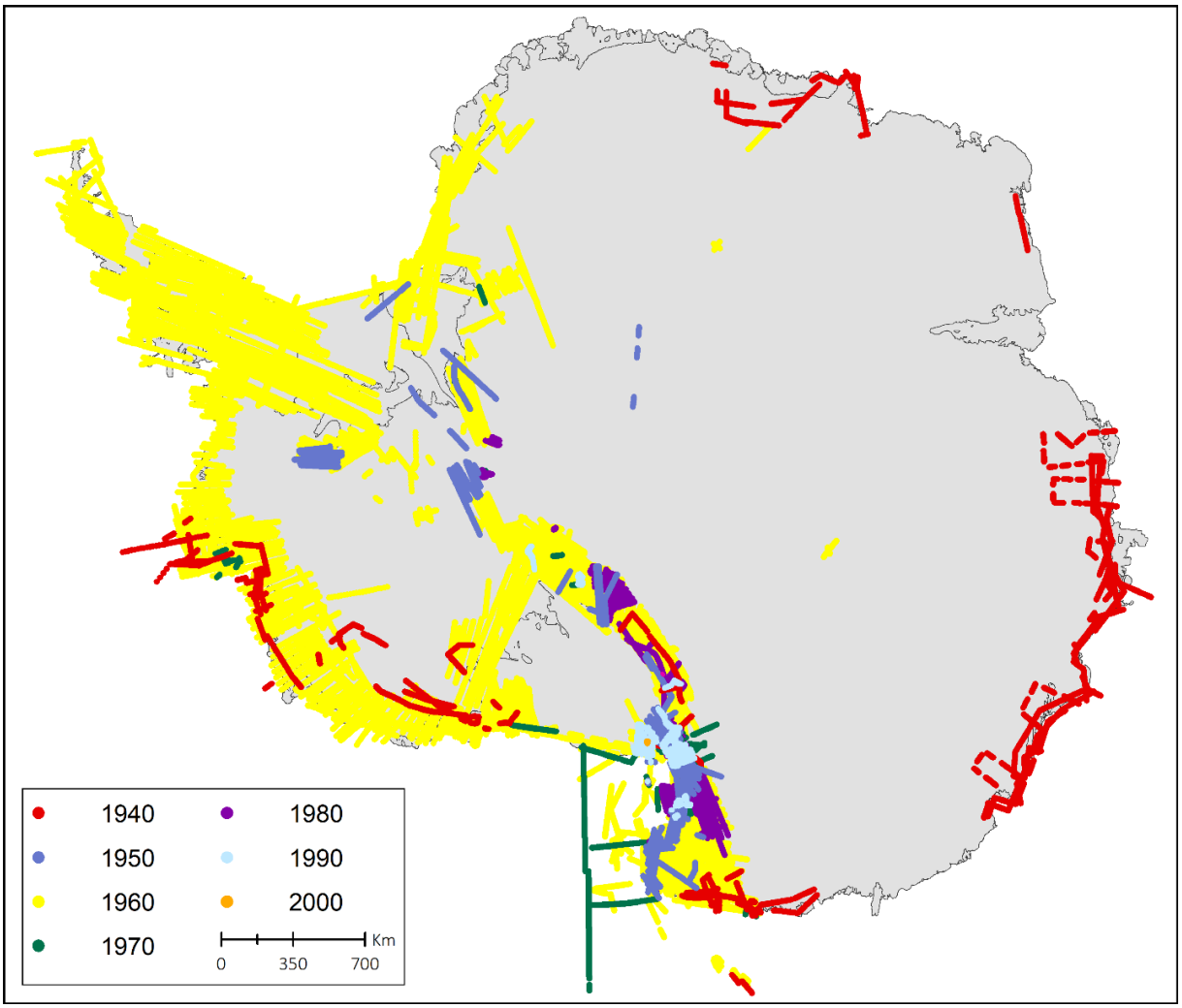

Figure 2.2: Map of Antarctic TMA image coverage collected by the U.S. Navy, by decade.

The camera types were all military-grade, manufactured by the Fairchild Camera and Instrument Company (van Reeth, 1966), and series T-11 or CA-14. Images were all captured on 9x9 inch panchromatic Kodak Aerographic Safety Film at an altitude of ~6,100-7,600 m. These photographs were originally collected to create the USGS's 1:250,000 topographic map series of the Transantarctic Mountains (Whitemore and Southard, 1966) during Operation Deep Freeze 60-65 (Anderson, 1974), but have been largely unused until presently.

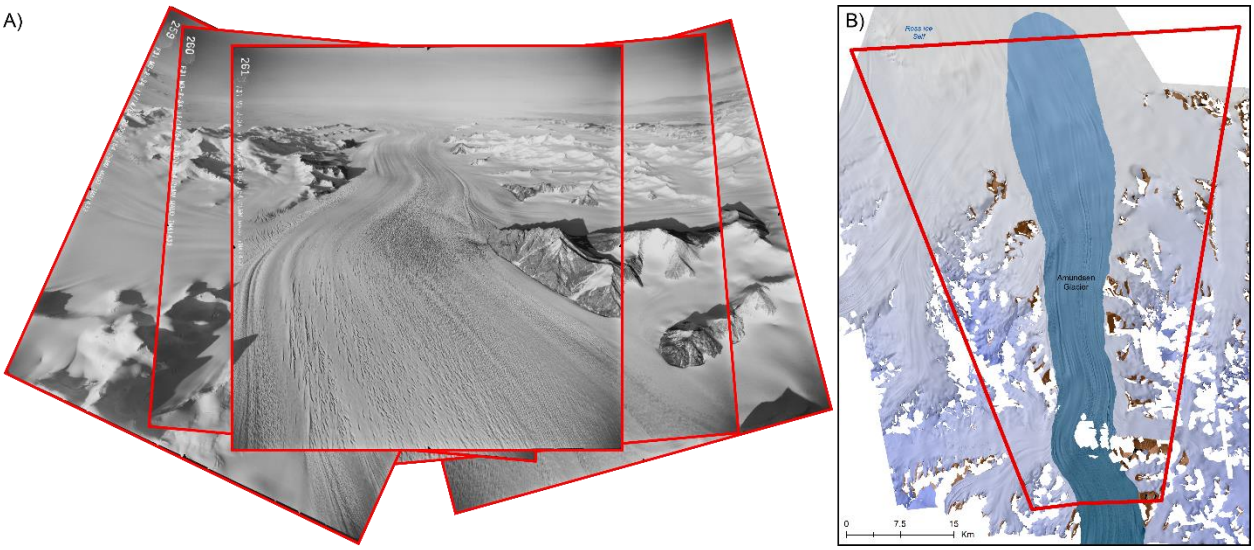

Figure 2.3: Example of oblique images: A) Left facing oblique image numbers 259-263 from flight TMA 1433. The glacier in the figure is Amundsen Glacier and view is looking down-flow towards the Ross Ice Shelf. Notice that the images do not align perfectly which is due to errors created by film distortion. B) A map of Amundsen Glacier — the red polygon outlines the extent of the photo coverage. The map has been rotated to match the same orientation as the aerial images.

For several decades, the location of the TMA image centers only existed as manual pencil drawings of the flight paths drawn on USGS 1:250,000 topographic maps. The resulting geolocations of the photo centers are very rough estimates; we use them only as a reference to identify specific images for processing, but otherwise assume the images contain no geospatial information.

The original TMA negatives are stored at the USGS's Earth Resources Observation and Science (EROS) Center, where they were also digitized at 1000 dpi. In this study, we use 65 oblique photographs collected over the years 1960-1964. This dataset is comprised of 17 different sets of images, where each glacier has image groups from 2-3 flight paths used in the DEM processing.

Glacier	TMA#	Images	Oblique Direction	Year	Focal Length (mm)	Tie Point #
Darwin/Hatherton						
	752	75-77	Left	1960	155.33	9,672
	1143	79-81	Left	1963	153.46	8,509
	1143	81-83	Right	1963	153.93	9,203
Byrd						
	768	115-117	Right	1960	155.33	13,261
	1002	86-90	Left	1962	154.42	26,639
Nimrod						
	763	2-4	Right	1960	155.33	14,395
	769	222-224	Right	1960	155.33	25,927
Beardmore						
	775	184-186	Right	1960	155.33	7,097
	780	5-7	Right	1960	153.23	12,231
Shackleton						
	780	57-61	Right	1960	153.23	43,094
	1133	100-102	Right	1963	153.46	24,470
	1447	9-13	Left	1964	154.25	20,411
Amundsen						
	780	124-126	Right	1960	153.23	15,060
	1433	259-263	Left	1964	154.25	18,415
Scott						
	780	141-145	Right	1960	153.23	38,729
	1447	109-113	Left	1964	154.26	22,772
	1447	116-120	Right	1946	154.46	24,315

Table 2.2: Image parameters for each group of TMA photographs.

2.3.2 Present-day DEM

Present-day elevation data are created from DEM strips of the Regional Elevation Model of Antarctica (REMA) (Howat et al., 2019) which are constructed from Noh and Howat (2015)'s

Surface Extraction from TIN based Search-space Minimization (SETSM) algorithm and distributed publicly by the Polar Geospatial Center (PGC). The SETSM algorithm creates DEMs from stereo-processing DigitalGlobe's WorldView versions 1-3 sub-meter imagery that was collected over the years 2012-2017. The final product is a DEM with a spatial resolution of 2 m; a by-product of the processing is the corresponding orthoimagery. The SETSM algorithm geolocates the DEMs using only the satellite sensor's rational polynomial coefficients (RPCs) (Noh and Howat, 2015). The available DEM strips are not co-registered to any other elevation product, and to date there is no formal metadata available for REMA data, so the horizontal and vertical errors are completely dependent on the accuracy of the RPCs. We conduct our own corrections and co-registration on these DEM strips and refer to the mosaic products as "present-day DEM" through the rest of the chapter.

2.3.3 Rock Mask

A rock mask is used to determine stable terrain locations (e.g. rock outcrop) in the historic DEMs and present-day DEMs as well as defining an ice/rock boundary for reporting results. The rock outcrop boundaries were delineated from Burton-Johnson et al. (2016). Burton-Johnson et al. (2016) calculated a normalized difference snow index (NDSI) from Landsat 8's Band 3 and Band 6 as far south over the continent of Antarctica as 82.6° South (the limit of Landsat's orbital coverage). For rock outcrops south of 82.6°, the boundaries are determined from exposed bedrock depicted from the USGS 1:250,000 topographic maps series covering the Transantarctic Mountains.

2.4 Methodology

2.4.1 Ground Control Points

Ground control is very sparse not just in the Transantarctic Mountains, but for all of Antarctica. Performing *in situ* ground control over ~140,000 km^2 of the Transantarctic Mountains is logistically difficult and extremely expensive. Our solution for ground control is to manually extract GCPs from the present-day DEMs. Other studies have used similar methodology in glaciological research — utilizing present-day elevations to obtain XYZ information for processing historic aerial imagery (Mertes et al., 2017; Midgley and Tonkin, 2017; Girod et al., 2018). We obtain ground control locations from stable, unchanging terrain of exposed bedrock not covered in ice or snow. Isostatic adjustment for the Transantarctic Mountains is estimated to be ~3 mm/yr (Argus et al., 2014; Peltier et al., 2015). Over the time frame of our study, uplift would have been ~0.143 m, which is well within acceptable vertical error of historic data (1 σ of stable terrain dh values (Frank et al., 2015)). Accordingly, we conclude that rock outcrop is still considered stable and a good candidate for ground control.

2.4.1.1 Shadow/Cloud/Blunder Masking

Prior to locating GCPs, we had to correct the present-day DEM data. The DEM strips created from Noh and Howat (2015)'s SETSM algorithm contain blunders due to shadows, clouds, and the high degree of nadir at which a significant portion of the WorldView 1-3 imagery was collected. In the case of shadows and high degree of nadir, the blunders lead to incorrect stereo-parallax calculations by the SETSM algorithm. Each DEM strip was manually inspected, and the bad-data values were masked from the dataset.

2.4.1.2 Co-registering/Mosaicking

Before mosaicking the DEM strips, we co-register each strip to its immediate up-stream neighboring strip. This is done to help correct for erroneous data values in the final mosaic DEM which may occur from factors like high slopes in terrain and atmospheric affects (Nuth and Kääb, 2011; Paul et al., 2017). Co-registering is performed using a python module called PyBob (McNabb, 2019) which uses the Nuth and Kääb (2011) method. DEM strips for each glacier are then mosaicked and resampled to 5 m. We use regions identified as stable terrain (after Burton-Johnson et al., 2016) to co-register the images.

2.4.1.3 Identifying GCPs

We locate potential GCP sites using WorldView 1-3 orthorectified imagery; the actual XYZ placement is established from local elevation highs in the present-day DEM (Figure 2.4). In SfM processing, only three GCPs are technically necessary for stereo-processing, but more GCPs ensures better bundle adjustment results (Girod et al., 2018). The bundle adjustment works to minimize reprojection errors by placing more emphasis on correctly placed GCPs and ignoring those that are offset. This function is highly advantageous because it is very challenging to accurately identify features in both satellite aerial (0° nadir) and aerial photo high-oblique (30°-60° nadir) views. A mountain peak in an oblique image captured ~60 km from the airplane will be comprised of a few pixels (~5-10), and the likelihood of placing a GCP on an incorrect pixel is large. An increase in the number of correctly placed GCPs increases the likelihood that the bundle adjustment corrects for XY misplacements.

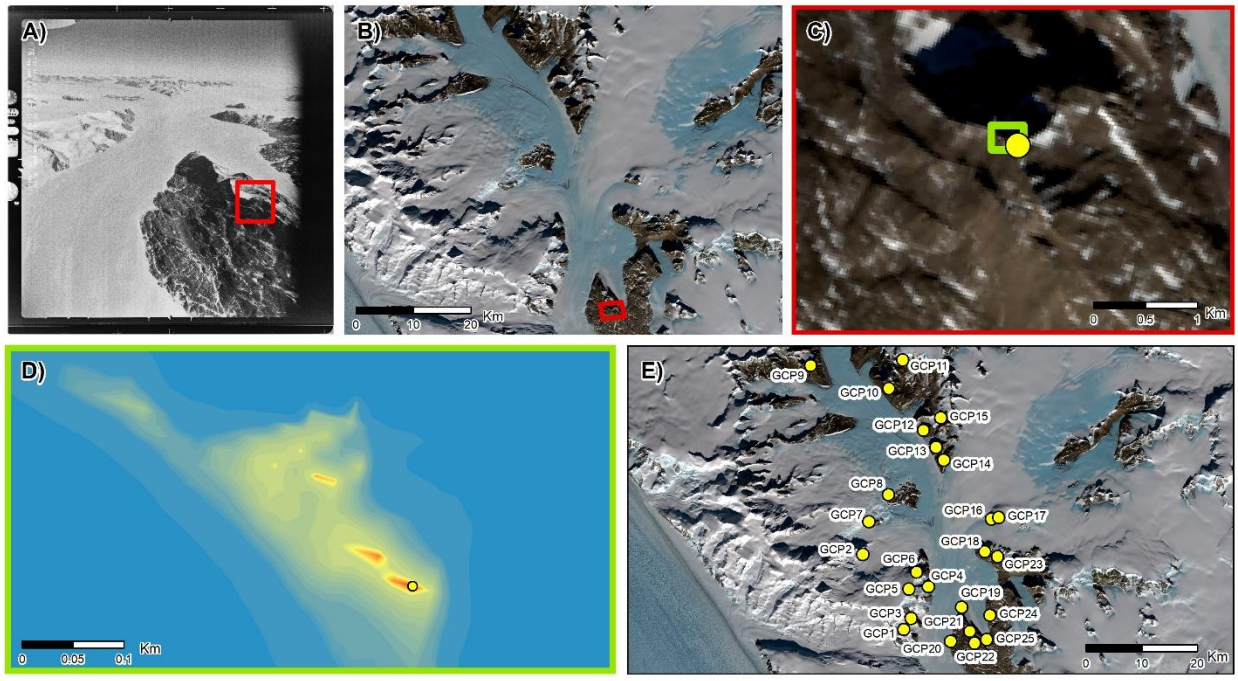

Figure 2.4: Image sequence illustrating the process of locating GCPs. The red box in (A) and (B) surrounds a topographic high in the oblique image and the Landsat 8 OLI images. Panel (C) is the zoomed in view of (A) and (B); the yellow point represents the elevation peak. The green box in (C) is further magnified in (D), which shows elevations from the present-day DEM. Topographic highs denoted by the darker orange color, and the GCP (yellow point) is placed at the peak. Panel (E) is a map of the GCPs used for Flight TMA 752 left oblique facing photos 75-77.

For each set of aerial images that we process, we locate and apply 22-30 GCPs — the difference in number is due to the availability of identifiable elevation peaks and number of images processed (for sets of five images, more GCPs were used). When choosing GCPs on oblique images, locations closer to the foreground are preferable because atmospheric effects like refraction are minimized (Bomford, 1980; Eiken and Sund, 2012).

2.4.2 Grounding Line

Our study focuses on elevation change over the grounded portion of glaciers. By ignoring the floating section, we isolate elevation changes due to either surface ablation/accumulation or velocity change. Therefore, corrections for tidal influence do not have to be applied nor does the

effect of submarine melting have to be considered. Grounded ice is defined as any ice up-flow of the hydrostatic equilibrium boundary.

We calculate the hydrostatic equilibrium using:

$$\Delta h' = \bar{h} - \frac{z(\rho_w - \rho_i)}{\rho_w}, \qquad (2.1)$$

where z is ice thickness (Fretwell et al., 2013) and $\bar{h}$ is surface elevation. In this equation, we use the present-day elevation, resampled to correspond to the ice thickness data.

2.4.3 TMA Processing

We process the historic imagery using a SfM program called MicMac. MicMac is an open-source SfM software created by the National Institute of Geographic and Forestry Information (IGN) and the National School of Geographic Sciences (ENSG) (Rapnik et al., 2017). The first step in SfM processing is manually locating the four fiducial marks, after which all of the images are normalized by resampling them to 25 microns. We then automatically identify tie points (or common features) in MicMac using the Scale-Invariant Feature Transformation (SIFT) algorithm (Lowe, 2004). Image features such as text and film border information are identified as tie points in this automated process, so we must first create a mask to exclude these data points from the final elevation processing. On average, ~20,000 of tie points are identified per set of images (Table 2.2).

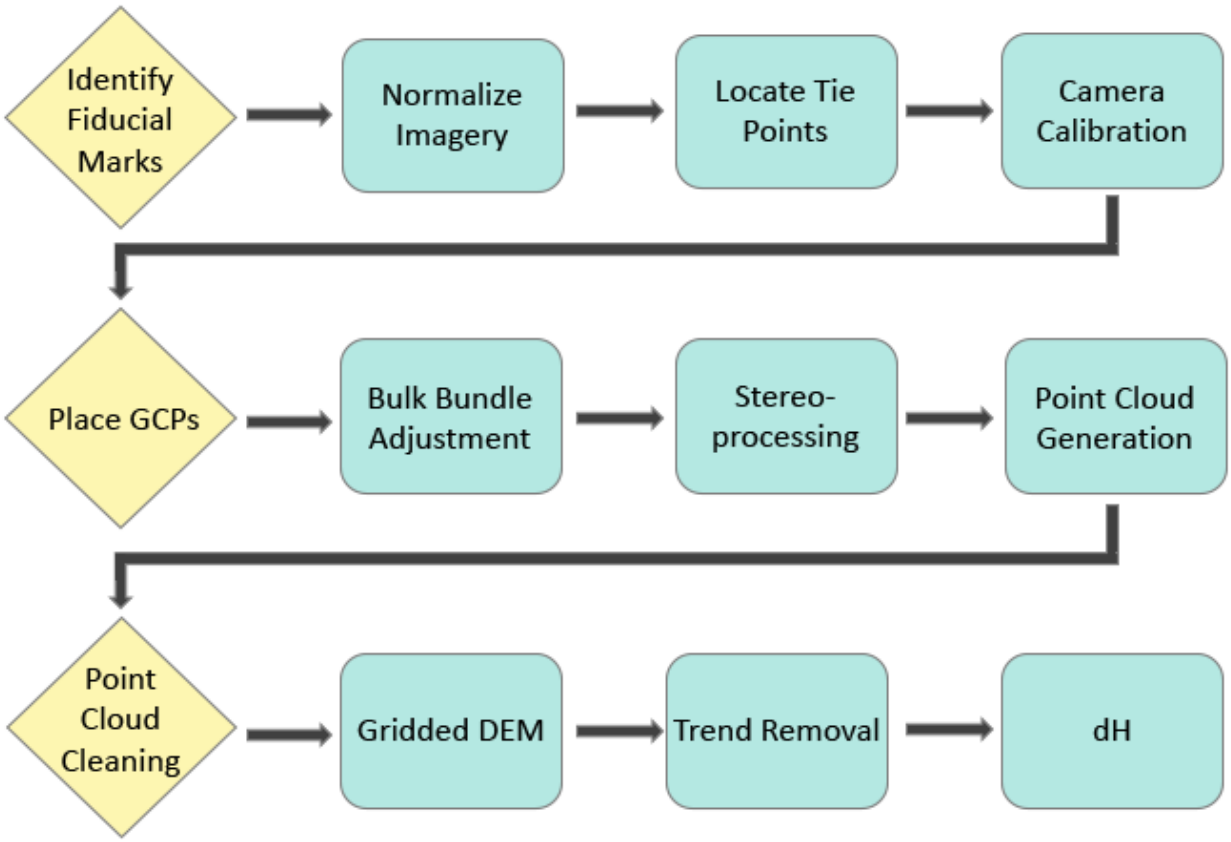

Figure 2.5: SfM processing tree. The yellow diamond shapes represent the processes that are manual and the teal rectangles are the automated ones.

Once tie points are located, an image coordinate system for the tie points (e.g. relative orientation) is determined using Fraser (1997)'s distortion model for camera calibration with the camera's focal length. Any image sets with calibration residuals greater than 1 pixel are eliminated. High residual values are the result of issues like poor image overlap (> 60%) and too few tie points identified (Dai and Lu, 2012; Dai et al., 2014). Absolute orientations are determined by manually identifying GCPs on the historic oblique images. Relative orientations are then transformed to real-world XYZ using a bundle adjustment.

We use MicMac's ground image geometry mode to complete the stereo-processing. This type of processing requires one master image and an equal number of secondary images surrounding it

(every master image is encompassed by either 2 or 4 secondary images (e.g., Figure 2.3 A)), which produces a DEM with the extent of master image coverage. Oblique aerial images are unique because they capture features like airplane wings and the atmospheric horizon (sky), which need to be masked out of the final DEM product. Likewise, homologous features, such as clouds and smooth snow surfaces, need to be filtered out because they produce errors in the SfM results. A new mask is created in the stereo-processing step to remove these features. The result of the SfM processing is a point cloud of the terrain from the master image. The point clouds are edited for spurious points ($dh > 3\ \sigma$) and registered to the present-day data in the software CloudCompare.

2.4.4 Elevation Differencing

At this step, we have the present-day DEM in a gridded format, and a historic DEM in a point cloud format. To estimate elevation differences, we convert the gridded present-day DEM to a point cloud. Recent research shows that large errors are introduced when a point cloud generated from oblique imagery is converted to a gridded format before elevation differences are calculated (Midgley and Tonkin, 2017). Vertical images do not have this problem because their generated point clouds are essentially a single layer of points resembling a rubber sheet draped over terrain. Oblique imagery, on the other hand, produce point clouds that resemble clusters instead of rubber sheets. A mountain for example will not just be made of a point cloud with an outer shell of points representing the terrain geometry, it will also have points within the “interior” of the mountain (see Figure 2.6).

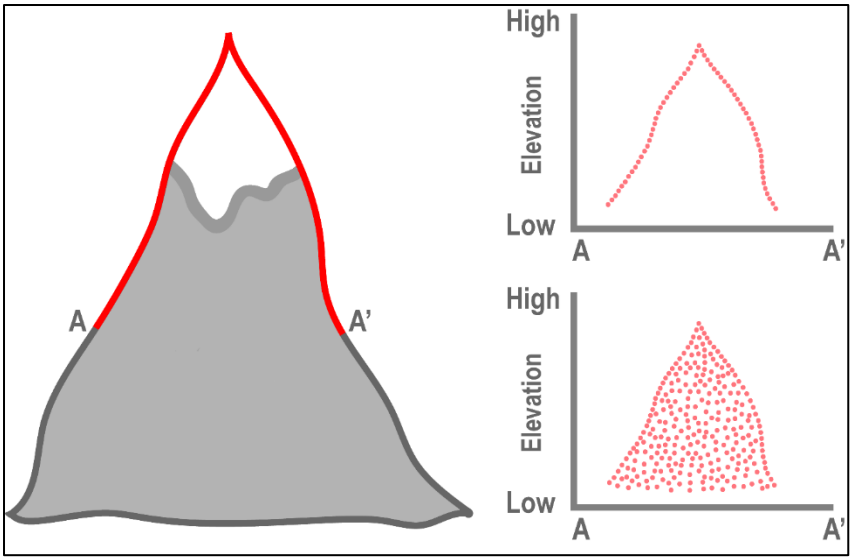

Figure 2.6: Schematic showing the profile of a point cloud created from vertical (B) and oblique (C) images from the profile A to A'. The profile in (B) depicts a singular row of points while the profile in (C) contains filler points.

We difference the two point clouds (derived from the present-day DEM and from TMA images) using the multiscale model to model cloud comparison (M3C2), which was developed as a plugin by Lague et al. (2013) for CloudCompare. The M3C2 plugin is a robust means of estimating the distance between two elevation data sets by using a sample set of core points from the historic point cloud. The plugin calculates a search distance from each core point to correlating values in the present-day point cloud from which elevation change is estimated. Due to the high variability of glacier surface texture of these glaciers, we chose a spatial perimeter of 250 m to eliminate any elevation differences that might arise from changes in crevasse patterns and flow lines. The differenced results were converted into 250 m grids.

Elevation differences of data products whose imagery was collected by different sensors contain a directional trend or "tilt" (Nuth and Kääb, 2011), which has also been observed in dh studies using historic oblique satellite imagery (e.g. CORONA data) (Bolch et al., 2008; Pieczonka et

al., 2011). Regardless of the surface (glaciated and/or exposed bedrock) the uncorrected dh results have a monotonic trend that, in most cases, increases with elevation change and distance from the plane. The tilt in the dh results was corrected by removing a fitted 2nd order polynomial trend surface from the dh results (Racoviteanu et al., 2007; Bolch et al., 2008).

2.5 Results

2.5.1 Grounding Lines

We calculate grounding line locations for all seven glaciers, using the present-day elevations and hydrostatic equilibrium (see Figure 2.7). We compare our results with published studies and find good overlap in position for Darwin Glacier (Gillespie et al., 2017), Byrd Glacier (Floricioiu et al., 2012), Nimrod Glacier (Floricioiu et al., 2012), and Beardmore Glacier (Marsh et al., 2013). Our derived grounding lines are substantially different for Nimrod, Amundson, and Scott glaciers than those calculated by Bindschadler et al. (2011). Due to the extremely crevassed surface of Nimrod Glacier and the methodology used to identify the grounding line from Bindschadler et al. (2011) (e.g. photoclinometry which is known for having trouble producing accurate results on highly crevassed regions) and the significantly higher spatial resolution of the data we used for our analysis, we feel confident that our results provide a more accurate grounding line location.

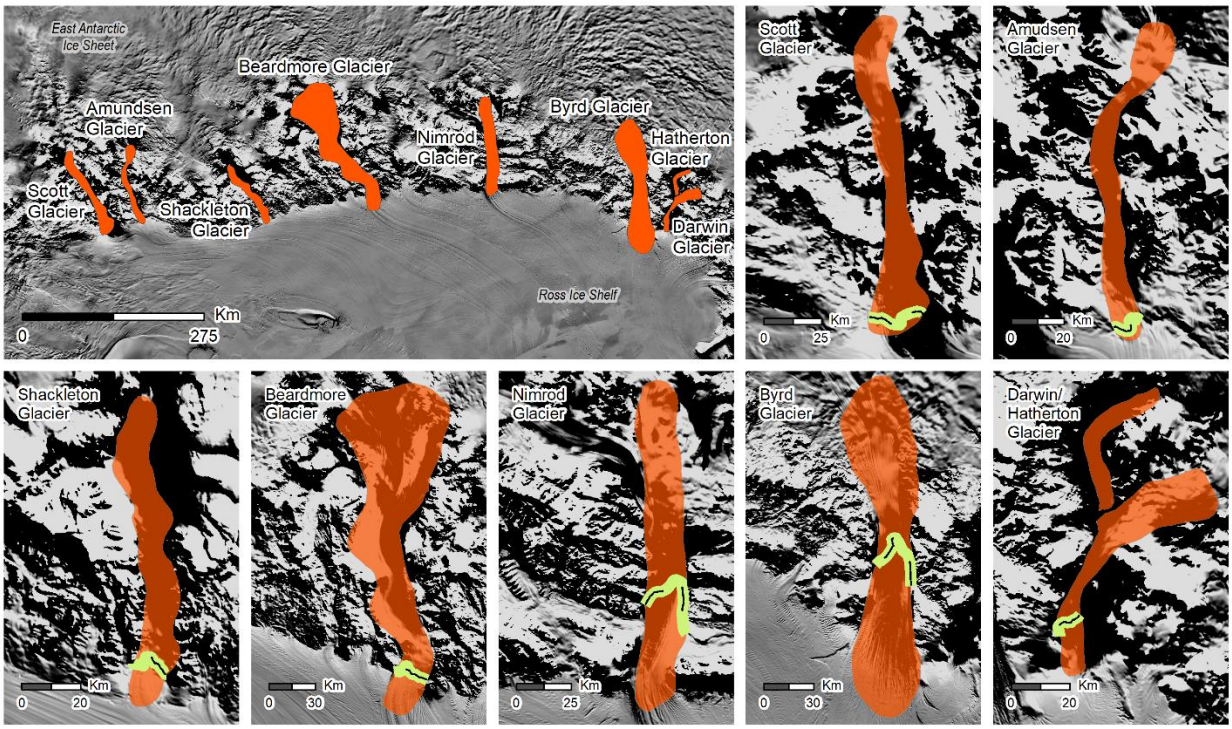

Figure 2.7: Grounding lines calculated from hydrostatic equilibrium represented by the lime green lines over the glacier polygons in orange. Background images is from Radarsat.

2.5.2 Elevations

2.5.2.1 SfM Processing

Historical (54-57 years ago) glacier surfaces were rendered for the seven glaciers, covering ~3900 km^2 (Figure 2.8). Nimrod Glacier has the least coverage because the majority of the processed results were eliminated due to being located down-flow of the grounding line. Glaciers with varied surface textures, such as Amundsen, Darwin, Scott, and Shackleton, had the greatest density of processed points. Beardmore Glacier has a very smooth surface, which is why it had the fewest number of tie points and one of the smallest DEM coverages.

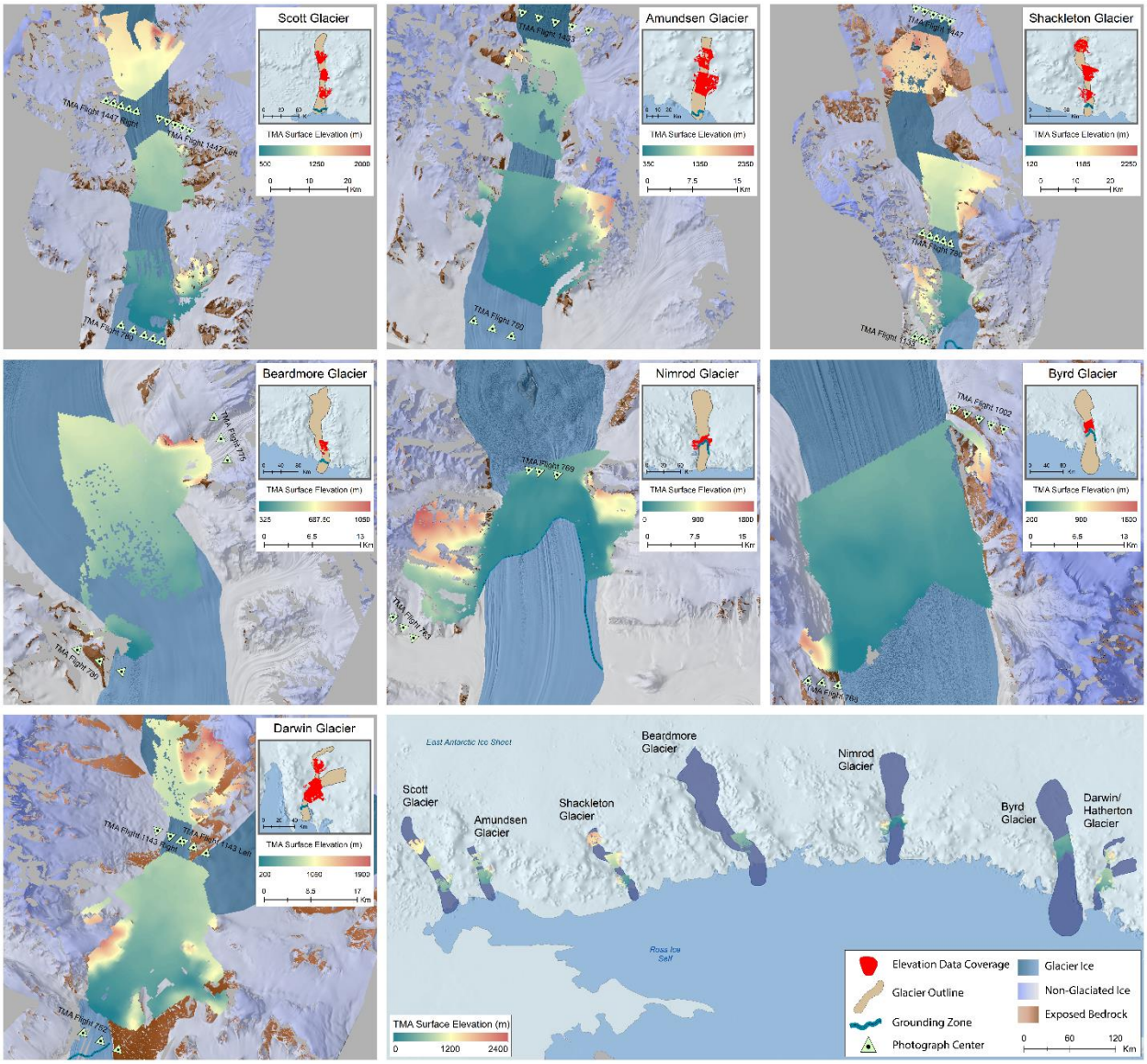

Figure 2.8: SfM processed historic DEMs for each glacier and in (H) a map of all 7 DEMs. The symbols in the legend of (H) apply to the rest of the maps in the figure. The smaller maps in the upper right corners of (A)-(G) are showcasing the spatial coverage of the DEMs. The elevation color and scale bars are specific to each map.

2.5.2.2 Accuracy

The resulting elevations are only relative because *in situ* ground control does not exist in the Transantarctic Mountains with sufficient coverage and accuracy to permit translation of SfM DEMs to absolute values. We assess the accuracy of the elevation result by examining the standard deviation and root mean square error (RMSE) of the differences of present-day

elevation to historic elevations over exposed bedrock, whose terrain is sloped less than 20°. In Figure 2.9A, a scatter plot of all of the stable terrain (3,537 elevation values) has a vertical mean difference of -3.311 m, standard deviation of 24.746 m, and a RMSE of 24.711 m. By excluding values of dh outside of 3 σ, the RMSE improves to 18.372 m. This value is well within range of RMSE values reported for historic DEM validations on the Antarctic Peninsula (Fieber et al., 2018).

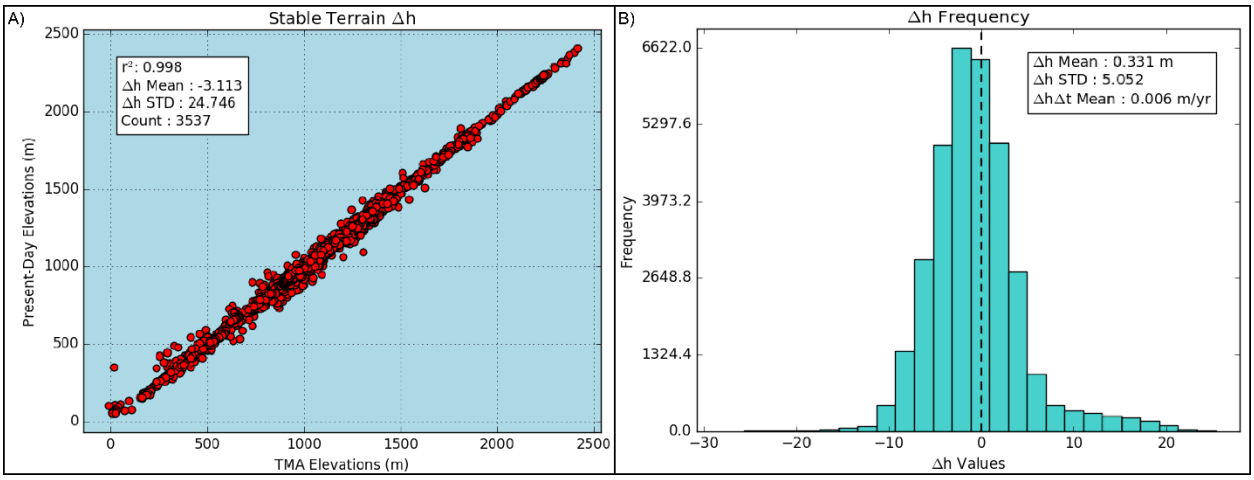

Figure 2.9: Stable terrain differences: A) Scatter plot of the present-day and historic elevations over all stable terrain. B) Frequency histogram of the dh results for all seven glaciers.

We assess the SfM processing algorithm by analyzing residuals estimated during the block bundle adjustment. In Table 2.3, the average residual from the block bundle adjustment is an error less than ~0.99 of a pixel. The mean shifts for the XYZ positions are larger than that for typical digital photography, but these large shifts are expected due to poor quality of images, digitization, and possible film distortions which were not accounted for (Csatho et al., 2008).

2.5.3 Surface Elevation Change

The overall mean change in elevation is a slight gain of 0.331 m which is a rate of ~0.006 m/yr. Two of the seven glaciers have undergone thinning while the other five have become thicker over the past 60 years. Figure 2.10 shows the dh results for all seven glaciers and Table 2.4 lists the individual dh means. Nimrod Glacier underwent the greatest change with an elevation gain of 6.68 m; Amundsen Glacier underwent the most thinning at 3.10 m. By comparing these results with other Antarctic outlet glaciers like Pine Island Glacier, whose surface has lowered by 2.72 ±.07 m over the past 25 years (Shepherd et al., 2019), we interpret our results as the major Transantarctic Mountains outlet glaciers are in stable condition.

Glacier	TMA ID	X-shift (m)	Y-shift (m)	Z-shift (m)	Average Residual	Pixel Error
Darwin						
	752L #75-77	0.94	3.55	0.20	0.82	1.65
	1143L #79-81	16.9	3.08	-1.38	0.94	1.74
	1143R #81-83	7.12	-0.84	0.27	0.82	3.38
Byrd						
	768R #115-117	1.76	-3.45	-0.97	1.23	1.76
	1002L #86-90	-0.93	-0.13	2.53	1.09	2.74
Nimrod						
	763R #2-4	0.04	-3.84	-0.75	1.01	1.21
	769R #222-224	3.67	-20.2	-.004	1.02	1.63
Beardmore						
	775R #184-186	38.6	31.1	4.89	0.75	3.55
	780R #5-7	-3.64	-16.3	0.16	1.06	1.74
Shackleton						
	780R #57-61	-6.65	-38.4	5.09	1.04	1.66
	1133R #100-102	-4.77	1.10	0.16	0.97	1.13
	1447L #9-13	10.4	-66.5	-3.93	0.98	3.87
Amundsen						
	780R #124-126	-2.40	-1.87	1.96	0.95	1.64
	1433L #259-261	13.0	11.7	4.33	1.11	5.06
Scott						
	780R #141-145	27.0	44.3	7.26	1.25	7.69
	1447L #109-113	-59.0	-35.7	-8.98	0.92	4.28
	1447R #116-120	3.10	-31.4	-0.36	1.00	2.98
Mean Values		**2.77**	**-6.38**	**0.65**	**1.00**	**2.74**

Table 2.3: The displacement variables calculated during the block bundle adjustment. The Average Residual and Pixel Error are both in units of pixels.

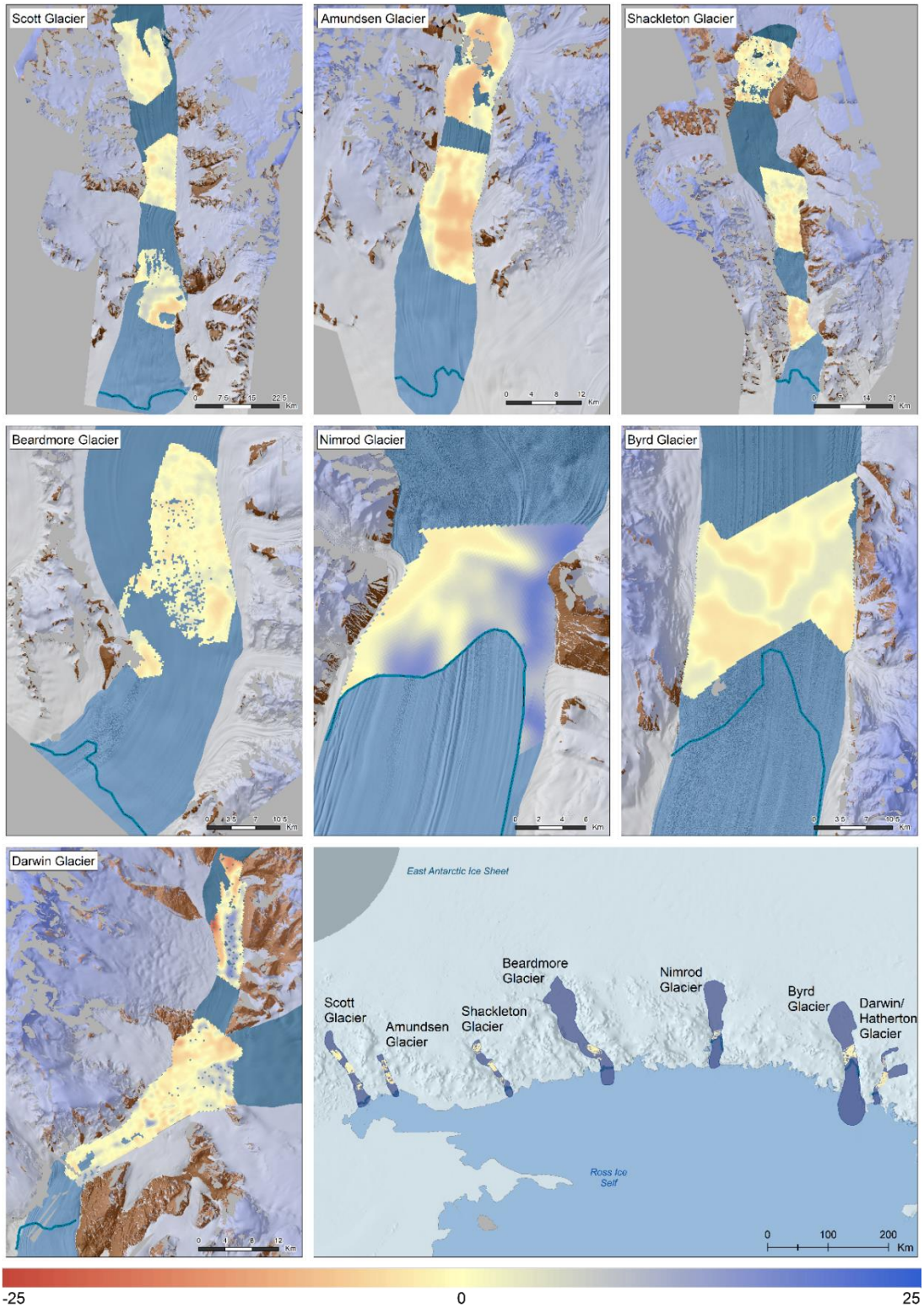

Figure 2.10: Elevation change maps for all seven glaciers (A-G) and an overview map from the Transantarctic Mountains in meters. The color bar scale is for -25m to +25m. The background images are hill shades of the present-day elevations.

Glacier	Min dh (m)	Max dh (m)	Mean dh (m)	dh/dt (m/yr)
Scott	-6.51	7.61	0.51	0.0089
Amundsen	-9.57	5.71	-3.10	-0.0544
Shackleton	-8.62	6.20	-0.68	-0.0119
Beardmore	-7.29	7.73	0.04	0.0006
Nimrod	-2.00	19.00	6.68	0.1172
Byrd	-5.30	5.24	0.01	0.0001
Darwin/Hatherton	-24.59	26.38	0.56	0.0098

Table 2.4: Elevation change results for all seven glaciers for the past 54-57 years. Dh values fall within 3 σ of the mean.

2.6 Discussion

2.6.1 Ice sheet surface elevation changes

Some East Antarctic regions like Wilkes Land have been losing mass since the 1980s (Rignot et al., 2019), but mass balance and surface elevation change results of the EAIS are generally positive (Shepherd et al., 2018; McMillan et al., 2014; Zwally et al., 2015). However, due to sparse data and various data types used to estimate mass balance, there is disagreement over how much ice mass East Antarctica has contributed to sea level over the past 20 years (Hanna et al., 2013). Typical mass balance and surface elevation change studies are Antarctic-wide and do not report results for individual glaciers (Zwally et. al, 2015, Shepherd et. al, 2019, Schroder et. al, 2019). These studies instead report change either on a East-West-Peninsula scale, or by specified basins. Only a few studies report elevation change (Shepherd et al. (2019) and McMillan et al. (2014)), and they estimate an average surface elevation increase of 0.003 m/yr for the basin highlighted in Figure 2.11A from datasets covering 1992-2015 and 2010-2013 respectively. This positive trend in elevation is similar to our results (0.006 m/yr) of average elevation change.

Dynamic changes at the grounding line of marine terminating glaciers have the potential to lead to large-scale mass loss and possibly complete ice sheet collapse (Hughes, 1973; Schoof, 2007). Glaciers that are particularly vulnerable to this phenomenon are those with deep troughs, retrograde slopes, and grounded ice significantly below sea level (Schoof, 2007). Given these traits, dynamic thinning at the grounding line has the potential to propagate several kilometers inland of the grounding line to the catchment basin (Dupont and Alley, 2005; Pritchard et al., 2009). To some extent, Scott, Amundsen, Beardmore, Nimrod, and Byrd Glaciers exhibit these characteristics at their grounding lines and are therefore capable of contributing substantial mass loss given retreat of their grounding lines. Data for Nimrod Glacier extend down-flow of the grounding line (data for the other glaciers do not), so we can calculate changes in grounding line elevation. We do not observe any elevation lowering at Nimrod Glacier's grounding line change and, in fact, detect slight mass gain for most of the other glaciers with reverse bed slopes just up-flow from their grounding lines. We interpret this as more evidence in favor of Transantarctic Glacier stability.

All glaciers in our study exhibit localized regions of both positive and negative elevation change at their margins and along their trunks. These localized elevation changes could be due to changes in ice dynamics from merging tributary glaciers (Thomas et al., 2009), variations in subglacial hydrology (Scambos et al., 2011; Babonis et al., 2016), surface ablation due to sublimation (e.g. exposed blue ice (Bintanja,1999; Kassab et al., 2019)), or increased surface melt (Kingslake et al., 2017; Bell et al., 2018). The exact causes of elevation change are beyond the scope of this study; however, they are important for understanding ice dynamic processes and deserve more attention in future studies.

2.6.2 Impact from Ross Ice Shelf

The majority of mass loss in Antarctica occurs at the ice shelves from basal melt, which has increased over the last couple of decades due to warming ocean temperatures (Rignot et al., 2013; Schodlok et al., 2016). The effect of warming ocean temperatures from Circumpolar Deep Water (CDW) varies around Antarctica; while some ice shelves are undergoing excessive sub-ice shelf melt, other ice shelves are at or near steady state (Moholdt et al., 2014). Paolo et al. (2015) estimated a rate of elevation change of -0.32 m/yr along the RIS for a period of 1994-2012; but other estimates show slight basal accretion of 0.1 m/yr (Liu et al.,2015), for a period from 2003-2011, which will either result in surface elevation rise or steady-state depending on grounding line discharge and calving rates. Despite having opposite signs, these results both show moderate rates of change, indicating that RIS is largely in balance (Moholdt et al., 2014). At glacier grounding lines, changes in ice shelf thickness can have a large impact on ice-flow upstream (Scambos et al., 2004; Pritchard et al., 2012). Estimates of RIS stability suggests that any observed elevation change on grounded ice is due to local ice dynamics.

Tinto et al. (2019) compiled a new high-resolution bathymetric map of the RIS, which highlights a newly discovered tectonic boundary believed to create an insulating effect for glaciers draining into the RIS from warming ocean temperatures. This effective shield may be protecting RIS grounding lines from following the fate of other glaciers in Antarctica (e.g. enhanced submarine melt, followed by grounding line retreat and glacier acceleration (Pritchard et al., 2012)). The implication is that RIS grounding lines are more likely impacted by local influences (e.g. ice dynamics) than from CDW; therefore, it is possible that these grounding lines will remain stable

even in warming conditions (Fürst et al., 2016; Tinto et al., 2019). This hypothesis agrees well with our observed trends in elevation change. Despite a warming climate and its influence on the oceans and other Antarctic outlet glaciers, these major outlet glaciers in the Transantarctic region have remained relatively stable.

2.6.3 Hydrostatic equilibrium boundary changes

Konrad et al. (2018) find that only 3.3% of East Antarctic grounding lines retreated between 2010-2016. Glaciers flowing into Eastern RIS exhibited average grounding line advances of ~4 m/yr. We focus on Nimrod Glacier because as previously mentioned, it is the only glacier with elevation results that spatially overlap its grounding line; its grounding line is estimated to have advanced by 3.6 m/yr over the six-year time-line (Konrad et al., 2018). We are uncertain of the exact grounding line location from the 1960s, but since the same parameters that influence grounding line migration (e.g. basal melt, thickness change) also affect the hydrostatic equilibrium boundary, we solve for the equilibrium from the historical and present-day DEMs to assess 57 year-old migration. We find from the historic results that the boundary has drifted as much as ~1.3 km in both directions at specific locales (Figure 2.11B). Applying Konrad et al.'s (2018) grounding line migration rate to hydrostatic equilibrium boundary migration, the 3.6 m/yr of down-flow drift only produces a total migration of ~200 m for a 57-year period which is significantly less than our estimation of ~±1.3 km. This difference in total boundary deviations of Nimrod Glacier from 2010-2016 versus the 57-year period is hypothetically a signal that the hydrostatic equilibrium is experiencing a slow-down in migration rates. The 57-year boundaries changes are not uniform with the width of the glacier, which implies that even though the surface elevation of Nimrod Glacier has increased, other glacial dynamics will have had to alter in order

for the boundary to have drifted as such. More information about Nimrod's grounding line location and surrounding tributary glaciers' dynamics is necessary to better understand the causes of past and present-day migration rate fluctuations.

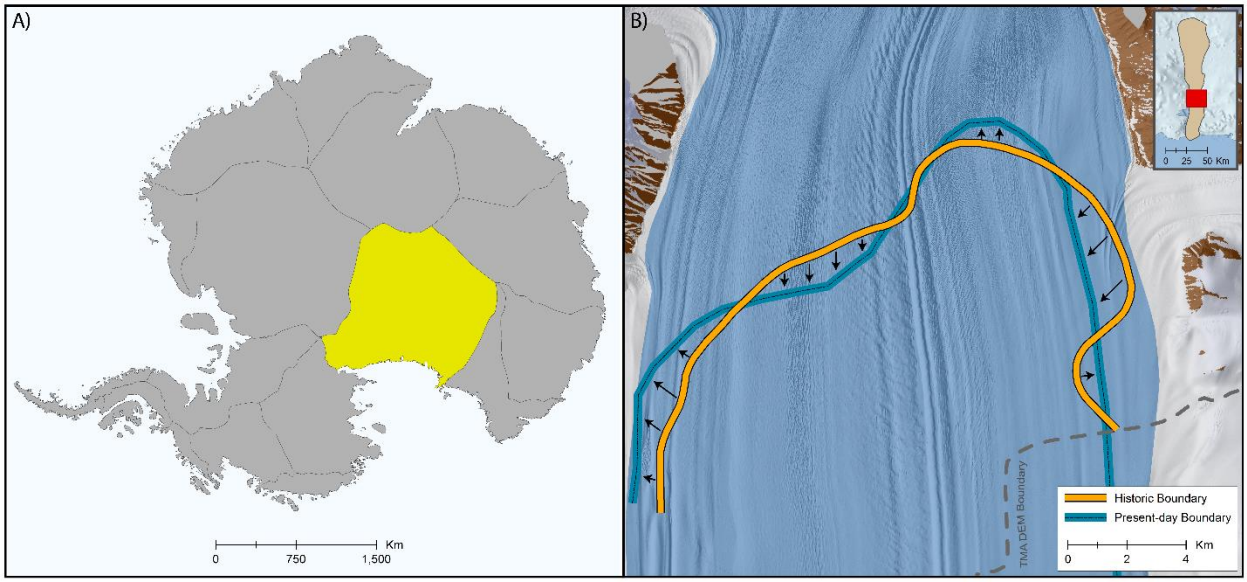

Figure 2.11: Basin and hydrostatic equilibrium boundaries: The basin boundaries in A) are the ones delineated from Giovinetto and Zwalley (2000), Rignot et al. (2011), and Rignot et al. (2013) for the 2016 Ice Sheet Mass Balance Inter-comparison Exercise (IMBIE) ice sheet basin dataset. The region highlighted in dark yellow is the catchment basin for the Transantarctic glaciers. B) The historic and present-day hydrostatic equilibrium boundaries on Nimrod Glaciers with arrows pointing in the direction of boundary movement. Ice is flowing from the top to the bottom of the figure. The map inset in the top right corner shows the data coverage. The gray dashed line denotes the spatial extent of the TMA DEM.

2.7 Conclusion

Using the historic TMA imagery with SfM processing, we have created the oldest elevation dataset to date of the Transantarctic Mountains. We find for seven major outlet glaciers flowing through this region over a 54-57 year period that the average elevation change is a gain of ~0.3 m. On average, these glaciers have gained 0.006 m/yr for the last six decades. This change in elevation is minor and suggests that these outlet glaciers are in steady state. In total, the

estimated range of mean elevation differences are roughly -3 m (Nimrod Glacier) to +7 m (Amundsen Glacier); Byrd Glacier changed the least.

All of the glaciers we studied underwent localized patterns of both elevation gain and loss. The fact that spatial patterns of elevation change are not uniform shows that these glaciers have a more complex history than past mass balance studies have indicated. More research into parameters like surface velocities and surrounding tributary glacier hypsometries estimated from various epochs is necessary to better understand the exact causes of elevation change. Spatial expansion of the study sites is planned to better cover the entirety of these glaciers both further upstream into the ice sheet as well are the floating portions at and downstream of the grounding line.

Chapter 2 Citations

Anderson, P. J. (1974). United States aircraft losses in Antarctica. *Antarctic Journal of the United States, 9*(1), 1-21.

Anisimov, O.A., Vaughan, D.G., Callaghan, T.V., Furgal, C., Marchant, H. Prowse, T.D., Vilhjálmsson, H., and Walsh, J.E. (2007). Polar regions (Arctic and Antarctic). *Climate Change 2007: Impacts, Adaptation and Vulnerability. Contribution of Working Group II to the Fourth Assessment Report of the Intergovernmental Panel on Climate Change*, Parry, M.L., Canziani, O.F., Palutikof, J.P., van der Linden, P.J., and Hanson, C.E., Eds., Cambridge University Press, Cambridge, 653-685.

Argus, D.F., Peltier, W.R., Drummond, R., and Moore, A.W. (2014). The Antarctica component of postglacial rebound model ICE-6G_C (VM5a) based on GPS positioning, exposure age dating of ice thicknesses, and relative sea level histories. *Geophysical Journal International, 198*(1), 537-563.

Babonis, G.S., Csatho, B., and Schenk, T. (2016). Mass Balance Changes and Ice Dynamics of Greenland and Antarctic Ice Sheets from Laser Altimetry. *International Archives of the Photogrammetry, Remote Sensing and Spatial Information Sciences: XXIII ISPRS Congress, XLI-B8.* 481-487.

Bell, R.E., Banwell, A.F., Trusel, L.D., and Kingslake, J. (2018). Antarctic surface hydrology and impacts on ice-sheet mass balance. *Nature Climate Change, (8),* 1044-1052.

Bintanja, R. (1999). On the glaciological, meteorological, and climatological significance of Antarctic blue ice areas. *Reviews of Geophysics, 37*(3), 337-359.

Bindschadler, R., Choi, H., Wichlacz, A., Bingham, B., Bohlander, J., Brunt, K., Corr, H., Drews, R., Fricker, H., Hall, M., and Hindmarsh, R. (2011). Getting around Antarctica: new high-resolution mappings of the grounded and freely-floating boundaries of the Antarctic ice sheet created for the International Polar Year. *The Cryosphere(5),* 569-588.

Bjørk, A.A., Kjær, K.H., Korsgaard, N.J., Khan, S.A., Kjeldsen, K.K., Andresen, C.S., Box, J.E., Larsen, N.K., and Funder, S. (2012). An aerial view of 80 years of climate-related glacier fluctuations in southeast Greenland. *Nature Geoscience, 5*(6), 427-432.

Bolch, T., Buchroithner, M., Pieczonka, T., and Kunert, A. (2008). Planimetric and volumetric glacier changes in the Khumbu Himal, Nepal, since 1962 using Corona, Landsat TM and ASTER data. *Journal of Glaciology, 54*(187), 592-600.

Bomford, G. (1980). *Geodesy* (4th Edition). New York, NY: Oxford University Press

Brecher, H.H. (1982). Photographic determination of surface velocities and elevations on Byrd Glacier. *Antarctic Journal of the United States*, *17*(5), 79-81.

Burton-Johnson, A., Black, M., Fretwell, P., and Kaluza-Gilbert, J. (2016). An automated methodology for differentiating rock from snow, clouds and sea in Antarctica from Landsat 8 imagery: a new rock outcrop map and area estimation for the entire Antarctic continent. *The Cryosphere, 10*, 1665-1677.

Carter, S. P., Fricker, H. A., and Siegfried, M. R. (2017). Antarctic subglacial lakes drain through sediment-floored canals: theory and model testing on real and idealized domains. *The Cryosphere, 11* (1). 381-405.

Cook, A.J., Fox, A.J., Vaughan, D.G., and Ferrigno, J.G. (2005). Retreating glacier fronts on the Antarctic Peninsula over the past half-century. *Science, 308*(5721), 541-544.

Csatho, B., Schenk, T., Van Der Veen, C.J., and Krabill, W.B. (2008). Intermittent thinning of Jakobshavn Isbrae, West Greenland, since the little ice age. *Journal of Glaciology, 54*(184), 131-144.

Dai, F. and Lu, M. (2012). Three-dimensional modeling of site elements by analytically processing image data contained in site photos. *Journal of Construction Engineering and Management, 139*(7), 881-894.

Dai, F., Feng, Y., and Hough, R. (2014). Photogrammetric error sources and impacts on modeling and surveying in construction engineering applications. *Visualization in Engineering, 2*(1).

Dupont, T.K. and Alley, R.B. (2005). Assessment of the importance of ice-shelf buttressing to ice-sheet flow. *Geophysical Research Letters, 32*(4).

Eiken, T. and Sund, M. (2012). Photogrammetric methods applied to Svalbard glaciers: accuracies and challenges. *Polar Research, 31*(1).

Felikson, D., Bartholomaus, T.C., Catania, G.A., Korsgaard, N.J., Kjær, K.H., Morlighem, M., Noël, B., Van Den Broeke, M., Stearns, L.A., Shroyer, E.L., and Sutherland, D.A. (2017). Inland thinning on the Greenland ice sheet controlled by outlet glacier geometry. *Nature Geoscience, 10*(5), 366-369.

Floricioiu, D., Jezek, K., Baessler, M., and Jaber, W.A. (2012). Geophysical parameters estimation with TerraSAR-X of outlet glaciers in the Transantarctic Mountains. *2012 IEEE International Geoscience and Remote Sensing Symposium*, 1565-1568.

Fox, A.J. and Cziferszky, A. (2008). Unlocking the time capsule of historic aerial photography to measure changes in Antarctic Peninsula glaciers. *The Photogrammetric Record, 23*(121), 51-68.

Fraser, C.S. (1997). Digital camera self-calibration. *ISPRS Journal of Photogrammetry and Remote Sensing, 52*(4), 149-159.

Fretwell, P., Pritchard, H.D., Vaughan, D.G., Bamber, J.L., Barrand, N.E., Bell, R., Bianchi, C., Bingham, R.G., Blankenship, D.D., Casassa, G., and Catania, G.A. (2013). Bedmap2: improved ice bed, surface and thickness datasets for Antarctica.

Fürst, J.J., Durand, G., Gillet-Chaulet, F., Tavard, L., Rankl, M., Braun, M., and Gagliardini, O. (2016). The safety band of Antarctic ice shelves. *Nature Climate Change*, *6*(5), 479-482.

Gillespie, M.K., Lawson, W., Rack, W., Anderson, B., Blankenship, D.D., Young, D.A., and Holt, J.W. (2017). Geometry and ice dynamics of the Darwin–Hatherton glacial system, Transantarctic Mountains. *Journal of Glaciology*, *63*(242), 959-972.

Glovinetto, M.B. and Zwally, H.J. (2000). Spatial distribution of net surface accumulation on the Antarctic ice sheet. *Annals of Glaciology*, *31*, 171-178.

Girod, L., Nielsen, N.I., Couderette, F., Nuth, C., and Kääb, A. (2018). Precise DEM extraction from Svalbard using 1936 high oblique imagery. *Geoscientific Instrumentation, Methods and Data Systems*, *7*(4), 277-288.

Guzzetti, F., Mondini, A.C., Cardinali, M., Fiorucci, F., Santangelo, M., and Chang, K.T. (2012). Landslide inventory maps: New tools for an old problem. *Earth-Science Reviews*, *112*(1-2), 42-66.

Hanna, E., Navarro, F.J., Pattyn, F., Domingues, C.M., Fettweis, X., Ivins, E.R., Nicholls, R.J., Ritz, C., Smith, B., Tulaczyk, S., and Whitehouse, P.L. (2013). Ice-sheet mass balance and climate change. *Nature*, *498*(7452), 51-59.

Howat, I.M., Porter, C., Smith, B.E., Noh, M.J. and Morin, P. (2019). The reference elevation model of Antarctica. *The Cryosphere*, *13*(2), 665-674.

Hughes, T. (1973). Is the West Antarctic ice sheet disintegrating?. *Journal of Geophysical Research*, *78*(33), 7884-7910.

Hughes, T.J. and Fastook, J.L. (1981). Byrd Glacier: 1978–1979 field results. *Antarctic Journal of the United States*, *16*(5), 86-89.

Kassab, C.M., Licht, K.J., Petersson, R., Lindbäck, K., Graly, J.A., and Kaplan, M.R. (2019). Formation and evolution of an extensive blue ice moraine in central Transantarctic Mountains, Antarctica. *Journal of Glaciology*, *66*(255), 49-60.

Kingslake, J., Ely, J.C., Das, I., and Bell, R.E. (2017). Widespread movement of meltwater onto and across Antarctic ice shelves. *Nature*, *544*(7650), 349-352.

Konrad, H., Shepherd, A., Gilbert, L., Hogg, A.E., McMillan, M., Muir, A., and Slater, T. (2018). Net retreat of Antarctic glacier grounding lines. *Nature Geoscience*, *11*(4), 258-262.

Lague, D., Brodu, N., and Leroux, J. (2013). Accurate 3D comparison of complex topography with terrestrial laser scanner: Application to the Rangitikei canyon (NZ). *ISPRS Journal of Photogrammetry and Remote Sensing*, *82*, 10-26.

Liu, Y., Moore, J.C., Cheng, X., Gladstone, R.M., Bassis, J.N., Liu, H., Wen, J., and Hui, F. (2015). Ocean-driven thinning enhances iceberg calving and retreat of Antarctic ice shelves. *Proceedings of the National Academy of Sciences*, *112*(11), 3263-3268.

Lowe, D. G. (2004). Distinctive image features from scale-invariant keypoints. *International Journal of Computer Vision*, *60*(2), 91-110.

Marsh, O.J., Rack, W., Floricioiu, D., Golledge, N.R., and Lawson, W. (2013). Tidally-induced velocity variations of the Beardmore Glacier, Antarctica, and their representation in satellite measurements of ice velocity. *Cryosphere Discussions*, *7*(2).

McMillan, M., Shepherd, A., Sundal, A., Briggs, K., Muir, A., Ridout, A., Hogg, A., and Wingham, D. (2014). Increased ice losses from Antarctica detected by CryoSat-2. *Geophysical Research Letters*, *41*(11), 3899-3905.

McNabb, R. (2019). PyBob Software, *Download available*: https://github.com/iamdonovan/pybob

Mertes, J.R., Gulley, J.D., Benn, D.I., Thompson, S.S., and Nicholson, L.I. (2017). Using structure-from-motion to create glacier DEMs and orthoimagery from historical terrestrial and oblique aerial imagery. *Earth Surface Processes and Landforms*, *42*(14), 2350-2364.

Midgley, N.G. and Tonkin, T.N. (2017). Reconstruction of former glacier surface topography from archive oblique aerial images. *Geomorphology*, *282*, 18-26.

Moholdt, G., Padman, L., and Fricker, H.A. (2014). Basal mass budget of Ross and Filchner-Ronne ice shelves, Antarctica, derived from Lagrangian analysis of ICESat altimetry. *Journal of Geophysical Research: Earth Surface*, *119*(11), 2361-2380.

Nielsen, N.I. (2017). *Recovering Data with Digital Photogrammetry and Image Analysis Using Open Source Software*. Master's thesis, University of Oslo.

Noh, M.J. and Howat, I.M. (2015). *Automated stereo-photogrammetric DEM generation at high latitudes: Surface Extraction with TIN-based Search-space Minimization (SETSM) validation and demonstration over glaciated regions. GIScience and Remote Sensing*, *52*(2), 198-217.

Nuth, C. and Kääb, A. (2011). Co-registration and bias corrections of satellite elevation data sets for quantifying glacier thickness change. *The Cryosphere*, *5*(1), 271-290.

Paul, F., Bolch, T., Briggs, K., Kääb, A., McMillan, M., McNabb, R., Nagler, T., Nuth, C., Rastner, P., Strozzi, T., and Wuite, J. (2017). Error sources and guidelines for quality assessment

of glacier area, elevation change, and velocity products derived from satellite data in the Glaciers_cci project. *Remote Sensing of Environment*, *203*, 256-275.

Peltier, W.R., Argus, D.F., and Drummond, R. (2015). Space geodesy constrains ice-age terminal deglaciation: The global ICE-6G_C (VM5a) model. *Journal of Geophysical Research: Solid Earth, 120*(1), 450-487.

Pieczonka, T., Bolch, T., and Buchroithner, M. (2011). Generation and evaluation of multitemporal digital terrain models of the Mt. Everest area from different optical sensors. *ISPRS Journal of Photogrammetry and Remote Sensing*, *66*(6), 927-940.

Pritchard, H.D., Arthern, R.J., Vaughan, D.G., and Edwards, L.A. (2009). Extensive dynamic thinning on the margins of the Greenland and Antarctic ice sheets. *Nature*, *461*(7266), 971-975.

Pritchard, H. D., Ligtenberg, S. R., Fricher, H. A., Vaughan, D. G., van den Broeke, M. R., and Padman L. (2012). Antarctic ice-sheet loss driven by basal melting of ice shelves. *Nature, 484*(7395), 502-505.

Racoviteanu, A.E., Manley, W.F., Arnaud, Y., and Williams, M.W. (2007). Evaluating digital elevation models for glaciologic applications: An example from Nevado Coropuna, Peruvian Andes. *Global and Planetary Change*, *59*(1-4), 110-125.

Rignot, E., Mouginot, J., and Scheuchl, B. (2011). Ice flow of the Antarctic Ice Sheet. *Science*, *333*(6048), 1427-1430.

Rignot, E., Jacobs, S., Mouginot, J., and Scheuchl, B., (2013). Ice-shelf melting around Antarctica. *Science*, *341*(6143), 266-270.

Rignot, E., Mouginot, J., Scheuchl, B., van den Broeke, M., van Wessem, M.J., and Morlighem, M. (2019). Four decades of Antarctic Ice Sheet mass balance from 1979–2017. *Proceedings of the National Academy of Sciences*, *116*(4), 1095-1103.

Rupnik, E., Daakir, M., and Deseilligny, M.P. (2017). MicMac–a free, open-source solution for photogrammetry. *Open Geospatial Data, Software and Standards*, *2*(14).

Scambos, T.A., Bohlander, J.A., Shuman, C.U., and Skvarca, P. (2004). Glacier acceleration and thinning after ice shelf collapse in the Larsen B embayment, Antarctica. *Geophysical Research Letters*, *31*(18).

Scambos, T.A., Berthier, E., and Shuman, C.A. (2011). The triggering of subglacial lake drainage during rapid glacier drawdown: Crane Glacier, Antarctic Peninsula. *Annals of Glaciology*, *52*(59), 74-82.

Schiefer, E. and Gilbert, R. (2007). Reconstructing morphometric change in a proglacial landscape using historical aerial photography and automated DEM generation. *Geomorphology*, *88*(1-2), 167-178.

Schodlok, M.P., Menemenlis, D., and Rignot, E.J. (2016). Ice shelf basal melt rates around Antarctica from simulations and observations. *Journal of Geophysical Research: Oceans, 12*(2), 1085-1109.

Schoof, C. (2007). Ice Sheet grounding line dynamics: Steady states, stability, and hysteresis. *Journal of Geophysical Research: Earth Surface, 112*(F3).

Schröder, L., Horwath, M., Dietrich, R., Helm, V., Van Den Broeke, M.R., and Ligtenberg, S.R. (2019). Four decades of Antarctic surface elevation changes from multi-mission satellite altimetry. *The Cryosphere*, *13*(2), 427-449.

Shepherd, A., Ivins, E., Rignot, E., Smith, B., Van Den Broeke, M., Velicogna, I., Whitehouse, P., Briggs, K., Joughin, I., Krinner, G., and Nowicki, S. (2018). Mass balance of the Antarctic Ice Sheet from 1992 to 2017. *Nature*, *558*, 219-222.

Shepherd, A., Gilbert, L., Muir, A.S., Konrad, H., McMillan, M., Slater, T., Briggs, K.H., Sundal, A.V., Hogg, A.E., and Engdahl, M. (2019). Trends in Antarctic Ice Sheet Elevation and Mass. *Geophysical Research Letters*. *46*(14), 8174-8183.

Slater, T., Shepherd, A., McMillan, M., Muir, A., Gilbert, L., Hogg, A.E., Konrad, H., and Parrinello, T. (2018). A new digital elevation model of Antarctica derived from CryoSat-2 altimetry. *The Cryosphere*, *12*(4), 1551-1562.

Stearns, L.A. (2007). Outlet glacier dynamics in east Greenland and East Antarctica. PhD, University of Maine.

Stearns, L. A., Smith, B. E., and Hamilton, G. S. (2008). Increased flow speed on a large East Antarctic outlet glacier caused by subglacial floods. *Nature Geoscience, 1*, 827-831.

Thomas, R., Frederick, E., Krabill, W., Manizade, S., and Martin, C. (2009). Recent changes on Greenland outlet glaciers. *Journal of Glaciology*, *55*(189), 147-162.

Tinto, K.J., Padman, L., Siddoway, C.S., Springer, S.R., Fricker, H.A., Das, I., Tontini, F.C., Porter, D.F., Frearson, N.P., Howard, S.L., and Siegfried, M.R. (2019). Ross Ice Shelf response to climate driven by the tectonic imprint on seafloor bathymetry. *Nature Geoscience, 12.* 441–449.

Van Reeth, E. W. (1966). Aerial Photography in Antarctica. *Antarctic Journal of the United States 1* (2). 66-68.

Van Wessem, J.M., Jan Van De Berg, W., Noël, B.P., Van Meijgaard, E., Amory, C., Birnbaum, G., Jakobs, C.L., Krüger, K., Lenaerts, J., Lhermitte, S., and Ligtenberg, S.R. (2018). Modelling the climate and surface mass balance of polar ice sheets using RACMO2: Part 2: Antarctica (1979-2016). *The Cryosphere*, *12*(4), 1479-1498.

Vaughan, D.G., Comiso, J.C., Allison, I., Carrasco, J., Kaser, G., Kwok, R., Mote, P., Murray, T., Paul, F., Ren, J., Rignot, E., Solomina, O., Steffen, K., and Zhang, T. (2013): Observations: Cryosphere. In: Climate Change 2013: The Physical Science Basis. Contribution of Working Group I to the Fifth Assessment Report of the Intergovernmental Panel on Climate Change [Stocker, T.F., Qin, D., Plattner, G.-K., Tignor, M., Allen, S.K., Boschung, J., Nauels, A., Xia, Y., Bex, V., and Midgley, P.M. (eds.)]. Cambridge University Press, Cambridge, United Kingdom and New York, NY, USA.

Whitmore, G. D. and Southard Jr, R. B. (1966). Topographic mapping in Antarctica by the U.S. Geological Survey. *Antarctic Journal of the United States, 1*(2). 40-50.

Zwally, H.J., Li, J., Robbins, J.W., Saba, J.L., Yi, D., and Brenner, A.C. (2015). Mass gains of the Antarctic ice sheet exceed losses. *Journal of Glaciology, 61*(230), 1019-1036.

Chapter 3
Basal crevasse formation as proxy for past subglacial flooding events

3.1 Introduction

Basal crevasses are common on Antarctic ice shelves. They form when tensile stress and water pressure (which act to widen the crevasse) exceed lithostatic stress (which acts to close it) (Rist et al., 1996, 2002; Van der Veen, 1998). Basal crevasses seem to form exclusively at glacier grounding lines, then advect down-flow through the ice shelf, often providing zones of weakness at which icebergs detach (Jezek, 1984; Luckman et al., 2012).

The location and geometry of basal crevasses can be mapped with ground-based or airborne radar measurements (Jezek et al., 1979; Jezek and Bentley, 1983; McGrath et al., 2012; Luckman et al., 2012; Vaughan et al., 2012). Along the Byrd Glacier flowline, these radar measurements show that basal crevasses are neither uniformly sized nor spaced. If crevassing does not occur at regular time intervals, then there must be short-term variations in the stresses modulating crevasse initiation (tensile stress, water pressure, or lithostatic stress). Of these three, tensile stress is the one that undergoes short-term variations, as exhibited by changes in ice velocity.

In this study, we investigate the formation and evolution of basal crevasses extending from the Byrd Glacier grounding line onto the Ross Ice Shelf (Figure 3.1). We identify over 300 basal crevasses within ~5 km of the grounding line. Of the crevasses whose heights we are able to measure, 86% are shorter than 100 m, but a few crevasses, including the one closest to the grounding line, are larger than 150 m tall. We hypothesize that the rapid drainage of Lake 2

(Figure 3.1) of the two large subglacial lakes in the Byrd Glacier catchment (Stearns et al., 2008; Carter et al., 2017) led to the formation of an anomalously large basal crevasse at the grounding line. Because large basal crevasses cause surface depressions, we explore whether the train of surface depressions between Byrd Glacier and the edge of the Ross Ice Shelf can be used as proxies for past subglacial flooding events.

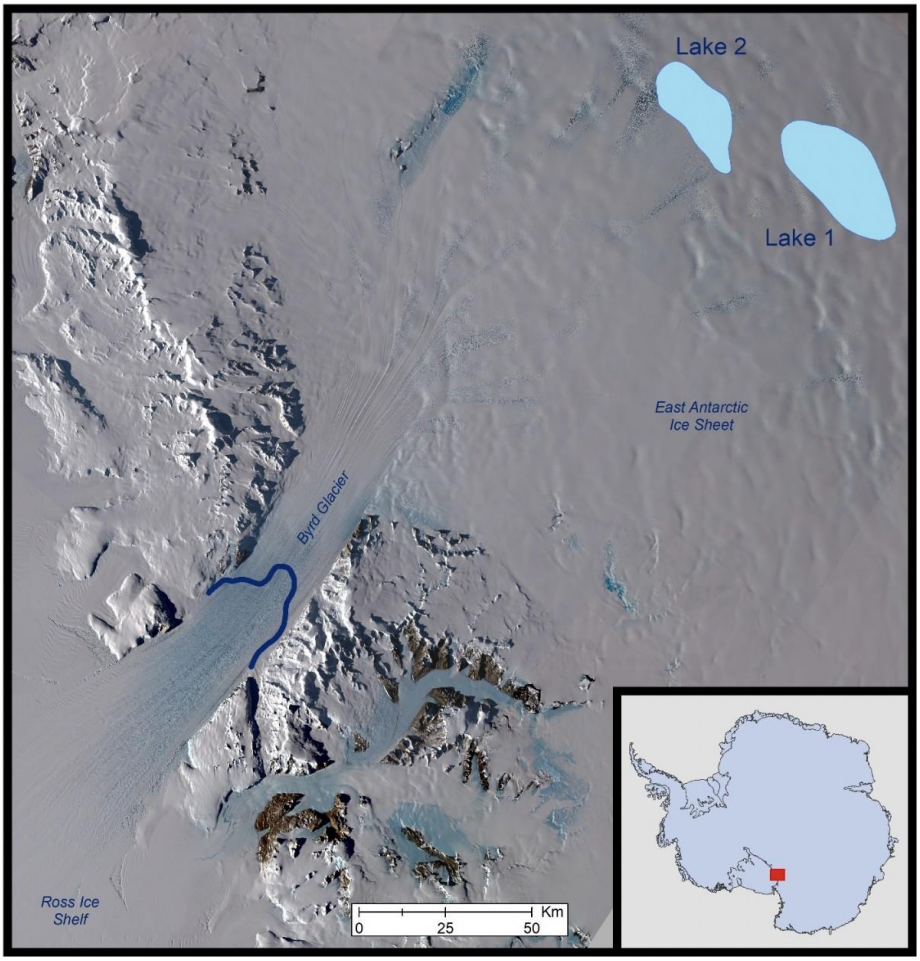

Figure 3.1: Map of Byrd Glacier and the subglacial lakes located ~175 km up-flow from the grounding line (Stearns et al., 2008). The violet line is the grounding line and the background image is Landsat 8 OLI from January-February 2019. The trunk of Byrd Glacier is ~25 km wide and ~100 km long; ice flow is from the top right to the bottom left.

3.2 Data and Methods

3.2.1 Grounding Line Location

Basal crevasses appear to only form at the grounding line, where tensile stresses and water pressure can exceed the lithostatic stress (Jezek and Bentley, 1983; Bentley,1987). To identify the grounding line location, we use both *in situ* observations and satellite data. From 2010 to 2013, a grid of nine GPS receivers was deployed near the grounding line, spanning an along-flow distance of 190 km. Tidal flexure is clearly visible in the GPS data (profiles in Figure 3.2), allowing us to delineate floating versus grounded ice.

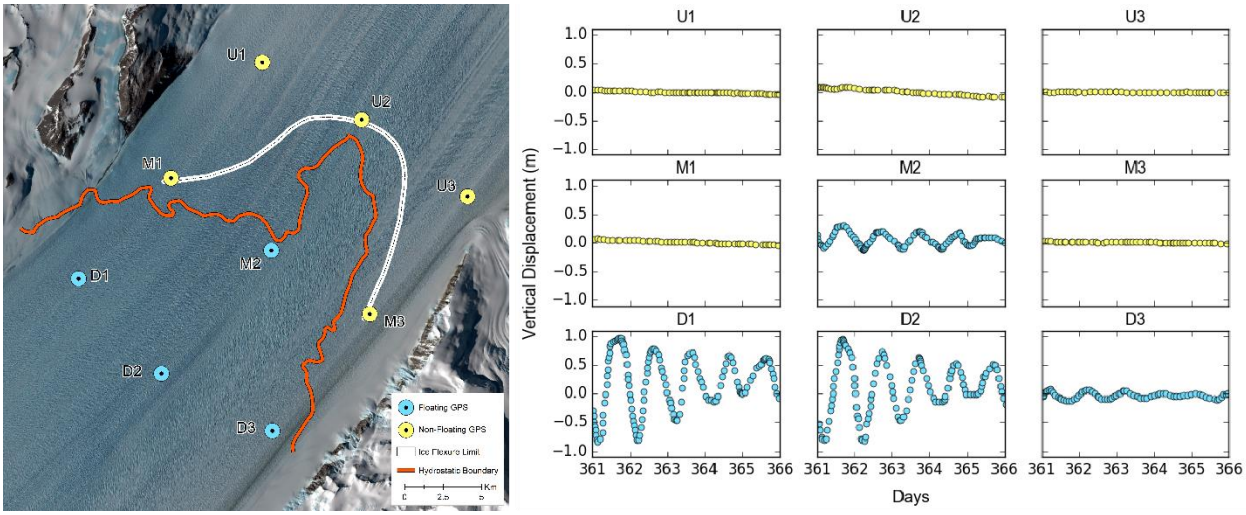

Figure 3.2: A) The grounding zone is between the limit of tidal flexure (white line) and hydro- static equilibrium (orange line) (after Fricker et al. (2009) and Brunt et al. (2010)). GPS labels represent up (U), middle (M), and down (D); the vertical component of each receiver is shown in panel B.

The grounding zone is estimated to be between the tidal flexure limit and the hydrostatic equilibrium boundary (between white and orange lines in Figure 3.2) (Vaughan, 1994; Fricker and Padman, 2006; Brunt et al., 2010). We calculate hydrostatic equilibrium using digital elevation model (DEM) strips derived from high resolution satellite imagery. In particular, we use DEM

strips generated from the search-space minimization algorithm of WorldView 1,2,3 imagery (Noh and Howat, 2015; Howat et al., 2019). This technique quotes a vertical error of ~1 m for imagery collected at low degrees of nadir and co-registered with substantial ground control. The degree of nadir for the imagery we use ranges from 6°-29°, so we assume a higher error of 5 m. Blunders from clouds, shadows, or the lee-side of terrain are clipped and then neighboring strops are co-registered using methodology from Nuth and Kääb (2011). The present-day DEM is a mosaicked 5 m grid of the co-registered DEM strips from 2016-2017 and referenced to the WGS84 ellipsoid. The present-day DEM is used to calculate the hydrostatic equilibrium (H_e) as,

$$H_e = h - \left(H * \left[\frac{\rho_w - \rho_i}{\rho_w}\right]\right), \qquad (3.1)$$

where h is the present-day surface elevation, H is the ice thickness, and ρ_i, ρ_w are the ice and water density, respectively. The ice thickness is estimated by subtracting bed topography values, which were manually picked from radar echograms (Gogineni et al., 2014) from the surface elevation DEM.

3.2.2 Basal crevasse geometry

3.2.2.1 Observed crevasse locations and heights

A dense grid of airborne radar data was collected by the Center for Remote Sensing of Ice Sheets (CReSIS) over Byrd Glacier in 2011-2012, with the radar depth sounder (MCoRDS V2) operating at 180-210 MHz (Gogineni et al., 2014). In this study, we use the individual echograms. Main sources of error for MCoRDS V2 are multiple reflectors, electronic noise, and

off-nadir reflections (CReSIS, 2014), which may lead to an error estimate of 30.6 m for gridded products (Gogineni et al., 2014). Elevations are referenced to the WGS84 ellipsoid.

We identify basal crevasses directly from the MCoRDS V2 echograms. Basal crevasses that are open in the same direction as the radar flight will appear as hyperbola in radar echograms, and the apex of those hyperbola represents the height of the fracture. In some cases, basal crevasses are so numerous that the asymptotes of neighboring hyperbola intersect and estimating crevasse height is not possible. We only report crevasse heights where both asymptotes are clearly identifiable.

3.2.2.2 Modeled crevasse locations and heights

Radar data were only collected in 2011-2012 — not coincident with the subglacial flooding event in 2006. We model basal crevasse heights using linear elastic fracture mechanics (LEFM) based on surface velocity variations pre-flood and during the flood. LEFM calculates a stress intensity factor (K_I); when this stress intensity factor exceeds the fracture criterion, or ice toughness, then a crack will propagate (Rist et al., 1996; Van der Veen, 1998), following:

$$K_I = \int_0^{h_0} \frac{2\theta_n(z)}{\sqrt{\pi h}} G(\gamma, \lambda) dz, \qquad (3.2)$$

Rearranging the above equation, we can solve for h, which is the height of the basal crevasse,

$$h = \frac{4}{\pi}\left[K_I^{-1} \int_0^{h_0} \theta_n(z) G(\gamma, \lambda) dz\right]^2, \qquad (3.3)$$

Here, h_0 is the size of the starter crack, which we set to 2 m after Rist et al. (2002) and a value of 0.155 $MPa\ m^{\frac{1}{2}}$ for K_I (Rist et al., 1999). H is the ice thickness, and z is the depth within the glacier, $G(\gamma, \lambda)$ is a function of $\lambda = \frac{h}{H}$ and $\gamma = \frac{z}{h}$ established from fitting a polynomial curve to the modeled stress intensity values (Van der Veen, 1998). $\theta_n(z)$ represents the combined stresses (tensile, lithostatic, and water pressure) acting at the crevasse tip. Tensile stress is calculated from strain rates, following Glen's Flow Law, and using a rate factor appropriate for surface ice at -20°C (after Van der Veen et al. 2014).

3.2.2.3 Surface depressions

Ice overlaying a large basal crevasse must adjust to hydrostatic equilibrium by forming a surface depression (Shabtaie and Bentley, 1982; Luckman et al., 2012). Several radar studies describe the relationship between surface depressions and basal crevasses (Jezek et al., 1979; Luckman et al., 2012; McGrath et al., 2012; Humbert et al., 2015). On Byrd Glacier, anomalously large basal crevasses have overlying surface depressions that are detectable from radar echograms and optical satellite imagery (See Figure 3.5).

We use Landsat 8 OLI imagery (Band 8, at 15 m) from 2016-2017 to identify surface depressions. Surface depressions are discernible in optical imagery because the surface crevasses within the depression have different reflectance values than their surroundings. Outlines of surface depression boundaries are manually drawn, and the centroids of those polygons are derived as points for particle tracking.

Assuming basal crevasses form at the grounding line, we can determine when they originated using a particle tracking algorithm (after Konikow and Bredehoeft (1978)). This algorithm requires information about ice velocity and flow direction. The lack of merging flow bands extending from Byrd Glacier to the Ross Ice Shelf's (RIS) edge suggests a generally steady flow speed (Hulbe and Fahnestock, 2007; LeDoux et al., 2017). This is an indicator that the ice has maintained a consistent speed and stress regime for centuries (Hulbe and Fahnestock, 2007), which allows us to use present-day velocities and flow directions to infer how basal crevasses advected. We use publicly available ice velocity data from Landsat Ice Speed of Antarctica (LISA; (Scambos et al., 2019)). LISA mosaics have a spatial resolution of 750 m; the velocities were generated from imagery collected July 1, 2016 to April 30, 2017. We actually track the depressions 'up-flow' towards the grounding line, which allows us to determine the flow path of every depression and an estimate of when each crevasse formed at the grounding line.

3.3 Results

3.3.1 Grounding line location

We locate the grounding line between the limits of tidal flexure (determined from GPS) and hydrostatic equilibrium (calculated using airborne- and satellite-data) (Figure 3.2). The grounding line we identify is similar in shape and location to one derived from tidal flexure in TerraSAR-X data (Floricioiu et al., 2012); it differs by ~7 km from one calculated using hydrostatic equilibrium on a coarser DEM (Van der Veen et al., 2014).

3.3.2 Basal crevasse geometry

The floating base of Byrd Glacier is heavily crevassed within the fjord and out on RIS. Both observational and modeling results reveal that Byrd Glacier is susceptible to crevassing of varying sizes and clustering.

3.3.2.1 Observed crevasse locations and heights

We identify ~300 basal crevasses by locating the hyperbole apex in 2011/12 CReSIS echograms (Figure 3.3). Crevasse distribution is most dense within the glacier fjord and decreases as ice flows into the RIS. Crevasses range in height from ~40-335 m with a mean height of 118 m; their widths range from ~0.08-1.2 km, with an average width of 0.625 km. We ignore hyperbole found in echograms collected near the glacier margins because high shear stresses mean that these are likely Mode 2 crevasses (Van der Veen, 1998) whose initiation did not necessarily occur within the grounding zone. Of the 300 hyperbole in Figure 3.3, we can confidently determine the height of 107 basal crevasses where both asymptotes are clearly visible. These 100+ crevasses are located within the region of centrally flowing ice where shear stress is zero (Whillans et al., 1989), and initial crevasse propagation is due only to tensile stresses (Van der Veen, 1998).

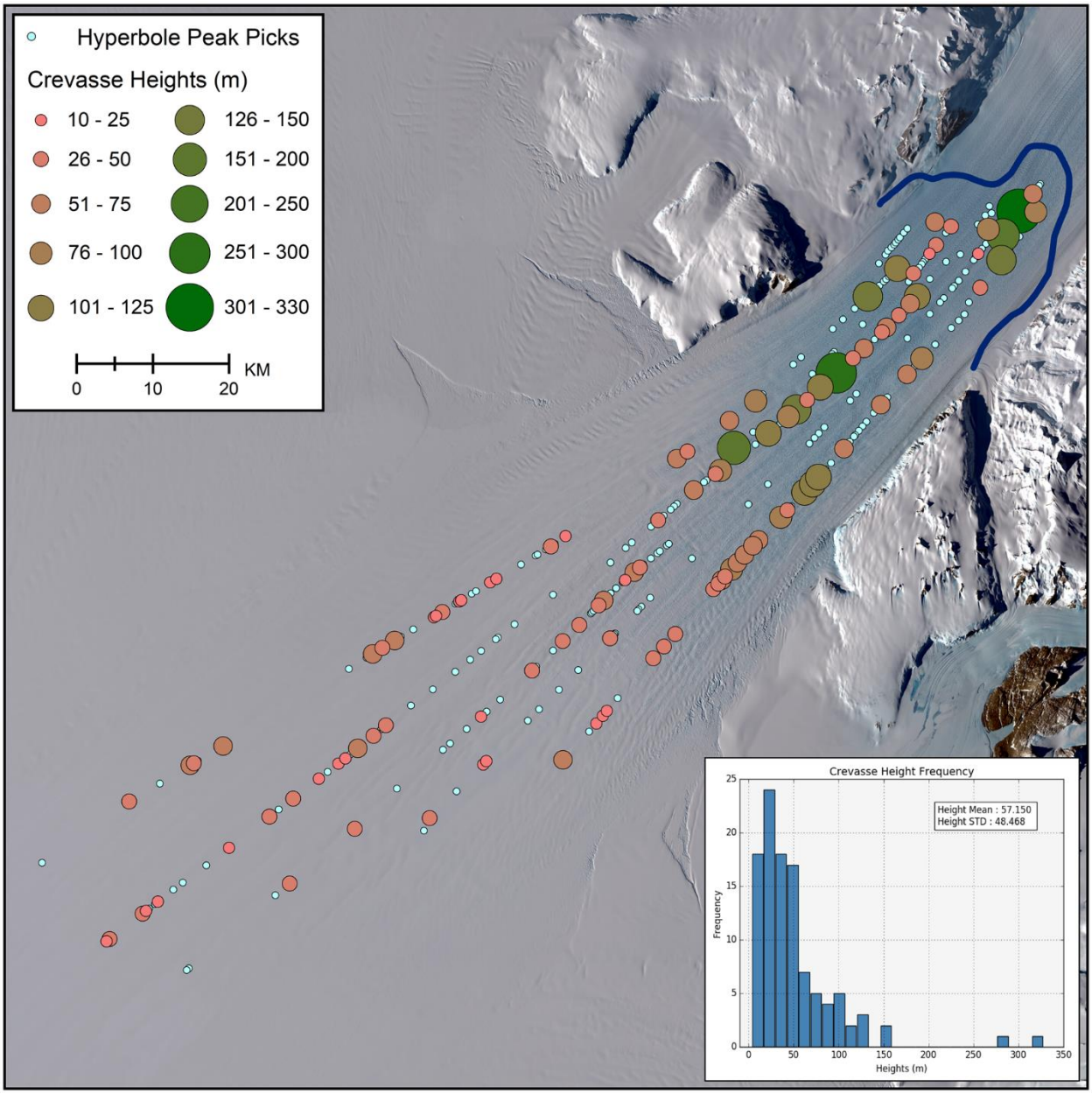

Figure 3.3: Locations of basal crevasses identified from hyperbola apex observed in airborne radar echograms (light-blue circles). Included in the figure are the 107 crevasses whose heights we were able to measure represented by both the green to coral grades in color size gradients. The histogram located in the bottom right corner is of crevasse heights.

3.3.2.2 Modeled crevasse locations and heights

We calculate basal crevasse height with LEFM (Equation 3, Figure 3.4) using strain rates derived during the subglacial flood event, when the glacier flowed ~10% faster, and during a non-flood

period. Due to image availability, it is impossible to pinpoint the exact timing of the acceleration, but it was likely during the second half of 2006 (Stearns et al., 2008).

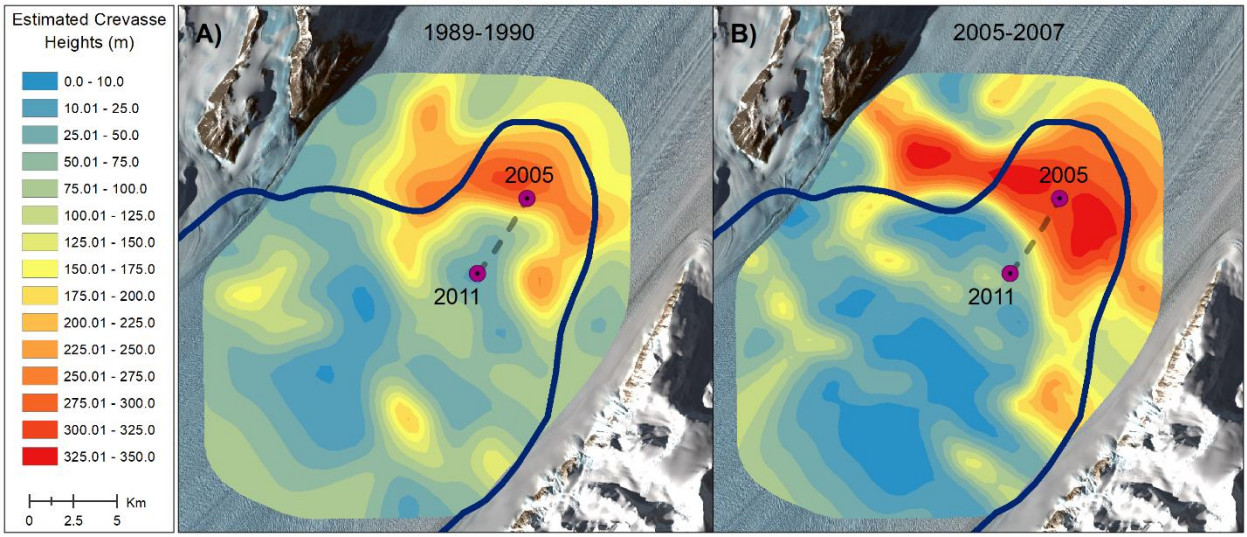

Figure 3.4: Estimated basal crevasse heights from LEFM modeling. A) LEFM results using strain rates derived from a 'non-flooding' period (1989-1990). B) LEFM results using strain rates derived during the glacier's acceleration (2005-2007). The purple points represent the approximated location of the ~335 m tall basal crevasse by year from 2005-2011. The blue line is the grounding line.

In both ice flow scenarios, greatest initial fracturing begins near the grounding zone, but faster ice flow and higher longitudinal strain rates in 2006 produce propagated heights ~75 m higher than in 'normal', non-flood, periods (Figure 3.4). This is particularly clear if we look exactly where the large basal crevasse would have formed in 2006 which was ~335 m tall when it was observed in 2011/12. LEFM results estimate propagation heights of 90-225 m during non-flood periods, and 285-300 m during flood periods.

3.3.2.3 Surface depressions

Surface depressions do not form instantaneously over large basal crevasses. Viscous creep at Byrd Glacier is slow (Van der Veen et al., 2014), and it will take several years for the ice to adjust

to its new ice thickness. The ~335 m crevasse identified in the radar echogram (in 2011) that we hypothesize was formed from the flooding event in 2006, has not yet formed a surface depression. The second largest basal crevasse is estimated to have formed in 1962-1963 (Figure 3.5). Landsat imagery shows no surface depression in 1988 or 1989, but one in 1990. Therefore, it took between 27-28 years for a surface depression to form directly above a large basal crevasse. At this rate, we would not expect to see a surface depression until 2033-2034. We do not observe surface depressions over shorter basal crevasses. The surface depressions that form over large basal crevasses have a distinct appearance and are not observed on the Ross Ice Shelf anywhere outside of the Byrd Glacier flow path. While other depressions exist, they appear more like rifts (narrow, long, with sharp edges), while the Byrd surface depressions are rounded and smooth.

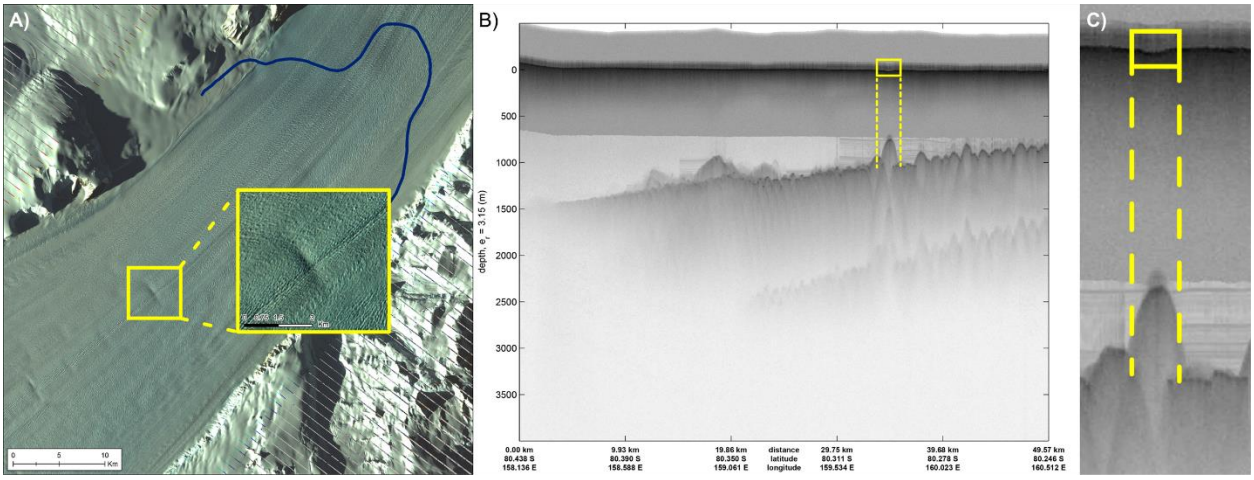

Figure 3.5: Identifying surface depressions: A) The surface depression overlaying a large ~290 m tall basal crevasse (shown in panels B) and C). The background is a Landsat 7 ETM+ image (Bands 2,3,4) acquired on February 22, 2011, approximately 10 months before CReSIS data were collected. B) CReSIS echogram (ID: 20111205 08 003) highlighting the ~290 m tall crevasse in yellow. C) Zoomed-in view of the same crevasse and overlying surface depression.

We identify 28 significant surface depressions over a distance of ~400 km from Byrd Glacier's grounding line to the RIS terminus (Figure 3.6). From particle tracking, the oldest surface

depression is estimated to have formed ~600 years ago; the average interval between surface depression formation is 22 years (Table 3.1).

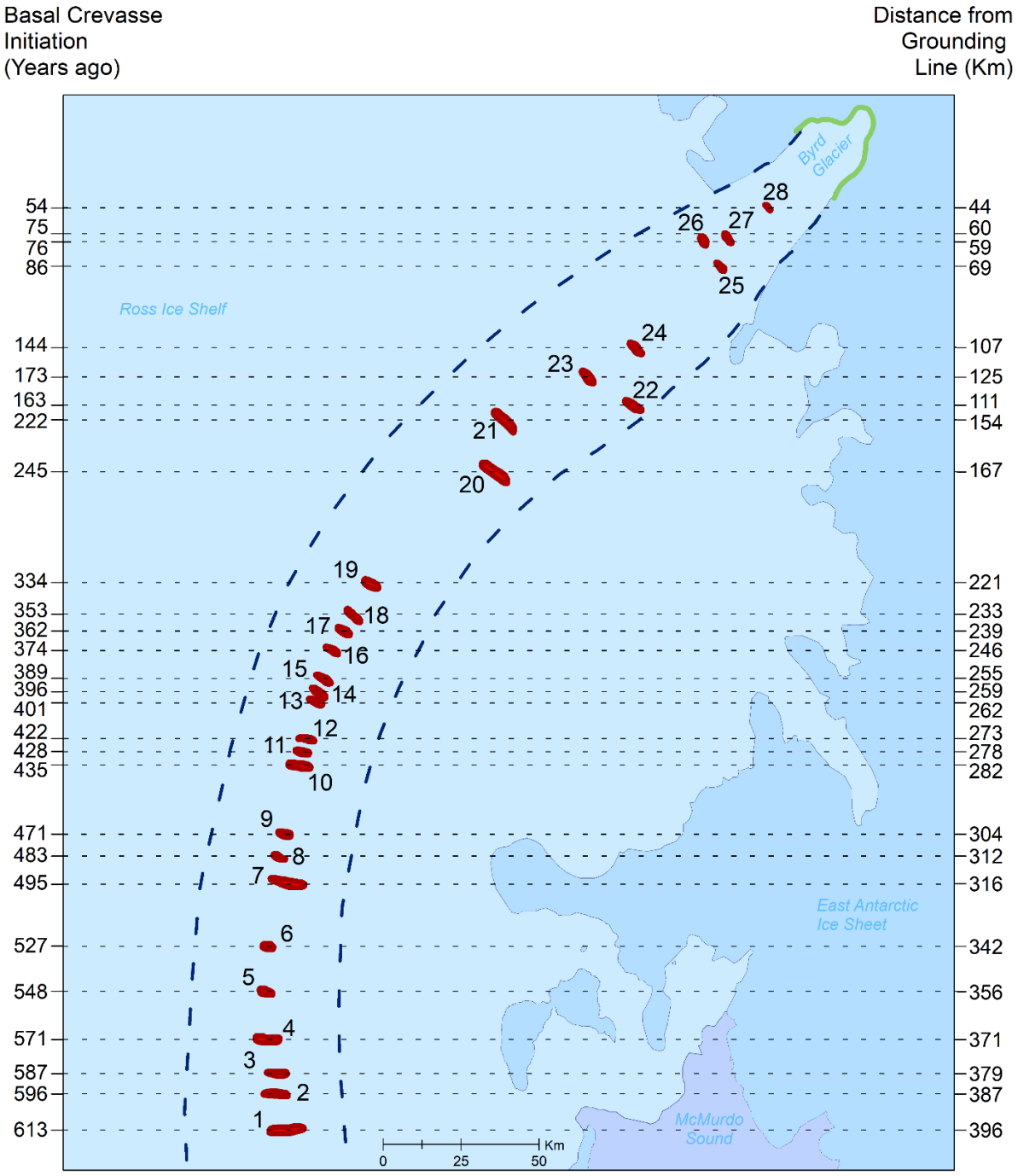

Figure 3.6: Red polygons show the locations of surface depressions extending from the Byrd Glacier grounding line to the edge of the Ross Ice Shelf. The age of individual crevasses is shown on the left side of the map; distance from the grounding line (green line) is shown on the right. Numbers next to the red polygons correspond with the numbers in Table 3.1. The dashed blue line is the boundary of Byrd Glacier's ice flow. We do not see any surface depressions outside of these flowlines.

Depression ID	# of Depressions	Year Formed	Age Range	Distance (km)
1-6	6	1400-1499	527-613	342-396
7-12	6	1500-1599	422-495	273-316
13-19	7	1600-1699	334-401	221-262
20-21	2	1700-1799	222-245	154-167
22-24	3	1800-1899	144-163	107-111
25-28	4	1900-1999	54-86	44-69

Table 3.1: Number of surface depressions that formed each century, with age and distance from grounding line

3.4 Discussion

Crevasse heights are not uniform extending from the Byrd Glacier grounding line to the Ross Ice Shelf. Most crevasses are <50 m tall (Figure 3.3) and do not form surface depressions; the 28 surface depressions suggest the under-laying basal crevasses were at some point abnormally large. We hypothesize that these large basal crevasses form during rapid subglacial drainage events (e.g. Stearns et al., 2008). Subglacial drainage events cause glacier acceleration, which increases the tensile stress at the grounding line. In addition, the large amount of water flowing across the grounding line likely enhances melt of any pre-existing basal crevasse. Below, we outline how these two processes can cause anomalously large basal crevasses to form during drainage events.

3.4.1 Large basal crevasse formation and glacier acceleration

When ice flow accelerates near the grounding line, tensile stress also increases. LEFM results show that when tensile stress increases, basal crevasse propagation heights are higher. Ice velocity derived from satellite remote sensing show that Byrd Glacier can flow up to ~10%

faster during subglacial drainage events. This acceleration has the potential to increase crevasse height by ~75 m.

To the best of our knowledge, the only other study to report Antarctic ice shelf basal crevasses > 300m is Rist et al. (2002). However, unlike the basal crevasses initiating at Byrd Glacier, those observed by Rist et al. (2002) are rifts (Swithinbank and Lucchitta, 1986). Rifts, though technically basal crevasses, are fractures that have propagated through the entire ice thickness from tensile stresses (Cuffey and Paterson, 2010). The observed rifts from Rist et al. (2002) initiate from the Rutford Ice Stream and also do not appear at regular intervals along the Ronne Ice Shelf. It is likely that ice flow from Rutford Ice Stream has also experienced intermittent acceleration events that have caused episodically large basal crevasses (which become full-fracture rifts).

Rist et al. (2002) also hypothesizes that short-term variations in ice dynamics cause abnormally large fracturing in Antarctica. While the fractures appear to persist for centuries on Byrd Glacier, they do not seem to influence its stability. On other ice shelves like Larsen C (Hogg and Gudmundsson, 2017) and Filchner (Ferrigno and Gould, 1987) basal crevasses become full-fracture rifts and have led to the calving of considerably large tabular icebergs. The Byrd Glacier basal crevasses do not evolve into rifts that produce tabular icebergs. To date, there are no data available that show that the large basal crevasses initiated at Byrd Glacier's grounding line have any impact on glacier or the ice shelf stability.

3.4.2 Large basal crevasse formation and subglacial drainage events

LEFM underestimates the height of the 330 m tall crevasse by 30-45 m or 10-14% of the height derived from radar echograms. A possible explanation for this difference is that LEFM only predicts the initial propagation height and not the evolved height of the crevasse. It is likely that the emergence of a freshwater plume at the grounding line during a subglacial flood event caused additional localized melting (Marsh et al., 2016).

Jenkins (2011) modelled melt rates for Byrd Glacier when a freshwater plume is the result of a subglacial lake flooding event and when the plume is due to discharge from basal deformational melt. During a flooding event, Jenkins (2011) estimates basal melt of 15.9 m/yr and melt of 5.64 m/yr from non-flood event years.

Lake 2 in Figure 3.1 began draining in June 2006 and ended March 2007. The radar data was collected December 2011. There are 67 months from June 2006 to December 2011, and if we assume an annual melt rate of 15.9 m/yr for the first 9 months and a rate of 5.64 m/yr for the remaining 58 months, then the total melt for that timeline is 39.19 m. By adding this amount of deformation to the LEFM estimated heights, the crevasse height would then be 324-339 m tall, which is within range of the measured crevasse.

3.4.3 Implications

Ice shelves can act as a “plug” for outlet glaciers where their presence maintains stable outlet glacier ice flow (Dupont and Alley, 2005; Depoorter et al., 2013). It is here that the majority of mass loss in Antarctica occurs (Rignot et al., 2013) through basal melt and iceberg calving. There

appears to be a direct link between the stability of ice shelves and the mass balance of outlet glaciers draining into the ice shelves. Following the Larsen B Ice Shelf collapse of 2002, the inflowing outlet glaciers underwent sustained acceleration and increased ice discharge (Scambos et al., 2004). These events can be elicited by weakened buttressing from large calving events triggered by basal crevasses forming rifts (Rott et al., 1996; Hogg and Gudmundsson, 2017). Basal crevasses play an integral role in iceberg formation (Colgan et al., 2016) and provide greater surface area for basal melt processes (Hellmer and Jacobs, 1992).

The subglacial hydrology of Antarctica also affects ice shelf stability from grounding line drainage events. Subglacial channels on ice shelves are known to evolve and grow from the influx of fresh subglacial water (Le Brocq et al., 2013; Marsh et al., 2016; Simkins et al., 2017; Dow et al., 2018), which is another means of increasing basal surface area for further melt to take place. These basal water melt-induced channels are the initiating factor forming basal crevasses that are parallel to flow and located at the crest of the channels on Pine Island Glacier (Vaughan et al., 2012). This is subsequently another means of crevasse propagation as a consequence of subglacial water influx. The Antarctic basal hydrologic system influences the stability of ice shelves through its impact on glacier dynamics (speedincreases leading to crevasse propagation) at the grounding line and melt rates of floating glacier ice. Having a better understanding of the drivers behind basal crevasse production has the potential to aid in better constraining of predictive models about the future of both ice shelves and ice sheets.

3.5 Conclusion

There is an extensive number of basal crevasses on Byrd Glacier, propagating from tensile stresses, and resulting in a wide range of geometries. We confidently identify the apex and two asymptotes of hyperbole from 2011/12 radar data of 107 basal crevasses which allows us to estimate their heights and horizontal locations. The spatial pattern of the heights appears to be random, indicating that Byrd Glacier undergoes intermittent variations in its stress regime.

We also locate a series of surface depressions from the fjord of Byrd Glacier to the terminus of the RIS. The depressions within the fjord are observed to directly overlay only abnormally large basal crevasses to which we hypothesize that the rest of the depressions in the RIS are also overlaying abnormally large crevasses. Assuming that the basal crevasses initiated at the grounding line, we use feature tracking to estimate the ages of the depressions, which gives a timeline of abnormally large basal crevasse formation over six-centuries.

Modeling results from flood-period velocities estimates greater initial basal crevasse propagation heights than LEFM results calculated with non-flood-period velocities. The initial heights are smaller than the measured geometries from radar echograms, but by including melt rates modeled by Jenkins (2011) over a timeline from initiation to when the radar data was collected, we approximate a range of crevasse heights than falls within range of the radar data.

The increased tensile stresses that incurred during the 2005-2007 flooding event were large enough to cause an abnormally large basal crevasse. At present, a surface depression has not

formed over this basal crevasses, but given the temporal spacing of the last surface depression that formed over an abnormally large basal crevasse, we expect a surface depression to form over the ~335 m tall crevasse within the next 12-13 years.

We hypothesize that all abnormally large basal crevasses on Byrd Glacier form as a result of subglacial flooding speedups, thereby making basal crevasses proxies for past subglacially induced velocity increases. By tracking the present-day location of surface depressions, which are located directly above abnormally large basal crevasses, back in time to the grounding zone, we are able to create a timeline for 28 past subglacial flooding events.

Chapter 3 Citations

Bentley, C. R. (1987). Antarctic ice streams: a review. *Journal of Geophysical Research: Solid Earth*, *92* (B9), 8843–8858.

Brunt, K. M., Fricker, H. A., Padman, L., Scambos, T. A., and O'Neel, S. (2010). Mapping the grounding zone of the Ross Ice Shelf, Antarctica, using ICESat laser altimetry. *Annals of Glaciology*, *51* (55), 71–79.

Carter, S. P., Fricker, H. A., and Siegfried, M. R. (2017). Antarctic subglacial lakes drain through sediment-floored canals: theory and model testing on real and idealized domains. *The Cryosphere*, *11* (1).

Colgan, W., Rajaram, H., Abdalati, W., McCutchan, C., Mottram, R., Moussavi, M. S., and Grigsby, S. (2016). Glacier crevasses: Observations, models, and mass balance implications. *Reviews of Geophysics*, *54* (1), 119-161.

CReSIS. (2014). *Antarctica 2011 Twin Otter Data, Lawrence, Kansas, USA. Digital Media*. Retrieved from http://dara.cresis.ku.edu/.

Cuffey, K. M., and Paterson, W. S. B. (2010). *The Physics of Glaciers*. Academic Press.

Depoorter, M.A., Bamber, J.L., Griggs, J.A., Lenaerts, J.T., Ligtenberg, S.R., van den Broeke, M.R. and Moholdt, G. (2013). Calving fluxes and basal melt rates of Antarctic ice shelves. *Nature*, *502* (7469), 89-92.

Dow, C. F., Lee, W. S., Greenbaum, J. S., Greene, C. A., Blankenship, D. D. Poinar, K., Forrest, A.L., Young, D.A., and Zappa, C. J. (2018). Basal channels drive active surface hydrology and transverse ice shelf fracture. *Science Advances*, *4* (6), eaao7212.

Dupont, T.K. and Alley, R.B. (2005). Assessment of the importance of ice-shelf buttressing to ice-sheet flow. *Geophysical Research Letters*, *32* (4).

Ferrigno, J., and Gould, W. (1987). Substantial changes in the coastline of Antarctica revealed by satellite imagery. *Polar Record*, *23* (146), 577-583.

Floricioiu, D., Jezek, K., Baessler, M., and Jaber, W. A. (2012). Geophysical parameters estimation with TerraSAR-X of outlet glaciers in the Transantarctic Mountains. *2012 IEEE International Geoscience and Remote Sensing Symposium*, 1565-1568.

Fricker, H. A., and Padman, L. (2006). Ice shelf grounding zone structure from ICESat laser altimetry. *Geophysical Research Letters*, *33* (15).

Fricker, H. A., Coleman, R., Padman, L., Scambos, T. A., Bohlander, J., and Brunt, K. M. (2009). Mapping the grounding zone of the Amery Ice Shelf, East Antarctica using InSAR, Modis and ICESat. *Antarctic Science*, *21* (5), 515–532.

Gogineni, S., Yan, J.-B., Paden, J. D., Leuschen, C. J., Li, J., Rodriguez-Morales, F., Braaten, D.A., Purdon, K., Wang, Z., Liu, W. and Gauch, J. (2014). Bed topography of Jakobshavn Isbræ, Greenland, and Byrd Glacier, Antarctica. *Journal of Glaciology*, *60*(223), 813-883.

Hellmer, H. H., and Jacobs, S. S. (1992). Ocean interactions with the base of Amery Ice Shelf, Antarctica. *Journal of Geophysical Research: Oceans*, *97*(12).

Hogg, A. E., and Gudmundsson, G. H. (2017). Impacts of the Larsen-C Ice Shelf calving event. *Nature Climate Change*, *7* (8), 540-542.

Howat, I. M., Porter, C., Smith, B. E., Noh, M.-J., and Morin, P. (2019). The Reference Elevation Model of Antarctica. *The Cryosphere*, *13* (2), 665–674.

Hulbe, C., and Fahnestock, M. (2007). Century-scale discharge stagnation and re-activation of the Ross ice streams, West Antarctica. *Journal of Geophysical Research: Earth Surface*, *112* (3).

Humbert, A., Steinhage, D., Helm, V., Hoerz, S., Berendt, J., Leipprand, E., Christmann, J., Plate, C. and Müller, R. (2015). On the link between surface and basal structures of the Jelbart Ice Shelf, Antarctica. *Journal of Glaciology 61* (229), 975-986.

Jenkins, A. (2011). Convection-driven melting near the grounding lines of ice shelves and tidewater glaciers. *Journal of Physical Oceanography*, *41*(12).

Jezek, K. C. (1984). A modified theory of bottom crevasses used as a means for measuring the buttressing effect of ice shelves on inland ice sheets. *Journal of Geophysical Research: Solid Earth*, *89* (3).

Jezek, K. C., and Bentley, C. R. (1983). Field studies of bottom crevasses in the Ross Ice Shelf, antarctica. *Journal of Glaciology*, *29*(101), 118-126.

Jezek, K. C., Bentley, C. R., and Clough, J. W. (1979). Electromagnetic sounding of bottom crevasses on the Ross Ice Shelf, Antarctica. *Journal of Glaciology*, *24* (90), 321-330.

Konikow, L. F., and Bredehoeft, J. D. (1978). *Computer model of two-dimensional solute transport and dispersion in ground water* (Vol. 2) (No. 7). US Government Printing Office, Washington, D.C.

Le Brocq, A. M., Ross, N., Griggs, J. A., Bingham, R. G., Corr, H. F., Ferraccioli, F., and Jenkins, A. (2013). Evidence from ice shelves for channelized meltwater flow beneath the Antarctic Ice Sheet. *Nature Geoscience*, *6* (11).

LeDoux, C. M., Hulbe, C. L., Forbes, M. P., Scambos, T. A., and Alley, K. (2017). Structural provinces of the Ross Ice Shelf, Antarctica. A*nnals of Glaciology*,*58* (75pt1), 88-98.

Luckman, A., Jansen, D., Kulessa, B., Edward King, P., and Benn, D. (2012). Basal crevasses in Larsen C Ice Shelf and implications for their global abundance. *The Cryosphere*, *6* (1), 113-123.

Marsh, O. J., Fricker, H. A., Siegfried, M. R., Christianson, K., Nicholls, K. W., Corr, H. F., and Catania, G. (2016). High basal melting forming a channel at the grounding line of Ross Ice Shelf, Antarctica. *Geophysical Research Letters*, *43* (1), 250-255.

McGrath, D., Steffen, K., Scambos, T., Rajaram, H., Casassa, G., and Lagos, J. L. R. (2012). Basal crevasses and associated surface crevassing on the Larsen C Ice Shelf, Antarctica, and their role in ice-shelf instability. *Annals of Glaciology*, *53* (60), 10-18.

Noh, M.-J., and Howat, I. M. (2015). Automated stereo-photogrammetric DEM generation at high latitudes: Surface extraction with tin-based search-space minimization (SETSM) validation and demonstration over glaciated regions. *GIScience Remote Sensing*, *52* (2), 198-217.

Nuth, C., and Kääb, A. (2011). Co-registration and bias corrections of satellite elevation data sets for quantifying glacier thickness change. *The Cryosphere*, *5* (1), 271-290.

Rignot, E., Jacobs, S., Mouginot, J., and Scheuchl, B. (2013). Ice-shelf melting around Antarctica. *Science*, *341* (6143), 266-270.

Rist, M., Sammonds, P., Murrell, S., Meredith, P., Oerter, H., and Doake, C. (1996). Experimental fracture and mechanical properties of Antarctic ice: preliminary results. *Annals of Glaciology*, *23*, 284–292.

Rist, M., Sammonds, P., Murrell, S., Meredith, P., Doake, C., Oerter, H., and Matsuki, K. (1999). Experimental and theoretical fracture mechanics applied to Antarctic ice fracture and surface crevassing. *Journal of Geophysical Research: Solid Earth*, *104* (B2), 2973–2987.

Rist, M., Sammonds, P., Oerter, H., and Doake, C. (2002). Fracture of Antarctic shelf ice. *Journal of Geophysical Research: Solid Earth*, *107* (1).

Rott, H., Skvarca, P., & Nagler, T. (1996). Rapid collapse of northern Larsen ice shelf, Antarctica. *Science*, *271* (5250), 788-792.

Scambos, T. A., Bohlander, J., Shuman, C., and Skvarca, P. (2004). Glacier acceleration and thinning after ice shelf collapse in the Larsen B embayment, Antarctica. *Geophysical Research Letters*, *31* (18).

Scambos, T. A., Fahnestock, M., Moon, T., Gardner, A., and Klinger, M. (2019). *Ice speed of Antarctica (LISA), Version 1. [2016-2017].* Retrieved from https://doi.org/10.7265/nxpc-e997.

Shabtaie, S., and Bentley, C. R. (1982). Tabular icebergs: implications from geophysical studies of ice shelves. *Journal of Glaciology*, *28* (100), 413-430.

Simkins, L. M., Anderson, J. B., Greenwood, S. L., Gonnermann, H. M., Prothro, L. O., Halberstadt, A. R. W., Stearns, L.A., Pollard, D. and DeConto, R.M. (2017). Anatomy of a meltwater drainage system beneath the ancestral East Antarctic Ice Sheet. *Nature Geoscience*, *10* (9), 691-697.

Stearns, L. A., Smith, B. E., and Hamilton, G. S. (2008). Increased flow speed on a large East Antarctic outlet glacier caused by subglacial floods. *Nature Geoscience*, *1* (12), 827-831.

Swithinbank, C., and Lucchitta, B. K. (1986). Multispectral digital image mapping of Antarctic ice features. *Annals of Glaciology,8*, 159-163.

Van der Veen, C. J. (1998). Fracture mechanics approach to penetration of bottom crevasses on glaciers. *Cold Regions Science and Technology,27*(3), 213-223.

Van der Veen, C. J., Stearns, L. A., Johnson, J. T., and Csatho, B. M. (2014). Flow dynamics of Byrd Glacier, East Antarctica. *Journal of Glaciology,60*(224), 1053-1064

Vaughan, D. G. (1994). Investigating tidal flexure on an ice shelf using kinematic GPS. *Annals of Glaciology, (20)*, 372-376.

Vaughan, D. G., Corr, H. F., Bindschadler, R. A., Dutrieux, P., Gudmundsson, G. H., Jenkins, A., Newman, T., Vornberger, P., and Wingham, D. J. (2012). Subglacial melt channels and fracture in the floating part of Pine Island Glacier, Antarctica. *Journal of Geophysical Research: Earth Surface*, *117* (F3).

Whillans, I., Chen, Y., Van der Veen, C. J., and Hughes, T. (1989). Force budget: III. application to three-dimensional flow of Byrd Glacier, Antarctica. *Journal of Glaciology,35*(119), 68-80.

Conclusion

Typical glaciological studies cover only the past ~20 years because of the scarcity of available remotely sensed data. This limited timeline makes understanding glacier evolution due to climate change or internal ice dynamics difficult. Remote sensing techniques of long-term elevation changes and basal crevasse initiation were used as a means of expanding the temporal scale Antarctic glacier dynamics. In expanding the temporal scale, the specific aims of this research were to assess modern image processing techniques of historic aerial photography in conjunction of manually extracted ground control to produce accurate digital elevation models of Antarctic Glaciers; determine whether Transantarctic Mountain outlet glaciers been losing mass for the last 60 years; and establish abnormally large basal crevasses act as proxies for past subglacial flooding events. Combined results from all three chapters increases the temporal scale of Antarctic glacier dynamics by ~60-600 years, which is longer than any other surface elevation or basal crevasse study ever conducted to date.

Chapter 1: Assessing performance of SfM processing with historic imagery and manually derived GCPs

The results in Chapter 1 show that it is possible to produce accurate elevation products using historic aerial imagery with modern-day processing techniques and manually derived, non-*in situ*, ground control over Antarctic outlet glaciers. This was demonstrated using aerial imagery collected ~40 years ago over Byrd Glacier with SfM software. GCPs were identified from high-resolution satellite imagery and we found that when we increased the number of GCPs over regions of steep slopes, the resulting elevations are more accurate (an average accuracy of ~1.4

m for both DEMs). The SfM processing produced two DEMs of 10 m spatial resolution which are the highest resolution of historic elevation grids ever produced in Antarctica.

Having high-resolution historic DEMs allows for more accurate analysis of changes of glacier dynamics. We show this advantage by examining the grounding line of Byrd Glacier. Previous studies using manually derived elevations from photogrammetric methods of the same imagery used in Chapter 1, found that the grounding line of Byrd Glacier has migrated up-flow by ~20 km for the past 30 years which is an indicator of glacier instability. This conclusion was drawn by estimating the hydrostatic equilibrium boundary using elevation datasets of spatial resolutions 100 times greater than our SfM produced DEMs. Recalculating the hydrostatic equilibrium with the higher resolution historic DEMs and better bed topography from radar data, shows that the average grounding line migration is minimal, ~800 m, which is 25 times smaller than previous conclusions. Such a small amount of migration is minor and is an indicator that Byrd Glacier has actually been stable for the last ~40 years.

The orthorectified images could not be used to estimate velocity because of a white stripe captured in every image of the 1978 dataset. However, a work-around was developed in which the surface slope of the DEMs was calculated and the velocities were estimated from these products instead. This was possible because of the high spatial resolution of the DEMs. A spatial resolution of 10 m captures individual glacier surface characteristics like crevasses which allows for feature-tracking algorithms to estimate displacement over a period of time. It is advantageous to use elevation products to approximate velocity when the optical data is unusable.

The manual component involved in processing historic aerial imagery is non-trivial, but the ability to expand the temporal scale of glacier dynamic studies is well worth it. The accurate elevations generated using SfM processing with manually derived GCPs have shown that it is possible to extend this methodology to the trimetrogon aerial image datasets collected ~15-20 years prior to the images used in Chapter 1. Future work in expanding the development of this methodology will include means of overcoming spurious elevations produced from homologous snow-covered surfaces. The majority of Antarctica is smoothed-surfaced so being able to accurately construct this type of relief in SfM processing will significantly increase the coverage of historic elevations.

Chapter 2: TMA Imagery and surface elevation changes

Oblique images from TMA cameras were used in SfM processing with manually derived GCPs from high-resolution satellite imagery to produce the oldest elevation dataset from the Transantarctic Mountains. Surface hypsometries of Scott Glacier, Amundsen Glacier, Shackleton Glacier, Beardmore Glacier, Nimrod Glacier, Byrd Glacier, and Darwin Glacier were analyzed over a ~60-year period. We found that the average glacier elevations change has been a gain of .331 m or .006 m/yr. The elevation change ranges from ~-3 to +7 m with Amundsen Glacier experiencing the greatest loss and Nimrod Glacier having increased the most. Byrd Glacier experienced the least amount of overall change.

In previous research, the Transantarctic region has received little attention due to the lack of satellite data from limiting orbital paths. Other mass balance and elevation change studies find the catchment basin drained by these seven glaciers to be stable, and the findings from Chapter 2

agree with the projections that these glaciers and this catchment basin is stable. One discovery ascertained in this research and not observed in other studies is that the spatial pattern of elevation change on every glacier is not uniform. When elevation changes are not spatially homogeneous, it means that forces acting on the glacier are localized which causes varied patterns of elevation gains and losses. The exact causes of these spatial patterns are currently unknown and will require future work to better understand.

It is hypothesized that elevation changes on outlet glaciers flowing through the Transantarctic Mountains occur from either basal melt at the grounding line or changes in glacier dynamics (e.g. velocity) because accumulation and ablation rates are so small. Results from Nimrod Glacier's grounding line shows little migration over the past ~60 years which makes for dynamic change being a stronger argument for the origin of asymmetric dh spatial patterns. Analysis of surface velocities and elevation changes from tributary glaciers flowing into the outlet glaciers will be necessary before any definitive conclusions can be drawn about the influence of glacier dynamics in regards to elevation results.

Chapter 3: Basal crevasses and subglacial flooding events

Between 2005 and 2007, Byrd Glacier experienced a velocity increase of ~100 m/yr due to a subglacial flooding event from two subglacial lakes located in the catchment. During the speedup, tensile stresses increased at the grounding line and an abnormally large basal crevasse formed. Evidence of this large basal crevasse is identified in airborne radar echograms acquired in 2011. We propose that the formation of unusually large basal crevasses is due to periodic subglacial flooding events. Stearns et al., (2008) was the first study to observe subglacial

hydrology affecting glacier dynamics. This study is the first to show subsequent impacts (e.g. abnormally large basal crevasses) from hydrology-induced shifts in dynamics.

Identifying all of the basal crevasses in the Byrd Glacier fjord, from radar echograms, revealed that less than 3% of the crevasses were considered to be abnormally large (> 150 m). Assuming these crevasses all formed during speedups caused by subglacial flooding events, the limited presence of abnormally large crevasses indicates these incidents occur intermittently. These large crevasses form surface depressions that are identifiable from optical satellite imagery. Twenty-eight surface depressions are mapped over ~400 km from Byrd Glacier's grounding line to the terminus of the Ross Ice Shelf. A timeline of abnormally large basal crevasse formation reveals subglacial flooding events extending back to ~600 years ago.

Discovering a proxy for subglacial flooding events is crucial because these episodes are extremely difficult to observe due to the lack of coincident data. Antarctic subglacial flooding events and subsequent basal crevasses are not due to changes in climate; basal hydrologic episodes are dynamically driven, and this makes understanding their frequency and influence on ice sheets and ice shelves so important. By applying more realistic constraints to process-based and spatially-based subglacial hydrology models, numerical models will ultimately be able to more accurately assess the impact of hydrology on Antarctic glacier dynamics and better predict sea level rise.

Estimating relative ages to basal crevasses is the other significant outcome from this study because their formation and evolution is almost completely unknown. Rifts develop from basal

crevasses and have the ability to calve significant portions of ice shelves and thus, affect the stability of the ice sheet. Predictions of large tabular icebergs are constricted due to the lack of observations of crevasse initiations and rift propagations. While it does not appear that any basal crevasses from Byrd Glacier have evolved into rifts, rifts do exist elsewhere on several Antarctic ice shelves. Future work will use the tracking surface depressions to grounding lines (e.g. point of basal crevasse formation) methodology on other Antarctic outlet glaciers. The goal is that with an improved understanding of the ice dynamics triggering initial basal crevasses propagation that then evolve into rifts, the accuracy of predicting when and where large-scale calving events will occur, as well as ice shelf stability, will be greatly improved.

Summary

The use of historic remotely sensed data and techniques of manipulating present-day remotely sensed data to describe past glacier behavior are vital to better understanding glacier dynamics both in terms of expanding the temporal scale of studies and verifying whether present-day observations are unusual. This research has validated the use of historic data of Antarctic glaciers in present-day research and provided new insight into past glacier dynamics of elevation change and fracturing. An increasing amount of decades-old analog datasets are being discovered and digitized; their use is essential to a more thorough comprehension of the effects of changing climates on glaciers all over the world. Future plans will apply the techniques from this research with existing and new historic data to other Antarctic outlet glaciers. The results will be a better understanding of past dynamics and how they apply to current observations will aid in improved predictive modeling of not only outlet glaciers, but the entire Antarctic Ice Sheet as well.

Appendices: Data Lists

Appendix I. Regional Elevation Model of Antarctica

Present-day elevation data were supplied by the Byrd Polar, Climate Research Center, and the Polar Geospatial Center under NSF-OPP awards 1543501, 1810976, 1542736, 1559691, 1043681, 1541332, 0753663, 1548562, 1238993 and NASA award NNX10AN61G. The data are available through: http://data.pgc.umn.edu/elev/dem/setsm/REMA/geocell/v1.0/2m/

Glacier	PGC REMA ID
Scott	WV02_20160127_1030010050C79900_10300100518DA800_seg1_2m_dem.tif
	WV02_20170111_1030010060179200_10300100629E4D00_seg1_2m_dem.tif
	WV02_20170208_1030010065B55500_1030010065D86600_seg1_2m_dem.tif
	WV02_20160118_1030010050225300_1030010050A7A800_seg1_2m_dem.tif
	WV02_20161211_103001006095E600_1030010060D0A300_seg1_2m_dem.tif
	WV01_20170201_102001005B76A600_102001005A42EC00_seg1_2m_dem.tif
	WV02_20161121_103001005F30DC00_103001005FA9ED00_seg1_2m_dem.tif
	WV02_20161212_103001006129D500_10300100627D2400_seg1_2m_dem.tif
	WV01_20170128_102001005D2EEB00_102001005DDDF000_seg1_2m_dem.tif
	WV03_20161119_1040010025899900_1040010025807A00_seg1_2m_dem.tif
	WV02_20161123_103001005F798200_1030010060730800_seg1_2m_dem.tif
	WV03_20160109_104001001790A400_10400100164B7B00_seg1_2m_dem.tif
	WV02_20161225_1030010063BEC200_103001006145E200_seg1_2m_dem.tif
	WV01_20170130_102001005E633700_102001005A741400_seg1_2m_dem.tif
	WV02_20151225_103001004EAEFE00_103001004FD5D100_seg1_2m_dem.tif
	WV03_20170211_1040010028AA0A00_10400100289A4500_seg1_2m_dem.tif
	WV02_20170215_1030010065B7DC00_1030010063CEFD00_seg1_2m_dem.tif
	WV02_20170208_1030010064BEF300_1030010066171900_seg1_2m_dem.tif
	WV02_20161122_103001005FAE4B00_103001005E16FF00_seg1_2m_dem.tif
Amundsen	WV01_20170113_102001005B5C8A00_102001005DADF200_seg1_2m_dem.tif
	WV03_20151228_1040010016797B00_10400100169FB600_seg1_2m_dem.tif
	WV01_20170112_10200100592EFF00_102001005A68F300_seg2_2m_dem.tif
	WV02_20160111_103001004F63B500_103001004E0FB800_seg1_2m_dem.tif
	WV01_20170130_102001005DA0C500_102001005C20D100_seg1_2m_dem.tif
	WV01_20170111_102001005C350E00_102001005A5E1100_seg1_2m_dem.tif
	WV02_20170131_1030010064349A00_103001006310F500_seg1_2m_dem.tif

WV03_20170208_1040010028BD6900_10400100274EDF00_seg1_2m_dem.tif
WV01_20170111_102001005A904100_102001005A3CCD00_seg1_2m_dem.tif
WV03_20161213_10400100265EA800_1040010025293400_seg1_2m_dem.tif
WV02_20170210_10300100659BED00_10300100655D2B00_seg1_2m_dem.tif
WV02_20170111_1030010060179200_10300100629E4D00_seg1_2m_dem.tif
WV02_20161123_103001005F798200_1030010060730800_seg1_2m_dem.tif

Shackleton

WV01_20170112_102001005DE4AC00_102001005C19EF00_seg2_2m_dem.tif
WV01_20161212_102001005B87B900_1020010056EA6500_seg1_2m_dem.tif
WV02_20160122_103001004FD68300_103001004FC42E00_seg1_2m_dem.tif
WV01_20161122_1020010057CE9000_10200100595DA000_seg1_2m_dem.tif
WV01_20170128_102001005D76C900_102001005C0F6100_seg1_2m_dem.tif
WV02_20160203_103001004E446800_1030010050248800_seg1_2m_dem.tif
WV02_20140304_103001002E4EBA00_103001002D3E5500_seg1_2m_dem.tif
WV02_20170114_10300100627BD100_1030010063AEDA00_seg1_2m_dem.tif
WV02_20161121_1030010061C14100_103001005FC5EE00_seg1_2m_dem.tif
WV02_20170113_1030010062AEB400_10300100632D7400_seg2_2m_dem.tif
WV03_20161116_1040010026189500_10400100248D6700_seg1_2m_dem.tif
WV02_20170131_1030010064C24300_10300100629D7D00_seg1_2m_dem.tif
WV03_20151225_10400100150E1E00_1040010015722B00_seg1_2m_dem.tif
WV03_20170114_1040010027598C00_1040010027860500_seg1_2m_dem.tif
WV03_20161122_104001002540DE00_1040010025150800_seg1_2m_dem.tif
WV03_20161121_10400100255D5A00_10400100251D9400_seg1_2m_dem.tif

Beardmore

WV01_20161022_1020010058E4D200_1020010058851D00_seg1_2m_dem.tif
WV01_20161026_1020010056D47E00_1020010056440900_seg1_2m_dem.tif
WV01_20161121_102001005A27E800_1020010058BC3000_seg1_2m_dem.tif
WV01_20161122_102001005990B400_102001005993AF00_seg1_2m_dem.tif
WV01_20161217_102001005670DD00_10200100578D4F00_seg1_2m_dem.tif
WV01_20161217_102001005D80E900_102001005A18F100_seg1_2m_dem.tif
WV02_20161023_103001005D435800_103001005E37DE00_seg1_2m_dem.tif
WV02_20161114_103001005F85B700_103001005E393D00_seg1_2m_dem.tif
WV02_20161119_103001006006E900_1030010060D80700_seg1_2m_dem.tif
WV02_20161119_103001006041E200_103001006133FD00_seg1_2m_dem.tif
WV02_20161120_1030010061994800_1030010060783600_seg1_2m_dem.tif
WV02_20161121_1030010060695C00_103001005F120800_seg1_2m_dem.tif
WV02_20161217_1030010061C9EA00_1030010061137A00_seg1_2m_dem.tif
WV03_20161120_104001002582BF00_104001002561CC00_seg1_2m_dem.tif
WV03_20161121_10400100253B2B00_1040010024397500_seg1_2m_dem.tif
WV03_20161227_104001002675E500_1040010027CFDD00_seg1_2m_dem.tif
WV01_20170127_102001005D925E00_102001005D260100_seg1_2m_dem.tif

WV02_20170116_1030010063399700_103001006493C300_seg1_2m_dem.tif
WV03_20170129_10400100282C5700_1040010028B6E600_seg1_2m_dem.tif

Nimrod

WV03_20170105_1040010026731100_10400100273E1F00_seg1_2m_dem.tif
WV01_20170106_102001005C2E2D00_1020010057805500_seg1_2m_dem.tif
WV01_20161107_1020010058D26700_102001005888C200_seg1_2m_dem.tif
WV01_20170105_102001005C9E9E00_102001005B897900_seg1_2m_dem.tif
WV01_20170112_102001005BE8B500_102001005B630900_seg1_2m_dem.tif
WV01_20170114_102001005D710800_102001005A91A500_seg1_2m_dem.tif
WV01_20170106_102001005A0DE600_102001005893EC00_seg1_2m_dem.tif
WV01_20170225_102001005C2A0000_102001005B030800_seg1_2m_dem.tif
WV01_20161110_10200100597D4700_10200100572FB200_seg1_2m_dem.tif
WV02_20160112_103001004F60A200_103001005111CE00_seg1_2m_dem.tif
WV01_20161111_102001005594F600_10200100582F2B00_seg1_2m_dem.tif
WV01_20160201_102001004DC5A600_102001004A15B400_seg1_2m_dem.tif
WV01_20161028_1020010056D92600_1020010056CF5C00_seg1_2m_dem.tif
WV01_20170109_102001005B2DCE00_102001005BAA1100_seg1_2m_dem.tif
WV01_20161227_102001005B12E400_102001005BDD7100_seg1_2m_dem.tif
WV01_20140118_102001002853A800_102001002ABE4300_seg1_2m_dem.tif
WV01_20160929_1020010056A06700_1020010057073E00_seg1_2m_dem.tif
WV01_20141101_102001003457BC00_10200100352D2400_seg1_2m_dem.tif
WV02_20141103_10300100390EFE00_103001003A3BAC00_seg1_2m_dem.tif
WV02_20161030_103001005FA1B700_103001005EAF1700_seg1_2m_dem.tif
WV01_20141101_1020010036C42E00_102001003562D300_seg1_2m_dem.tif
WV01_20170114_102001005BA63900_102001005C691A00_seg1_2m_dem.tif
WV02_20161005_103001005E081A00_103001005B76DF00_seg1_2m_dem.tif
WV02_20170112_1030010065AD2200_1030010063A69600_seg1_2m_dem.tif

Byrd

WV01_20170117_102001005B5DCE00_102001005D03ED00_seg1_2m_dem.tif
WV01_20161022_10200100572C2600_102001005728F300_seg1_2m_dem.tif
WV02_20170114_1030010063357E00_103001006328C800_seg1_2m_dem.tif
WV02_20170112_1030010063C79200_1030010064666E00_seg1_2m_dem.tif
WV02_20161104_103001005E85A100_1030010061CB4700_seg1_2m_dem.tif
WV03_20170106_1040010026CC6900_10400100263B2100_seg1_2m_dem.tif
WV02_20161106_103001005DB42D00_103001005D998800_seg1_2m_dem.tif
WV02_20161104_103001005FB39200_103001005F580E00_seg1_2m_dem.tif
WV02_20161103_103001005D2CB600_103001005F7E5300_seg3_2m_dem.tif
WV01_20170112_102001005E897C00_1020010059681600_seg1_2m_dem.tif
WV01_20170220_102001005BB1E700_102001005B62C700_seg1_2m_dem.tif
WV03_20170220_1040010029C88300_1040010029A3F500_seg1_2m_dem.tif
WV01_20170106_10200100596C6200_1020010059CA5F00_seg1_2m_dem.tif

WV01_20161105_10200100596C1200_102001005681D700_seg1_2m_dem.tif
WV01_20170112_102001005D748700_102001005DAFDE00_seg1_2m_dem.tif
WV02_20160204_1030010050525F00_1030010051D1C200_seg1_2m_dem.tif
WV01_20161107_102001005A3DD700_1020010056A10100_seg1_2m_dem.tif
WV01_20160204_1020010049146A00_1020010047BD2A00_seg1_2m_dem.tif
WV01_20170121_102001005AC91A00_102001005A582200_seg1_2m_dem.tif
WV03_20170123_104001002827D100_104001002891ED00_seg1_2m_dem.tif
WV01_20160201_102001004ACC8100_10200100468C3C00_seg1_2m_dem.tif
WV01_20160120_10200100487B0B00_102001004C1AF200_seg1_2m_dem.tif
WV01_20170122_102001005A724300_10200100594FD400_seg1_2m_dem.tif
WV01_20170130_102001005C044C00_102001005C1ACD00_seg1_2m_dem.tif
WV03_20161103_10400100239D2200_10400100231A1300_seg1_2m_dem.tif

Darwin

WV01_20170106_102001005A32B400_1020010059485200_seg1_2m_dem.tif
WV02_20170112_1030010063C79200_1030010064666E00_seg1_2m_dem.tif
WV01_20170106_102001005B4BD900_102001005B1A0E00_seg1_2m_dem.tif
WV02_20161104_103001005FB39200_103001005F580E00_seg1_2m_dem.tif
WV03_20161103_104001002364D900_1040010024C05900_seg1_2m_dem.tif
WV03_20170108_104001002779FD00_1040010027BB2300_seg3_2m_dem.tif
WV01_20161125_1020010059DC1F00_10200100598EF900_seg1_2m_dem.tif
WV01_20121114_102001001DA9E700_102001001D88C900_seg6_2m_dem.tif
WV02_20141218_103001003BC56300_1030010039803700_seg6_2m_dem.tif
WV02_20131213_103001002A86EB00_103001002A062D00_seg3_2m_dem.tif
WV01_20170117_102001005B5DCE00_102001005D03ED00_seg1_2m_dem.tif
WV02_20170112_1030010063C79200_1030010064666E00_seg1_2m_dem.tif
WV03_20170106_1040010026CC6900_10400100263B2100_seg1_2m_dem.tif
WV02_20161104_103001005FB39200_103001005F580E00_seg1_2m_dem.tif
WV01_20170207_102001005DD37900_102001005CBA9100_seg1_2m_dem.tif
WV01_20170106_10200100596C6200_1020010059CA5F00_seg1_2m_dem.tif
WV01_20170112_102001005D748700_102001005DAFDE00_seg1_2m_dem.tif
WV01_20170121_102001005AC91A00_102001005A582200_seg1_2m_dem.tif
WV03_20170123_104001002827D100_104001002891ED00_seg1_2m_dem.tif
WV02_20141213_103001003C14F000_103001003B27F400_seg13_2m_dem.tif

Appendix II. TMA Images

The TMA imagery was downloaded from the USGS's Earth Resources Observation and Science Earth Explorer data portal available here: https://earthexplorer.usgs.gov/

Glacier	TMA Image ID
Scott	
	ARCA078033R0141
	ARCA078033R0142
	ARCA078033R0143
	ARCA078033R0144
	ARCA078033R0145
	ARCA144733R0116
	ARCA144733R0117
	ARCA144733R0118
	ARCA144733R0119
	ARCA144733R0120
	ARCA144731L0109
	ARCA144731L0110
	ARCA144731L0111
	ARCA144731L0112
	ARCA144731L0113
Amundsen	
	ARCA078033R0124
	ARCA078033R0125
	ARCA078033R0126
	ARCA143331L0259
	ARCA143331L0260
	ARCA143331L0261
	ARCA143331L0262
	ARCA143331L0263
Shackleton	
	ARCA078033R0057
	ARCA078033R0058
	ARCA078033R0059
	ARCA078033R0060
	ARCA078033R0061
	ARCA144731L0009

	ARCA144731L0010
	ARCA144731L0011
	ARCA144731L0012
	ARCA144731L0013
	ARCA113333R0100
	ARCA113333R0101
	ARCA113333R0102

Beardmore	
	ARCA078033R0005
	ARCA078033R0006
	ARCA078033R0007
	ARCA077533R0084
	ARCA077533R0085
	ARCA077533R0086

Nimrod	
	ARCA076933R0222
	ARCA076933R0223
	ARCA076933R0224
	ARCA076333R0002
	ARCA076333R0003
	ARCA076333R0004

Byrd	
	ARCA076833R0115
	ARCA076833R0116
	ARCA076833R0117
	ARCA100231L0086
	ARCA100231L0087
	ARCA100231L0088
	ARCA100231L0089
	ARCA100231L0090

Darwin	
	ARCA075231L0075
	ARCA075231L0076
	ARCA075231L0077
	ARCA114331L0079
	ARCA114331L0080
	ARCA114331L0081
	ARCA114333R0081
	ARCA114333R0082

ARCA114333R0083

Appendix III. CReSIS Echograms

The radar data were collected and generated by the Center of Remote Sensing of Ice Sheets from the support of the University of Kansas, NSF grant ANT-0424589, and NASA Operation IceBridge grant NNX16AH54G. The echograms are available from:
ftp://data.cresis.ku.edu/data/rds/2011_Antarctica_TO/CSARP_standard/

CReSIS Echogram IDs
Data_20111201_05_005
Data_20111205_08_003
Data_20111214_02_010
Data_20111214_02_012
Data_20111214_06_002
Data_20111214_06_003
Data_20111214_06_004
Data_20111216_03_002
Data_20111216_04_001
Data_20111216_04_003
Data_20111218_01_002
Data_20111218_01_003
Data_20111218_03_003
Data_20111218_03_005
Data_20111218_03_006
Data_20111218_03_007
Data_20111218_04_001
Data_20111218_04_009
Data_20111218_05_001
Data_20111218_05_003

Appendix IV. Landsat Imagery and derive products

The Landsat 7 ETM and Landsat 8 OCI imagery was downloaded from the USGS's EROS Earth Explorer data portal: https://earthexplorer.usgs.gov/

The LISA dataset was downloaded from the NSIDC website: ftp://ftp.nsidc.org/pub/DATASETS/nsidc0733_landsat_ice_speed_v01/LISA750/

Landsat 8 OCI Secene IDs
LC08_L1GT_046117_20161202_20170317_01_T2_B8.TIF
LC08_L1GT_047116_20161209_20170317_01_T2_B8.TIF
LC08_L1GT_047117_20170110_20170311_01_T2_B8.TIF
LC08_L1GT_048116_20170202_20170215_01_T2_B8.TIF
LC08_L1GT_048117_20170202_20170215_01_T2_B8.TIF
LC08_L1GT_048118_20170202_20170215_01_T2_B8.TIF
LC08_L1GT_049117_20170124_20170311_01_T2_B8.TIF
LC08_L1GT_050115_20170216_20170228_01_T2_B8.TIF
LC08_L1GT_050116_20170216_20170228_01_T2_B8.TIF
LC08_L1GT_050117_20161112_20170318_01_T2_B8.TIF
LC08_L1GT_050118_20161214_20170316_01_T2_B8.TIF
LC08_L1GT_051115_20170223_20170301_01_T2_B8.TIF
LC08_L1GT_051116_20170223_20170301_01_T2_B8.TIF
LC08_L1GT_051117_20170223_20170301_01_T2_B8.TIF
*Used for surface depression identification

LISA Dataset
lisa750_2016183_2017120_0000_0400_v1
*Velocity dataset used for feature tracking